Chapter 1
Electrodeposition and Characterization of Alloys and Composite Materials

V.D. Jović, U.Č. Lačnjevac, and B.M. Jović

1.1 Introduction

It is general experience in materials science that alloy can exhibit qualities that are unobtainable with parent metals. This is particularly true for electrodeposited alloys. Some important properties of materials, such as hardness, ductility, tensile strength, Young's modulus, corrosion resistance, solderability, wear resistance, and antifriction service, may be enhanced. At the same time some properties that are not characteristic for parent metals, such as high magnetic permeability, other magnetic and electrical properties, amorphous structure, etc., can also be obtained. In some cases alloy coatings may be more suitable for subsequent electroplate overlayers and conversion chemical treatments [1].

Some alloys may be more easily obtained by electrodeposition than by metallurgical processes. This is particularly true for alloys composed of metals having large differences in melting temperatures or cannot be mixed in a liquid state. Such metals can very often be codeposited from the solutions (e.g., alloys Ag–Ni, Ag–Co, and Cd–Co). Taking into account that some metals cannot be deposited from the aqueous solutions (Ti, V, W, Nb, Zr, etc.), they could be deposited from the melts of their salts. In recent times the processes of metals and alloys deposition from the room temperature molten salts were also investigated and developed (deposition of Al–Cu, Al–Co, Al–Ni alloys from $AlCl_3$–MeEtImCl melt).

The fast-growing requirements of modern industry for materials with special qualities in the last century have given rise to increasing interest in electrodeposition of alloys, particularly in corrosion protection and in the modern electronic industry [1].

V.D. Jović (✉) • U.Č. Lačnjevac • B.M. Jović
Department of Materials Science, Institute for Multidisciplinary Research,
Kneza Višeslava 1, 11030 Belgrade, Serbia
e-mail: vladajovic@imsi.rs

S.S. Djokić (ed.), *Electrodeposition and Surface Finishing: Fundamentals and Applications*, Modern Aspects of Electrochemistry 57,
DOI 10.1007/978-1-4939-0289-7_1,

Historically, the electroplating of alloys is practically as old as electroplating of pure metals, since the electroplating of brass and bronze was performed by De Ruolz [2] in 1842, shortly after the discovery of the first cyanide baths. It is interesting to note that these baths were essentially similar to ones used nowadays, being based on the use of Cu, Sn, and Zn complexes with cyanide.

From 1842 until the end of the nineteenth century, over 180 alloys involving 40 elements have been deposited [3]. An excellent review of the achievements up to 1962 is given in the book of Brenner [4], while from practical point of view it is recommended to consider the book of Bondar, Grimina, and Pavlov [5], which contains recipes and references for more than 1,100 baths for alloy deposition.

Although the first alloys [2] were deposited in 1842, practically the first attempt at scientific approach to electrodeposition of alloys, discussing the role of cathodic potential in the deposition of brass, came rather late with the work of Spitzer [6] in 1905. In 1914 a more comprehensive attempt came from Schlötter [7], but better under-standing of the alloy deposition process by understanding the electrochemical thermodynamics and kinetics, as well as complexometry and some other fields in order to obtain clear scientific bases, had to await second part of the nineteenth century. Some attempts were made by Gorbunova and Polukarov [8], Fedoteev et al. [9], and Faust [10], but they remained at a rather elementary level, obviously oriented to help practical electroplaters.

The results obtained until 1995 are summarized in the chapter by Despić and Jović [1]. Recently, published results on electrodeposition of alloys, with a particular attention on Ni–MoO_2 composite coatings used as catalysts for the hydrogen evolution reaction (HER), are discussed in this chapter.

1.2 Electrodeposition of Alloys from Aqueous Solutions

1.2.1 Conditions for Electrodeposition of Alloys

The metals immersed in the solution of their simple salts establish the reversible potential. The values of the reversible potentials for different metals could differ for about 3 V. Electrodeposition of metals could take place only at potentials more negative than the reversible ones. Accordingly, in the solution of ions of two metals (cf. Cu^{2+} and Zn^{2+}) with one being on the positive side of the potential scale (vs. SHE) (Cu) and another one being on the negative side of the potential scale (Zn), intensive deposition of Cu could take place at potentials at which Zn would not deposit at all. Taking into account that the reversible potentials of metals could change with the presence of different anions in the solution (complexation of metal ions), and that the rates of electrodeposition of different metals are usually different, it is possible to achieve conditions for simultaneous deposition of these two metals [1].

For simultaneous deposition of two metals, A and B, their deposition potentials (E) must be identical, $E(\mathrm{A}) = E(\mathrm{B})$, i.e.,

$$E_\mathrm{r}(\mathrm{A}) + \eta(\mathrm{A}) = E_\mathrm{r}(\mathrm{B}) + \eta(\mathrm{B}), \tag{1.1}$$

where $E_\mathrm{r}(\mathrm{A})$ and $E_\mathrm{r}(\mathrm{B})$ are reversible potentials of metals A and B, while $\eta(\mathrm{A})$ and $\eta(\mathrm{B})$ correspond to the overpotentials needed for the deposition of these two metals. The reversible potential could be changed by the change of metal ions concentration in the solution and by the temperature of the solution and is defined by the Nernst's equation:

$$E_\mathrm{r}(\mathrm{A}) = E^\Theta(\mathrm{A}) + \frac{RT}{pF}\ln a(\mathrm{A}^{\mathrm{p}+}), \tag{1.2}$$

$$E_\mathrm{r}(\mathrm{B}) = E^\Theta(\mathrm{B}) + \frac{RT}{qF}\ln a(\mathrm{A}^{\mathrm{q}+}), \tag{1.3}$$

where $E^\Theta(\mathrm{A})$ and $E^\Theta(\mathrm{B})$ are standard potentials of metals A and B, a activities of corresponding metal ions in the solution, and p and q numbers of electrons to be exchanged during the process of metal deposition.

The condition defined by Eq. (1.1) could be accepted only as a first approximation, since the potential of the metal deposition is undefined quantity if the value of corresponding current density is not known. It appears that a better definition of the conditions for simultaneous deposition of two metals would be current density at which both metals deposit with approximately the same current density. More precisely, for two-components alloy to be deposited with the molar ratio of the more noble metal x and the less noble metal $(1 - x)$, assuming that the Faraday's low is obeyed, following relations should be fulfilled:

$$x = \frac{n_\mathrm{A}}{n_\mathrm{A} + n_\mathrm{B}} = \frac{\frac{j_\mathrm{A}}{p}}{\frac{j_\mathrm{A}}{p} + \frac{j_\mathrm{B}}{q}} \tag{1.4}$$

and

$$(1 - x) = \frac{n_\mathrm{B}}{n_\mathrm{A} + n_\mathrm{B}} = \frac{\frac{j_\mathrm{B}}{q}}{\frac{j_\mathrm{A}}{p} + \frac{j_\mathrm{B}}{q}}, \tag{1.5}$$

where n_A and n_B are numbers of moles of components A and B. Hence, the current density ratio for the deposition of these two metals should be defined as

$$\frac{j_\mathrm{A}}{j_\mathrm{B}} = \frac{p}{q}\frac{x}{(1 - x)}. \tag{1.6}$$

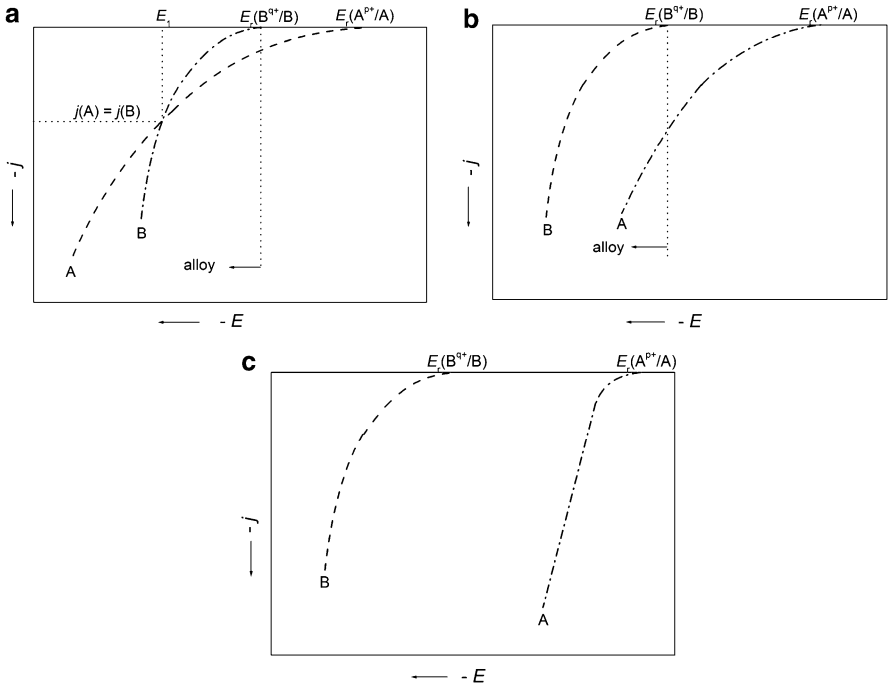

Fig. 1.1 Schematic presentation of the characteristic cases for alloy deposition

The condition defined by Eq. (1.6) could be achieved by proper adjustment of three essential variables: the concentration of the depositing ions at the electrode/solution interface (where the discharge occurs), the electrode potential, and the temperature.

In order to obtain better inside into the conditions defined by Eqs. (1.1, 1.2, 1.3, 1.4, 1.5, and 1.6), it is important to present polarization curves (current density versus potential relationships) for deposition of each metal. The characteristic cases are presented in Figs. 1.1 and 1.2. The first case is presented in Fig. 1.1a: the overpotential for deposition of the more noble metal A is higher than that for the less noble metal B. From the potentials $E_r(A^{p+}/A)$ to $E_r(B^{q+}/B)$ only more noble metal deposition occurs, while the deposition of alloy commences at the potential E_1. In the potential range from $E_r(B^{q+}/B)$ to E_1 metal A deposits with higher current density than metal B (the alloy contains more metal A than B). At the potential E_1 both metals deposit with the same current density, and the alloy contains the same amount of both metals. At the potentials more negative than E_1, the metal B deposits with higher current density and, accordingly, the alloy contains more metal B than metal A. The second case is presented in Fig. 1.1b: the overpotential for deposition of metal A is slightly lower than that for metal B, i.e., the polarization curves are almost parallel. Hence, the deposition of alloy commences at the potential $E_r(B^{q+}/B)$, while the alloy contains more metal A than B. If the difference between $E_r(A^{p+}/A)$ and $E_r(B^{q+}/B)$ is high and the overpotential for deposition of the

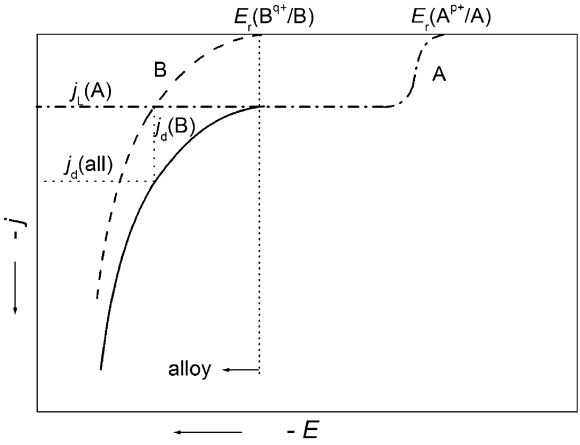

Fig. 1.2 Polarization curves for the deposition of more noble metal (A) and less noble metal (B): $j_L(A)$—diffusion limiting current density for the deposition of metal (A); $j_d(B)$—current density for the deposition of metal (B); $j_d(all)$—current density for the deposition of alloy

more noble metal A is lower than that for the less noble metal B, the third case, presented in Fig. 1.1c applies: in such a case alloy deposition is impossible. The difference between the reversible potentials of two metals could be changed (lowered) by the change of metal ions concentration (activity), and in most cases this is achieved by the complexation.

Simultaneous deposition of two metals is possible even if the difference in their reversible potentials is high if the applied current density for alloy deposition is higher than the diffusion limiting current density for the deposition of the more noble metal. Such a case is schematically presented in Fig. 1.2.

If $p = q = 2$ the molar ratios of metals (A) and (B) in the alloy are defined by the following relation:

$$x(\mathrm{A}) = \frac{j_\mathrm{L}(\mathrm{A})}{j_\mathrm{L}(\mathrm{A}) + j_\mathrm{d}(\mathrm{B})} = \frac{j_\mathrm{L}(\mathrm{A})}{j_\mathrm{d}(\mathrm{all})},$$
$$x(\mathrm{B}) = \frac{j_\mathrm{d}(\mathrm{B})}{j_\mathrm{L}(\mathrm{A}) + j_\mathrm{d}(\mathrm{B})} = \frac{j_\mathrm{d}(\mathrm{B})}{j_\mathrm{d}(\mathrm{all})}. \tag{1.7}$$

1.2.2 Reversible Potential of Alloys in the Solution of Corresponding Ions

According to the electroplating literature [4], when an alloy composed of metals A and B is immersed in the solution containing corresponding metal ions (A^{p+} and B^{q+}), its potential is termed as "static potential." In such a case it is desired to establish the conditions under which no net process would take place, so that the potential could be considered as the reversible potential of the alloy. Taking into account that an alloy may (and very often does) consist of several phases (intermetallic compounds), with each phase having different thermodynamic properties, it should be expected to have different reversible potential for each alloy composition. Such a case is essentially a

nonequilibrium situation. Nevertheless, the thermodynamic properties of each phase, and accordingly the problem of its reversible potential, can be treated assuming that this is the only phase present in a given situation (it will be discussed later).

The problem of the reversible potential of alloys has been treated in the literature [1, 11, 12] in terms of the Nernst equation applied to the less noble metal only, while the more noble component of the alloy being considered as an inert metal matrix. Such approach is not appropriate since it yields unrealistic results. Hence, in a proper approach the thermodynamic property of the alloy cannot be assigned to an individual component of the alloy. Instead, a phase should be treated as composed of a chemical entity of stoichiometric composition corresponding to the alloy composition. Accordingly, a phase can be described as $A_xB_{(1-x)}$ and the formation of one mole of the substance characterizing this phase should be presented by the following chemical reaction:

$$x\mathrm{A} + (1-x)\mathrm{B} \Leftrightarrow \mathrm{A}_x\mathrm{B}_{(1-x)}. \tag{1.8}$$

1.2.2.1 The Influence of the Gibbs Energy of Phase Formation

The change of the Gibbs energy in the formation of the phase $A_xB_{(1-x)}$ can be described in terms of their standard partial molar Gibbs energies (standard chemical potentials) as

$$\Delta_\mathrm{f}G^\Theta\left(\mathrm{A}_x\mathrm{B}_{(1-x)}\right) = \mu^\Theta\left(\mathrm{A}_x\mathrm{B}_{(1-x)}\right) - x\mu^\Theta(\mathrm{A}) - (1-x)\mu^\Theta(\mathrm{B}). \tag{1.9}$$

The phase $A_xB_{(1-x)}$ can also be formed in the electrochemical cell from the ions of both metals (A^{p+} and B^{q+}) present in the solution. In such a case the electrochemical cell is composed of an electrode made of the alloy phase as cathode and a standard hydrogen electrode as anode. The cell reaction is then

$$x\mathrm{A}^{\mathrm{p}+} + (1-x)\mathrm{B}^{\mathrm{q}+} + \left[\frac{xp+(1-x)q}{2}\right]\mathrm{H}_2 = \mathrm{A}_x\mathrm{B}_{(1-x)} + [xp+(1-x)q]\mathrm{H}^+. \tag{1.10}$$

The standard Gibbs energy change for this reaction is defined by the equation:

$$\begin{aligned}\Delta G^\Theta_\mathrm{cell} = {} & \mu^\Theta\left(\mathrm{A}_x\mathrm{B}_{(1-x)}\right) + [xp+(1-x)q]\mu^\Theta(\mathrm{H}^+) - x\mu^\Theta(\mathrm{A}^{\mathrm{p}+}) \\ & - (1-x)\mu^\Theta(\mathrm{B}^{\mathrm{q}+}) - \left[\frac{xp+(1-x)q}{2}\right]\mu^\Theta(\mathrm{H}_2).\end{aligned} \tag{1.11}$$

Taking into account that

$$[xp+(1-x)q]\mu^\Theta(\mathrm{H}^+) - \left[\frac{xp+(1-x)q}{2}\right]\mu^\Theta(\mathrm{H}_2) = 0, \tag{1.12}$$

it follows that the standard Gibbs energy change in the electrochemical cell is defined by the equation:

$$\Delta G^{\Theta}_{\text{cell}} = \mu^{\Theta}\left(\mathrm{A}_x\mathrm{B}_{(1-x)}\right) - x\mu^{\Theta}(\mathrm{A}^{\mathrm{p}+}) - (1-x)\mu^{\Theta}(\mathrm{B}^{\mathrm{q}+}). \tag{1.13}$$

The electromotive force of this cell, which is identical with the electrode potential of the alloy phase on the standard hydrogen scale, is given by

$$E\left(\mathrm{A}_x\mathrm{B}_{(1-x)}\right) = E^{\Theta}\left(\mathrm{A}_x\mathrm{B}_{(1-x)}\right) + \frac{RT}{[xp+(1-x)q]F}\ \ln\ a(\mathrm{A}^{\mathrm{p}+})^{x} a(\mathrm{B}^{\mathrm{q}+})^{(1-x)}. \tag{1.14}$$

The standard electrode potential of the alloy phase, $E^{\Theta}(\mathrm{A}_x\mathrm{B}_{(1-x)})$, is related to the standard Gibbs energy change in the cell, defined by the following equation:

$$\begin{aligned} E^{\Theta}\left(\mathrm{A}_x\mathrm{B}_{(1-x)}\right) &= \frac{-\Delta G^{\Theta}_{\text{cell}}}{[xp+(1-x)q]F} \\ &= \frac{-\mu^{\Theta}\left(\mathrm{A}_x\mathrm{B}_{(1-x)}\right) + x\mu^{\Theta}(\mathrm{A}^{\mathrm{p}+}) + (1-x)\mu^{\Theta}(\mathrm{B}^{\mathrm{q}+})}{[xp+(1-x)q]F}, \end{aligned} \tag{1.15}$$

where $[xp + (1 - x)q]F$ represents the total number of electrons exchanged in one act of the cell reaction [Eq. (1.10)].

The standard Gibbs energies of formation of the ions relative to that of the hydrogen ion (taken as zero), which are equal to the standard chemical potentials of the ions, are related to the standard potentials of the corresponding metals on the standard hydrogen scale as

$$\Delta_{\mathrm{f}} G^{\Theta}(\mathrm{A}^{\mathrm{p}+}) = \mu^{\Theta}(\mathrm{A}^{\mathrm{p}+}) = pFE^{\Theta}(\mathrm{A}^{\mathrm{p}+}/\mathrm{A}) \tag{1.16}$$

and

$$\Delta_{\mathrm{f}} G^{\Theta}(\mathrm{B}^{\mathrm{q}+}) = \mu^{\Theta}(\mathrm{B}^{\mathrm{q}+}) = pFE^{\Theta}(\mathrm{B}^{\mathrm{q}+}/\mathrm{B}). \tag{1.17}$$

Substituting Eqs. (1.16) and (1.17) into Eq. (1.15) and then substituting the resulting $E^{\Theta}(\mathrm{A}_x\mathrm{B}_{(1-x)})$ into Eq. (1.14), the reversible potential of the alloy phase is obtained as

$$\begin{aligned} E\left(\mathrm{A}_x\mathrm{B}_{(1-x)}\right) = {} & \frac{xp}{[xp+(1-x)q]}\left[E^{\Theta}(\mathrm{A}^{\mathrm{p}+}/\mathrm{A}) + \frac{RT}{pF}\ \ln\ a(\mathrm{A}^{\mathrm{p}+})\right] \\ & + \frac{(1-x)q}{[xp+(1-x)q]}\left[E^{\Theta}(\mathrm{B}^{\mathrm{q}+}/\mathrm{B}) + \frac{RT}{qF}\ \ln\ a(\mathrm{B}^{\mathrm{q}+})\right] \\ & - \frac{\mu^{\Theta}\left(\mathrm{A}_x\mathrm{B}_{(1-x)}\right)}{[xp+(1-x)q]F}, \end{aligned} \tag{1.18}$$

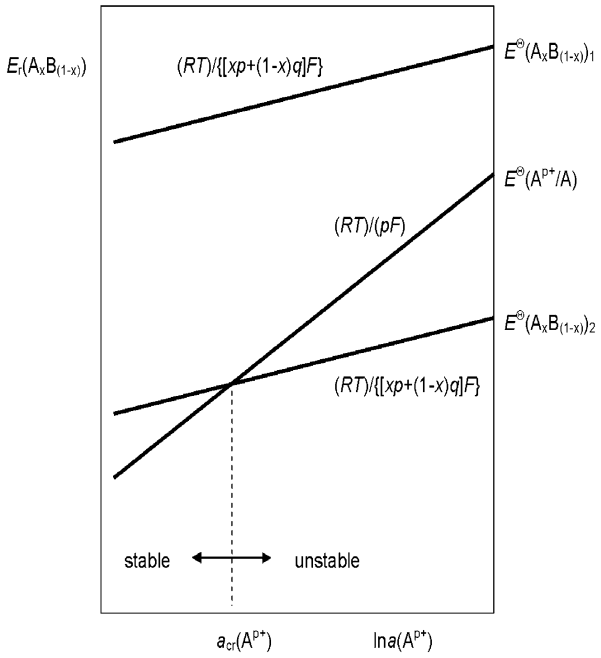

Fig. 1.3 Schematic presentation of the range of stability of phases $(A_xB_{(1-x)})_1$ and $(A_xB_{(1-x)})_2$ as a function of the concentration of more noble metal ions, ln $a(A^{p+})$ (Reprinted from [1] with the permission of Springer)

where $\mu^{\Theta}(A_xB_{(1-x)}) = \Delta_f G^{\Theta}(A_xB_{(1-x)}) - x\mu^{\Theta}(A) - (1-x)\mu^{\Theta}(B)$ is the standard chemical potential of the alloy phase relative to those of metal constituents. From Eq. (1.18) it could be concluded that: (a) the reversible potential of an alloy phase depends on the activities of ions of both metals in solution and (b) the dominant role in determining the position of the standard potential of the alloy phase relative to the pure metals is played by the standard molar Gibbs energy of the alloy phase formation [1].

1.2.2.2 Stability of Phases in the Solution of Corresponding Ions

When ions corresponding to metal constituents of an alloy phase are present in the solution, it is necessary to take into consideration their tendency to form other possible alloy phases or undergo reduction to pure metals. Accordingly, if another alloy phase or a pure metal would yield a more noble reversible potential, thermodynamic conditions for anodic dissolution of the existing alloy phase are created ("replacement reaction"). Hence, the considered alloy phase becomes unstable tending to undergo corrosive degradation. It can be shown that the instability depends on the activity of the metal ions in solution. Such a case [1] is schematically presented in Fig. 1.3.

Equation (1.14) defines the reversible potential of any alloy phase, as well as the reversible potential of the pure more noble metal ($x = 1$). Assuming a constant activity of the ions of the less noble constituent of the alloy ($a(B^{q+}) = 1$), it can be seen in Fig. 1.3 that the slope of a plot of E_r versus ln $a(A^{p+})$ is always larger for the pure more noble metal than for the alloy phase, since $\{x/[xp + (1 - x)q]\} < 1/p$ for any $x < 1$. If $E^{\Theta}(A_xB_{(1-x)})_1$ of the alloy phase 1 turns out to be more positive than other alloy phase 2, $E^{\Theta}(A_xB_{(1-x)})_2$, or of the pure more noble metal, $E^{\Theta}(A^{p+}/A)$, then the alloy phase will remain stable over the entire range of activities of ions of the more noble metal. If $E^{\Theta}(A_xB_{(1-x)})_2 < E^{\Theta}(A^{p+}/A)$, as shown in Fig. 1.3, there is a crossing point between the two functions at the activity $a_{cr}(A^{p+})$. At the activities larger than $a_{cr}(A^{p+})$ the metal would tend to precipitate on the account of dissolution of the alloy phase 2, i.e., the alloy phase 2 will be unstable. Conversely, at activities smaller than $a_{cr}(A^{p+})$ the alloy phase 2 will remain stable in the solution [1].

Taking into account discussion about the alloy phase stability, it is recommended not to introduce into the solution ions of the more noble metal, but only those of the less noble one. At the beginning of the nineteenth century (1907), Pushin [12] was aware of this fact and in his work the potentials of alloys were measured in the solution containing only less noble metal ions, and the same metal was used as the reference electrode.

1.2.3 Types of Electrodeposition of Alloys

According to Brenner [4], electrochemical codeposition of two metals to form an alloy could be: equilibrium, irregular, regular, anomalous, and induced. This classification is based on the relation between the composition of the deposited alloy (percentages of metals in the alloy) and the "metal ratio" which represents percentages of corresponding metal ions in the solution independently of their ionic form ("stoichiometric concentrations"). For the regular, irregular, and equilibrium codeposition, it is characteristic that the relative content of metals in the deposited alloy corresponds to that expected from the relation between their reversible potentials, whereas anomalous codeposition corresponds to the reverse situation. Induced codeposition is characteristic for the metals which cannot be deposited from the aqueous solutions, Mo, Ti, W, Ge, but can be codeposited with the iron-group metals (Fe, Co, Ni).

1.2.3.1 Equilibrium Codeposition

Equilibrium codeposition implies a common reversible potential for both metal constituents so that the reduction of both metal ions would take place at potentials more negative than the reversible ones. To close the gap between the reversible potentials of depositing metals, it is necessary to make the concentration of simple

salts (undergoing complete dissociation) of the more noble metal impractically low and of the less noble metal impractically high. As stated in Sect. 1.2.2.1 the best way to overcome this problem could result from complexation of metal ions with different ligands. Complexation usually changes the activity of the resulting species in solution by many orders of magnitude, while keeping the total amount of one or other metal in solution sufficiently high for a good supply of plating material to the cathode. It is very often case that the ions of both metals form complexes with one and the same ligand with similar values of the stability constants, so that the change of the potential of the deposition of each metal is the same (or similar) value. Usually, in such a case, the complexation with two different ligands could result in a more pronounced change of the deposition potentials of two metals. In a further text an example for the deposition of the Ni–Sn alloy from the solution containing pyrophosphate and glycine ligands is presented [13].

According to the literature [14] standard potential of the Ni deposition is −0.23 V vs. SHE, while that for Sn is −0.1364 V vs. SHE and accordingly Ni is less noble metal. Taking into account that the overvoltage for Ni deposition [15] is much higher than that for Sn deposition, the difference between the potentials of deposition of these two metals should be larger than that of their standard potentials. In the data presented in Dean's Handbook of Chemistry [16] Ni forms two pyrophosphate complexes, $[Ni(P_2O_7)]^{2-}$ and $[Ni(P_2O_7)_2]^{6-}$, and three glycine complexes, $[Ni(NH_2CH_2COO)]^{+}$, $[Ni(NH_2CH_2COO)_2]$, and $[Ni(NH_2CH_2COO)_3]^{-}$. There are only three papers in the literature with the data for different complexes of Ni and Sn in the pyrophosphate and glycine solutions, the data proposed by Duffield et al. [17], Turyan et al. [18], and Orekhova et al. [19]. Corresponding reactions for the formation of different complexes and their formation (stability) constants are given in the work of Duffield et al. [17]. All species and their stability constants used for the calculation of the distribution of different complexes in the solution containing Sn, Ni, pyrophosphate, and glycine ions are listed in Table 1.1.

The calculation of the distribution of complexes in the solution containing pyrophosphate and glycine showed that $[Sn(P_2O_7)_2]^{6-}$ is dominant complex with Sn at pH 8.0, while two complexes of Ni dominate: complex $[Ni(P_2O_7)_2]^{6-}$ and complex $[Ni(NH_2CH_2COO)_3]^{-}$. This is shown in Fig. 1.4.

The values of the equilibrium potentials of prevailing complexes (E_{eq}), calculated using explanations based on the Gibbs energy change for reaction of certain complex formation [20] (assuming that the ions activities are equal to their concentrations), are also presented in Table 1.1. As can be seen, the equilibrium potential for deposition of Sn by the reduction of $[Sn(P_2O_7)_2]^{6-}$ complex is −0.847 V vs. SCE, while the equilibrium potentials for the reduction of $[Ni(P_2O_7)_2]^{6-}$ and $[Ni(NH_2CH_2COO)_3]^{-}$ complexes are more positive, being about −0.716 V vs. SCE, and situation becomes opposite to that for deposition from the solution of simple ions. After the complexation Ni becomes more noble metal, while Sn becomes less noble one. Hence, it could be concluded that at pH 8.0 Sn would deposit from the complex $[Sn(P_2O_7)_2]^{6-}$, while Ni would deposit simultaneously from two complexes, $[Ni(P_2O_7)_2]^{6-}$ and $[Ni(NH_2CH_2COO)_3]^{-}$, in the presence of both complexing anions. The equilibrium potentials for deposition

Table 1.1 All complexes present in the solution containing 0.1 M $SnCl_2$ + 0.1 M $NiCl_2$ + 0.6 M $K_4P_2O_7$ + 0.3 M NH_2CH_2COOH, their concentrations, stability constants, and equilibrium potentials of prevailing complexes

Complexes	log β	Conc. (M)	E_{eq} (V vs. SCE)
$[H(P_2O_7)]^{3-}$	8.14		
$[H_2(P_2O_7)]^{2-}$	14.01		
$[H_3(P_2O_7)]^{-}$	15.78		
$[H_4(P_2O_7)]$	16.63		
$[H(NH_2CH_2COO)]$	9.64		
$[H_2(NH_2CH_2COO)]^{+}$	12.05		
$[Sn(NH_2CH_2COO)H]^{2+}$	12.78		
$[Sn(NH_2CH_2COO)]^{+}$	10.02		
$[Sn(P_2O_7)]^{2-}$	**13.05**	**0.007**	**−0.847**
$[Sn(P_2O_7)H]^{-}$	15.92		
$[Sn(P_2O_7)H_2]$	17.47		
$[Sn(P_2O_7)_2]^{6-}$	**16.27**	**0.093**	**−0.847**
$[Sn(P_2O_7)_2H]^{5-}$	22.31		
$[Sn(P_2O_7)_2H_2]^{4-}$	26.79		
$[Sn(P_2O_7)_2H_3]^{3-}$	30.07		
$[Sn(P_2O_7)_2H_4]^{2-}$	31.58		
$[Sn(P_2O_7)OH]^{3-}$	5.32		
$[Sn(P_2O_7)(OH)_2]^{2-}$	−4.77		
$[Sn(P_2O_7)_2OH]^{5-}$	7.04		
$[Ni(NH_2CH_2COO)]^{+}$	5.60		
$[Ni(NH_2CH_2COO)_2]$	**10.40**	**0.009**	**−0.716**
$[Ni(NH_2CH_2COO)_3]^{-}$	**13.80**	**0.057**	**−0.716**
$[Ni(P_2O_7)]^{2-}$	**5.80**	**0.005**	**−0.716**
$[Ni(P_2O_7)_2]^{6-}$	**7.40**	**0.029**	**−0.716**

Reprinted from [13] with the permission of Electrochemical Society

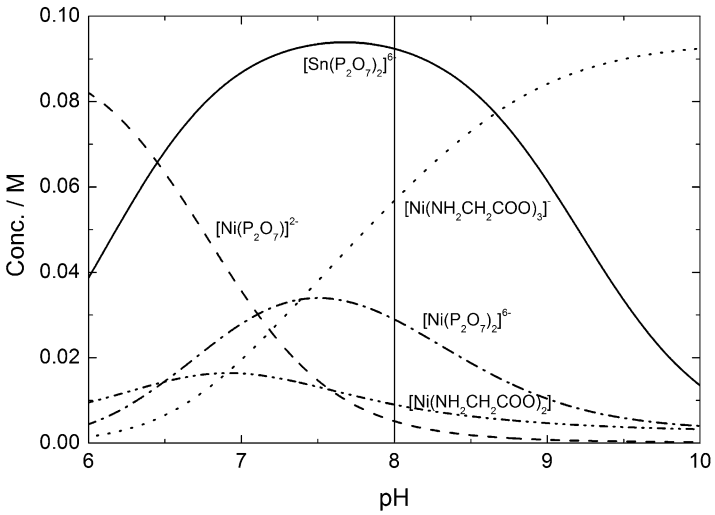

Fig. 1.4 Distribution of different complexes in the solution containing 0.1 M $SnCl_2$ + 0.1 M $NiCl_2$ + 0.6 M $K_4P_2O_7$ + 0.3 M NH_2CH_2COOH as a function of the solution pH

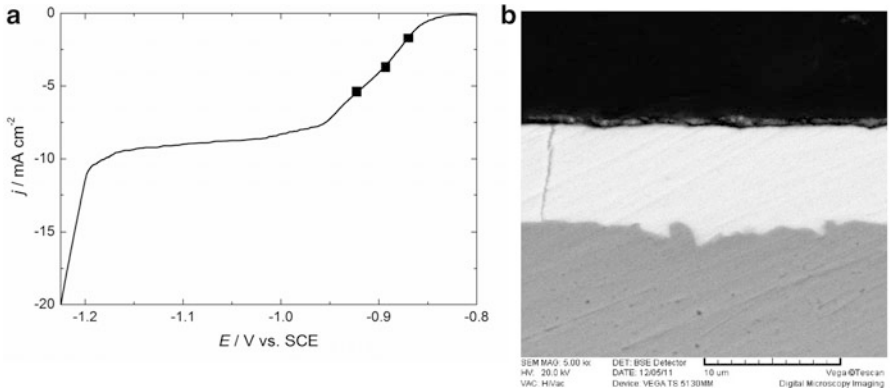

Fig. 1.5 (**a**) Polarization curve for deposition of the Ni–Sn alloy onto Ni electrode. (**b**) Typical cross section of coatings obtained at different current densities marked with solid squares in Fig. 1.5a (Reprinted from [21] with the permission of Int. J. Hydrogen Energy)

of Sn and Ni still differ for 0.131 V. As already stated, because of high overvoltage for Ni deposition [13], it could be expected that two metals possess identical, or similar, potential of deposition. This is exactly the case for these two metals in the pyrophosphate–glycine solution. The polarization curve for Ni–Sn alloy deposition onto Ni electrode is shown in Fig. 1.5a [21]. The deposition process commences at about −0.83 V vs. SCE being activation controlled down to about −0.95 V vs. SCE, while in the potential range from about −0.95 V to about −1.20 V well-defined diffusion limiting current density (−10 mA cm^{-2}) is established. In the region of the activation control (squares marked on Fig. 1.5a), Ni–Sn alloy coatings were deposited at the current densities of −2, −4, and −6 mA cm^{-2}. Flat and compact deposits were obtained in all cases, as shown in Fig. 1.5b. The composition of the coatings changed with the increase of cathodic current density from about 37 at.% Ni (for sample obtained at −2 mA cm^{-2}) to about 45 at.% Ni (for sample obtained at −6 mA cm^{-2}) [21], but in all cases both metals were present in the coating, indicating a good example for equilibrium codeposition.

1.2.3.2 Irregular Codeposition

The irregular type of codeposition is very often characterized by simultaneous influence of cathodic potential and diffusion phenomena, i.e., it mainly occurs under the activation and/or mixed control of the deposition processes. The rate of deposition in such a case is expressed by Butler–Volmer equation which is usually used for the kinetics of electrochemical processes [1]:

$$\frac{j}{j^{o}} = \frac{j_{o}}{j^{o}}\left[\exp\left(\frac{\alpha_{a}F}{RT}\eta\right) - \left(\frac{c}{c_{o}}\right)\exp\left(\frac{-\alpha_{c}F}{RT}\eta\right)\right], \tag{1.19}$$

where $\eta = E - E_{r}$ corresponds to the overpotential needed for the deposition of metals [see Eq. (1.1)], c and c_{o} represent concentrations of the discharging species at the surface of the electrode and in the bulk of the solution, respectively, j_{o} is "exchange current density" related to the rate constant of the deposition process, and α_{a} and α_{c} are anodic and cathodic transfer coefficients related to the mechanism of discharge (note that for a cathodic process both η and j acquire negative signs. Also note that the current densities are divided by arbitrarily chosen unit current j^{o} in order to obtain dimensionless values for further use).

If the discharge of depositing species is sufficiently slow so that their supply to the electrode surface occurs without difficulty, the concentration c virtually does not deviate from c_{o}, and such a case is termed "activation controlled" deposition with the rate-determining step being the activation energy of the discharge process. At any cathodic overpotential larger than −40 mV, the first term in Eq. (1.19) becomes negligible, so that this equation can be transformed into a simpler one, known as the Tafel equation:

$$\eta = a - b\log\left(-\frac{j}{j^{o}}\right), \tag{1.20}$$

where the Tafel constant a is

$$a = \frac{2.3RT}{\alpha_{c}F}\log\left(\frac{j_{o}}{j^{o}}\right), \tag{1.21}$$

while the slope of the linear dependence obtained from a plot η versus $\log(-j)$ (Tafel slope) is

$$b = \frac{2.3RT}{\alpha_{c}F}. \tag{1.22}$$

The above reasoning applies equally and independently to both metals (A) and (B), j_{A} and j_{B}, and the total current density being $j_{alloy} = j_{A} + j_{B}$.

It should be stated here that the concept of overpotential is related to the reversible potential of a pure metal in a given solution. In the case of codeposition of two metals and the formation of a phase $A_{x}B_{(1-x)}$, this potential has no physical meaning since it represents an arbitrary point to which j_{o} is related.

Typical cases of activation-controlled codeposition of the metals A (j_{A}) and B (j_{B}), presented as polarization curves for pure metals and an alloy phase (j), are shown in Fig. 1.6.

The Tafel functions, presented in Fig. 1.7, indicate linear relationships between the logarithm of the partial current densities and the electrode potential. When this

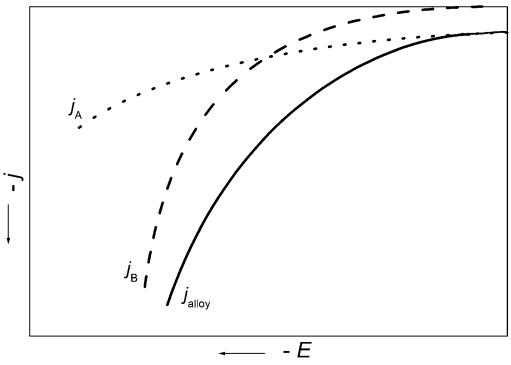

Fig. 1.6 Typical cases of activation-controlled codeposition of the metals A (j_A) and B (j_B), presented as polarization curves for pure metals and an alloy phase ($j_{alloy} = j_A + j_B$) (Reprinted from [1] with the permission of Springer)

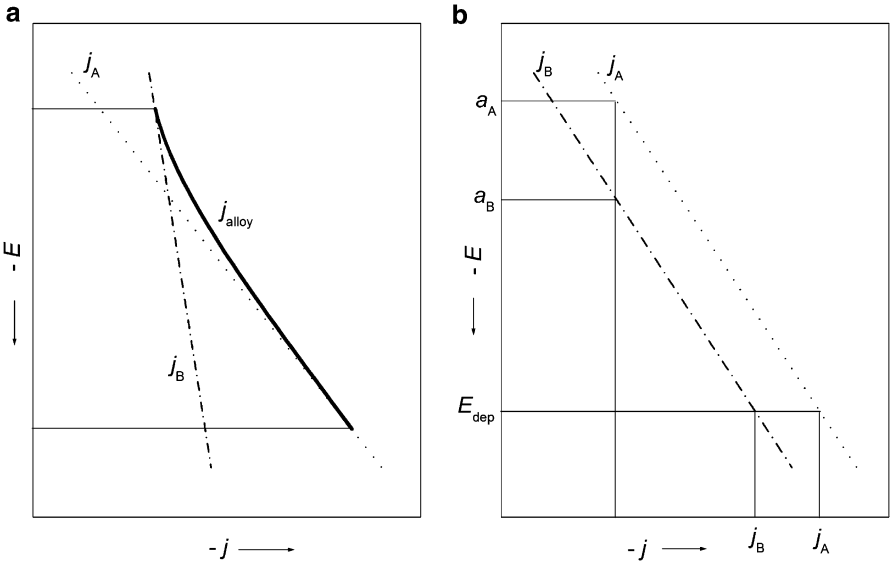

Fig. 1.7 Tafel functions for activation-controlled codeposition of the metals A (j_A) and B (j_B) and an alloy (j_{alloy}). (**a**) Different slopes of Tafel functions for pure metals deposition. (**b**) The same slopes of Tafel functions for pure metals deposition (Reprinted from [1] with the permission of Springer)

is the case, the total current density j_{alloy} cannot be a linear function of potential in the region in which the two partial current densities are comparable, since $\log (j_A + j_B) \neq \log j_A + \log j_B$ (Fig. 1.7a). When the Tafel function of the total current density merges with one or the other partial current density line, then one or the other metal is obtained virtually pure. In the extreme case in which the Tafel slopes for both depositing metals are equal, as shown in Fig. 1.7b, the difference between $\log j_A$ and $\log j_B$ remains constant, i.e., the composition of the alloy is constant at all potentials. In such a case the actual composition of the alloy depends on the difference between the values of the Tafel constants (a) for the two metals.

Considering the values of the Tafel constants and Tafel slopes, it is possible to analyze the factors determining the deviation of the metal ratio in the alloy from the metal ratio in solution. At any constant potential following relation is valid:

$$a_{\mathrm{A}} - b_{\mathrm{A}} \log\left(-\frac{j_{\mathrm{A}}}{j_{\mathrm{o}}}\right) = a_{\mathrm{B}} - b_{\mathrm{B}} \log\left(-\frac{j_{\mathrm{B}}}{j_{\mathrm{o}}}\right). \tag{1.23}$$

According to Eq. (1.6) one can derive:

$$\log\frac{x_{\mathrm{A}}}{x_{\mathrm{B}}} = \log\left(\frac{pj_{\mathrm{A}}}{qj_{\mathrm{B}}}\right) = \left[\left(\frac{a_{\mathrm{A}}}{b_{\mathrm{A}}} - \frac{a_{\mathrm{B}}}{b_{\mathrm{B}}}\right) - \left(\frac{b_{\mathrm{B}} - b_{\mathrm{A}}}{b_{\mathrm{A}} b_{\mathrm{B}}}\right) E\right] \frac{p}{q}. \tag{1.24}$$

Returning to the linear coordinates one obtains:

$$\frac{x}{1-x} = \frac{x_{\mathrm{A}}}{x_{\mathrm{B}}} = \frac{(j_{\mathrm{o}})_{\mathrm{A}} pa(\mathrm{A}^{\mathrm{p}+})^{(\alpha_{\mathrm{c}})_{\mathrm{A}}/p}}{(j_{\mathrm{o}})_{\mathrm{B}} qa(\mathrm{B}^{\mathrm{q}+})^{(\alpha_{\mathrm{c}})_{\mathrm{B}}/q}} \exp\left(\frac{RT}{F}\right) \left\{\left[(\alpha_{\mathrm{c}})_{\mathrm{A}} E^{\Theta}(\mathrm{A}^{\mathrm{p}+}/\mathrm{A}) - (\alpha_{\mathrm{c}})_{\mathrm{B}} E^{\Theta}(\mathrm{B}^{\mathrm{q}+}/\mathrm{B})\right] - \frac{(\alpha_{\mathrm{c}})_{\mathrm{A}} - (\alpha_{\mathrm{c}})_{\mathrm{B}}}{(\alpha_{\mathrm{c}})_{\mathrm{A}}^{\,2} (\alpha_{\mathrm{c}})_{\mathrm{B}}^{\,2}}\right\}. \tag{1.25}$$

Hence, it appears that the composition of the alloy follows a complex dependence on the metal ratio, involving all the thermodynamic and kinetic parameters determining activation-controlled codeposition [1].

As shown in Fig. 1.7 the Tafel lines are meant to pertain to the deposition of pure metals under the assumption that alloying does not change the Tafel constants and that the current density for alloy deposition should be a sum of partial current densities for pure metals. However, in practice, deviation from such behavior has been recorded, and an attempt to explain this phenomenon has been reported by Gorbunova and Polukarov [8] on an extreme case in which surface diffusion of A across the grains of B and nucleation of new grains of A are strongly inhibited.

An example for this type of alloy deposition is presented in Fig. 1.33 for the system Ag–Cd (cf. Sect. 1.3.3.3).

1.2.3.3 Regular Codeposition

Regular codeposition assumes transport-controlled codeposition in which diffusion of metal ions of both metals is a rate-determining step in the overall codeposition reaction.

Under steady state conditions of deposition the diffusion is governed by Fick's first law [22]:

$$\frac{c}{c_o} = \frac{j_L + j}{j_L} \tag{1.26}$$

with

$$j_L = \frac{zFD}{\delta} c_o, \tag{1.27}$$

where D is the diffusion coefficient of the depositing species and δ is the Nernst diffusion layer thickness.

Introducing Eq. (1.26) into Eq. (1.19) and rearranging following relation is obtained:

$$j = \frac{j_o\left[\exp\left(\frac{\alpha_a F}{RT}\eta\right) - \exp\left(-\frac{\alpha_c F}{RT}\eta\right)\right]}{1 + \frac{j_o}{j_L}\exp\left(-\frac{\alpha_c F}{RT}\eta\right)}. \tag{1.28}$$

At increasing values of overpotential, the second term in the denominator becomes overwhelming and the current density tends to a potential-independent diffusion limiting one, j_L.

Under the conditions of diffusion control, a plot of E versus log $[(-j_L/j) - 1]$ should be made instead of the regular Tafel plot, and the relationship should be linear with the slope of $(2.3RT/\alpha_c F)$.

One of the cases of regular codeposition is the deposition of Ag–Pd alloy from high concentration chloride (12 M LiCl) containing bath [23]. Polarization curves for the deposition of Ag–Pd alloy from the solution containing 0.005 M $PdCl_2$ + 0.05 M AgCl + 12 M LiCl + 0.1 M HCl ($t = 80$ °C), recorded onto rotating glassy carbon electrode under the conditions of stationary (RPM = 0) and convective (RPM = 200) diffusion are presented in Fig. 1.8a. The Pd deposition commences at about 0.07 V vs. SCE, while the codeposition of Ag begins at about −0.07 V vs. SCE. A well-defined diffusion limiting current densities for Pd (j_L(Pd)) and alloy (j_L(alloy)) deposition, representing actually the sum of j_L(Pd) and j_L(Ag), could be detected on the polarization curves, indicating that the j_L(Ag) is lower than that of Pd (taking into account that the concentration of AgCl is ten times higher than that of $PdCl_2$) and that the diffusion coefficient for Ag deposition is lower than that for Pd. This is confirmed in Fig. 1.8b. The deposition of Pd occurs by the reduction of $[PdCl_4]^{2-}$, while the deposition of Ag occurs by the reduction of $[AgCl_4]^{3-}$.

From the slopes of the linear j_L versus $\omega^{1/2}$ dependences [23] (Fig. 1.8b), confirming that the diffusion of both species obeys Levich's equation:

$$j_L = 0.62zFD^{2/3}\nu^{-1/6}c_o\omega^{1/2} \tag{1.29}$$

(ν—kinematic viscosity, ω—rotation speed), corresponding values of D for both species are obtained: $D([AgCl_4]^{3-}) = 5.5 \times 10^{-6}$ cm^2 s^{-1} and $D([PdCl_4]^{2-}) = 1.8 \times 10^{-5}$ cm^2 s^{-1}.

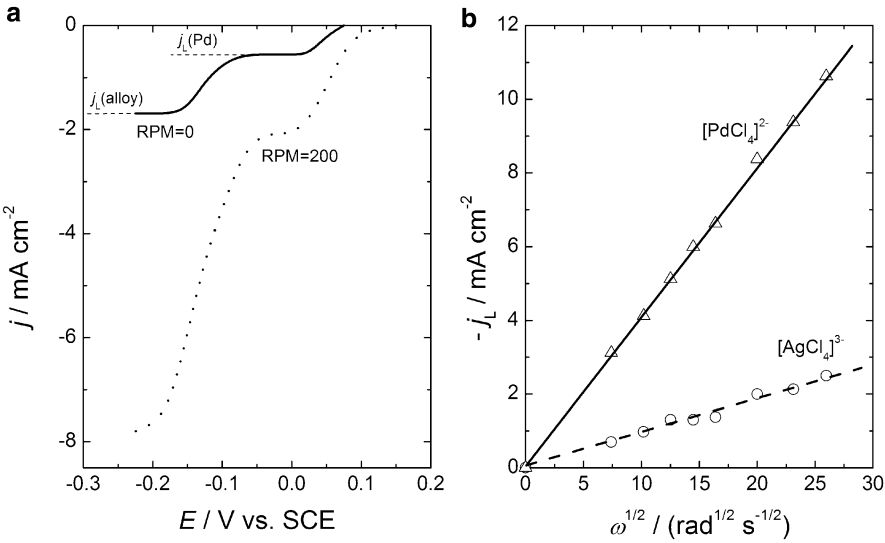

Fig. 1.8 (**a**) Polarization curves for the deposition of Ag–Pd alloy from the solution containing 0.005 M $PdCl_2$ + 0.05 M AgCl + 12 M LiCl + 0.1 M HCl ($t = 80$ °C), recorded onto rotating glassy carbon electrode. (**b**) The j_L versus $\omega^{1/2}$ dependences for pure Ag and pure Pd deposition onto rotating glassy carbon electrode from the solutions containing 0.005 M $PdCl_2$ + 12 M LiCl + 0.1 M HCl and 0.005 M AgCl + 12 M LiCl + 0.1 M HCl ($t = 80$ °C) (Reprinted from [23] with the permission of Serbian Chemical Society)

1.2.3.4 Anomalous Codeposition

According to Brenner's classification [4], anomalous codeposition is characterized by the fact that the less noble metal deposits before the more noble one as the potential is driven cathodic. As a consequence, the content of the less noble metal in the alloy is higher than its content in the solution.

An excellent example [24] is found in the case of Co–Ni alloy deposition. Pure Co and pure Ni were deposited at RPM = 1,000 onto a gold disc electrode from the solutions containing 0.2 M $CoSO_4$ + 0.2 M $Na_3C_6H_5O_7$ and 1 M $NiSO_4$ + 0.2 M $Na_3C_6H_5O_7$, respectively. For deposition of their alloys of different compositions, only the concentration of Co^{2+} has been changed, being 0.005, 0.01, 0.025, 0.05, and 0.2 M, respectively. Alloy layers of different compositions of the thickness of approximately 0.34 μm were obtained by galvanostatic deposition at two different current densities [$j = -2.5$ mA cm^{-2} (○) and $j = -28.5$ mA cm^{-2} (□)] to the same amount of charge ($Q_{dep} = -1$ C cm^{-2}). Polarization curves for pure metals deposition (Co and Ni) and Co–Ni alloy deposition (alloy) from the solution containing 0.025 M $CoSO_4$ + 1 M $NiSO_4$ + 0.2 M $Na_3C_6H_5O_7$ are presented in Fig. 1.9a (all other polarization curves for Co–Ni alloy deposition are placed between that for Ni and that for alloy—shaded area). As can be seen all polarization curves for Co–Ni alloy deposition are placed at more positive potentials than either of pure metals, which is clear indication for the anomalous codeposition of these two metals.

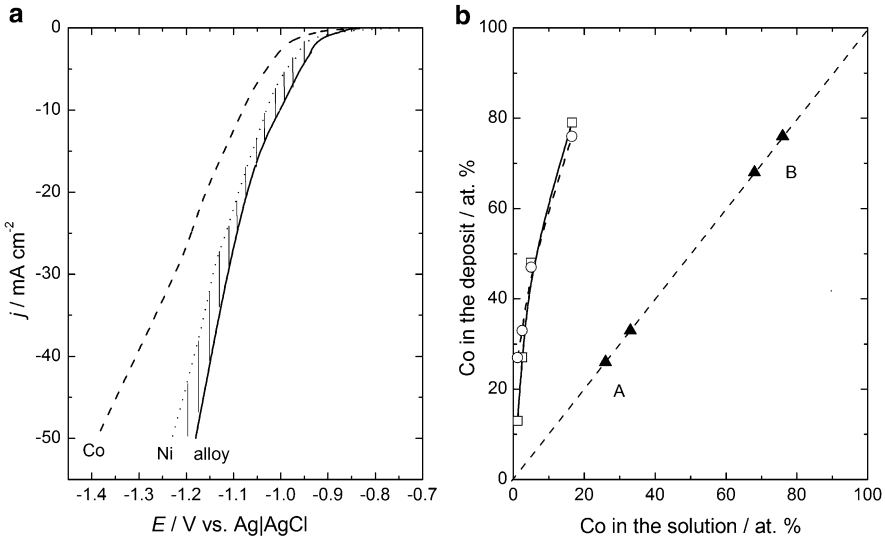

Fig. 1.9 (**a**) Polarization curves (corrected for IR drop) for the deposition of pure metals (Co and Ni) and Co–Ni alloy at the gold disc electrode (RPM = 1,000) obtained from the solutions: 0.2 M $CoSO_4$ + 0.2 M $Na_3C_6H_5O_7$ (Co); 1 M $NiSO_4$ + 0.2 M $Na_3C_6H_5O_7$ (Ni); 0.025 M $CoSO_4$ + 1 M $NiSO_4$ + 0.2 M $Na_3C_6H_5O_7$ (alloy). (**b**) Brenner's diagram for the system Co–Ni: samples obtained at $j = -2.5$ mA cm^{-2} (*open circle*) and at $j = -28.5$ mA cm^{-2} (*open square*) (Reprinted from [24] with the permission of Elsevier)

After deposition all Co–Ni alloy samples were dissolved in HCl, and the amounts of Co and Ni were determined by the AAS technique. It was found that the content of Co in the deposit increases with increasing concentration of Co^{2+} ions in the solution, changing from ~8 to ~80 at.%. The Brenner's diagram presented in Fig. 1.9b clearly shows pronounced anomalous codeposition.

Different explanations for such behavior are offered in the literature [4]. The most likely one appears to be "the hydroxide suppression mechanism" [25–28]. According to this concept, coevolution of hydrogen during the deposition causes an increase of pH at the electrode/solution interface, producing hydrolysis of less noble metal species and their precipitation as a layer of solid hydroxide. Formed hydroxide layer provides a good supply of ions of the less noble metal for their discharge and deposition, but suppresses the transport of species of the more noble metal to the cathode surface, causing anomalous codeposition.

1.2.3.5 Induced Codeposition

While it has been shown that Mo, W, Ti, and Ge cannot be separately deposited from aqueous solutions, they can be codeposited with the iron-group metals (Fe, Ni, Co) in the presence of appropriate complexing agents. This alloy-type deposition was defined by Brenner [4] as induced codeposition.

System Mo–Ni

In most of the papers concerning the process of induced codeposition of Ni and Mo, where molybdenum was present in the form of molybdate ion (MoO_4^{2-}), it was assumed that both metals were reduced to a metallic state, producing a Mo–Ni alloy coating. The most probable mechanism of alloy deposition was proposed by Podlaha and Landolt [29–31] and Marlot et al. [32]. Their investigations were performed under controlled mass transport conditions (rotating cylinder electrode). It was shown that mass transport control is an important factor for induced codeposition process. In a nickel-rich electrolyte molybdenum deposition is mass transport limited and the alloy composition is strongly influenced by the electrode rotation rate, while in a molybdenum-rich electrolyte the rate of molybdenum deposition is limited by the flux of nickel ions and alloy composition is independent of hydrodynamic effects [29]. The model assumes that nickel deposition occurs on the surface not covered by the molybdate reaction intermediate, by direct reduction of nickel species (all of them being complex of Ni^{2+} cations with the citrate anions) independently on the molybdate reaction, which can occur only in the presence of nickel species [29–32]. The model of Mo–Ni alloy deposition is described by following reduction reactions [30]:

$$[Ni(C_6H_5O_7)]^- + 2e^- \rightarrow Ni(s) + (C_6H_5O_7)^{-3} \tag{1.30}$$

$$MoO_4{}^{-2} + [Ni(C_6H_5O_7)]^- + 2H_2O + 2e^- \rightarrow [Ni(C_6H_5O_7)MoO_2]_{ads}{}^- + 4OH^- \tag{1.31}$$

$$[Ni(C_6H_5O_7)MoO_2]_{ads}{}^- + 2H_2O + 4e^- \rightarrow Mo(s) + [Ni(C_6H_5O_7)]^- + 4OH^- \tag{1.32}$$

$$H_2O + e^- \rightarrow \tfrac{1}{2}\, H_2 + OH^- \tag{1.33}$$

assuming that the alloy deposition is always accompanied by the simultaneous hydrogen evolution [reaction (1.33)]. This model has been confirmed by in situ surface Raman spectroscopic studies, by revealing existence of adsorbed intermediate $[Ni(C_6H_5O_7)MoO_2]_{ads}{}^-$ [33].

It was later shown for the Mo–Ni–O powder electrodeposition [34] that this mechanism is only partially correct and that among metallic Ni and Mo, the MoO_3 phase is also deposited. Taking into account that NiO, MoO_3, and $MoNi_4$ phases were detected in as-deposited samples by transmission electron microscopy (TEM), it is obvious that the mechanism of alloy deposition similar to the one presented by Eqs. (1.30, 1.31, 1.32, and 1.33) could be applied for the formation of $MoNi_4$ phase only, since it assumes complete reduction of both metal ions. By the analogy with the mechanism proposed by Podlaha and Landolt [29–31], it was suggested that the $MoNi_4$ phase could be formed by the following mechanism [35]:

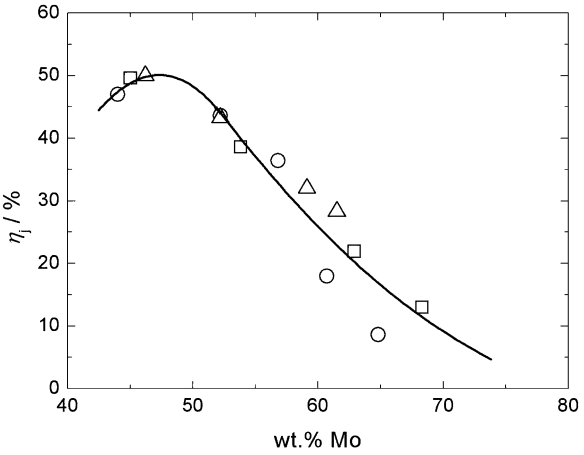

Fig. 1.10 Dependence of η_j on alloy composition (wt.% Mo); (*open square*) the influence of the $Na_4P_2O_7$ concentration; (*open circle*) the influence of the $FeCl_3$ concentration; (*open triangle*) the influence of the current density for alloy deposition (Reprinted from [36] with the permission of Serbian Chemical Society)

$$\left[Ni(NH_3)_3\right]^{2+} + 2e^- \rightarrow Ni(s) + 3NH_3 \tag{1.34}$$

$$MoO_4{}^{2-} + \left[Ni(NH_3)_3\right]^{2+} + 2H_2O + 2e^- \rightarrow \left[Ni(NH_3)_3MoO_2\right]_{ads}{}^{2+} + 4OH^- \tag{1.35}$$

$$\left[Ni(NH_3)_3MoO_2\right]_{ads}{}^{2+} + 2H_2O + 4e^- \rightarrow Mo(s) + \left[Ni(NH_3)_3\right]^{2+} + 4OH^- \tag{1.36}$$

The most probable mechanism for the MoO_3 phase formation is [34]:

$$MoO_4{}^{2-} + \left[Ni(NH_3)_3\right]^{2+} + H_2O + 2e^- \rightarrow MoO_3 + Ni(s) + 3NH_3 + 2OH^- \tag{1.37}$$

System Fe–Mo [36]

The Fe–Mo alloy coatings were deposited onto mild steel substrate from the solution containing $FeCl_3$, Na_2MoO_4, $Na_4P_2O_7$, and $NaHCO_3$, pH 9.3. Depending on the concentrations of $FeCl_3$, $Na_4P_2O_7$, and Na_2MoO_4, as well as the applied current density, the wt.% of Mo in the coatings (approximate thickness 20 μm) changed from about 45 wt.% to about 70 wt.%, while the current efficiency (η_j) varied from about 10 % to 50 %, as shown in Fig. 1.10. It should be stated that in all samples a certain (in some cases significant) amount of oxygen has been detected, but this was neglected assuming that the mechanism for induced codeposition defined by Eqs. (1.30, 1.31, 1.32, and 1.33) is operative and, accordingly, only percentages of Fe and Mo were taken into account [36].

Typical morphology of the coatings deposited at different current densities is presented in Fig. 1.11, characterized with nodular surface and large cracks. By the

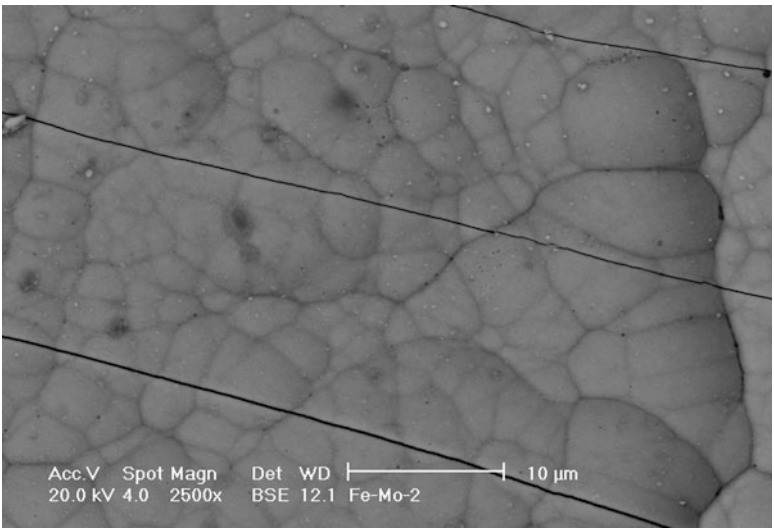

Fig. 1.11 Typical morphology of the Fe–Mo alloy coatings deposited at different current densities

Table 1.2 Composition of the Fe–Mo alloy surfaces, obtained by the EDS analysis, as a function of the deposition current density

j_{dep} (mA cm^{-2})	at.% O	at.% Mo	at.% Fe
−20	61.20	17.51	21.29
−50	34.05	27.08	38.87
−100	25.80	25.24	48.96

EDS analysis of the Fe–Mo alloy surfaces, it was found that their composition depends on the deposition current density, as shown in Table 1.2. Considering these results it appears that the amount of MoO_3 in the deposit decreases with the increase of the deposition current density (lower percentage of oxygen), indicating that the mechanism predicted by Eqs. (1.30, 1.31, and 1.32) and (1.34, 1.35, and 1.36) for Ni–Mo, prevails at higher current densities, while the mechanism for MoO_3 formation prevails at lower current densities of Fe–Mo alloy deposition.

1.3 Characterization of Electrodeposited Alloys by Electrochemical Techniques

1.3.1 Basic Concepts

The most common technique for phase identification in alloys is X-ray technique. The application of the X-ray technique on electrodeposited alloys is very often limited by the size of crystals, since in electrodeposited alloys they are often very

small (lower than 10 nm) which is under the limit of detection in conventional X-ray technique. Accordingly, such crystallites appear on the diffractograms as amorphous and must be investigated by the expensive and often not available TEM technique in order to be identified. Hence, it is desirable to use some other, much simpler and less expensive technique for identification of phases in deposited alloys. It appeared that electrochemical techniques, galvanostatic dissolution and anodic linear sweep voltammetry (ALSV), could be used for successful identification of phases in electrodeposited alloys [1].

The first attempt of the use of an electrochemical technique for characterization of a deposited alloy was made in 1928 in order to determine the thickness of metallic coatings [37, 38]. Using this method it was possible to determine the thickness of the coating and that of the intermediate layer between the coating and substrate, as well as to obtain data about the phase composition of the coating. Since then, electrochemical techniques have been extensively used for investigating processes of alloy dissolution [39–48]. In all of these cases bulk alloys were investigated, and the discrepancies between the obtained results were significant.

At the beginning of nineties, three laboratories reported attempts to determine the phase composition by complete dissolution of a thin layer (up to 10 μm) of a deposited alloy [49–62, 64, 65, 72, 79, 80], using different techniques: galvanostatic [50, 52], potentiostatic [57, 58, 61], and ALSV [49, 51, 57–62, 64, 65, 72, 79, 80].

1.3.2 ALSV technique

The ALSV technique is based on the application of linear sweep voltammetry at low sweep rate of 1 mV s^{-1} during the dissolution of thin layer of deposited alloy. After deposition of a thin layer of an alloy (up to 10 μm, recommendable about 1 μm) from the solution containing ions of both metals (constituents of the alloy) onto glassy carbon, gold, silver, or platinum substrates in one cell, working electrode, together with the deposit, is transferred into another cell containing only supporting (neutral) electrolyte, and/or ions of the less noble metal of the two, in which the alloy coating is completely dissolved. If the ions of the less noble metal are present in such solution, usually the reference electrode is less noble metal in the solution of corresponding ions. In the case of neutral electrolyte any reference electrode could be used, but the starting potential for alloy dissolution should be reversible potential of the less noble metal [1].

1.3.2.1 Conditions for Phase Detection in the Thin Layer of Deposited Alloys

Following conditions must be fulfilled for successful phase detection in deposited alloys by the ALSV technique:

- It is important to dissolve the entire alloy sample, since only in such a case eventual diffusion of alloy constituents in the solid phase will not influence the process of alloy dissolution by masking of some phases by other ones. If there are some solid-state diffusion limitations, they can be overcome by using either long time polarization (galvanostatic or potentiostatic techniques) or very low sweep rate in the ALSV technique;
- The processes of passivation or replacement must be prevented during the dissolution of alloy. This can be achieved by a proper choice of the solution for alloy dissolution. The use of simple salt solutions (such as NaCl, Na_2SO_4, and $NaClO_4$) with pH values in the range $3 \leq pH \leq 6$ or simple salt solutions with addition of small concentration of the less noble metal (up to 10^{-2} M) is recommended [1];
- It is much better to use techniques in which potential is controlled since galvanostatic responses are not always well defined [50, 52]. Particularly, good results were obtained with the application of ALSV technique [51, 53, 57–62, 64, 65, 72, 79, 80].
- Concerning the process of the more noble metal deposition/dissolution, two cases can exist in the application of the ALSV technique: (1) The deposition/dissolution process of the more noble metal is reversible. Accordingly, during the dissolution of alloy the ions of the more noble metal must reprecipitate on the spot (since the potential is more negative than the reversible one of the more noble metal); (2) the deposition/dissolution of the more noble metal is irreversible and the dissolution of the more noble component starts at the potentials more positive than its reversible potential. Accordingly, no reprecipitation of the more noble metal would take place.

1.3.3 Characteristics of the ALSV Responses for Dissolution of Different Types of Alloys

The shape of the ALSV of alloy dissolution could be predicted by consideration of the phase diagram of alloys and the Gibbs energies of phases appearing in the system. Different types of alloys (eutectic, solid solution, alloys with intermediate phases, and/or intermetallic compounds) will possess different shapes of the ALSV responses.

1.3.3.1 Eutectic-Type Alloys

Since the interaction (miscibility) between the components in the solid phase of the eutectic-type alloys is absent or negligible, the Gibbs energies of each constituent should be the same as that of the corresponding pure metal. Accordingly, the reversible potential of each constituent in the alloy should be virtually the same as that of pure metal of the same grain size. In such a case, the ALSV should be

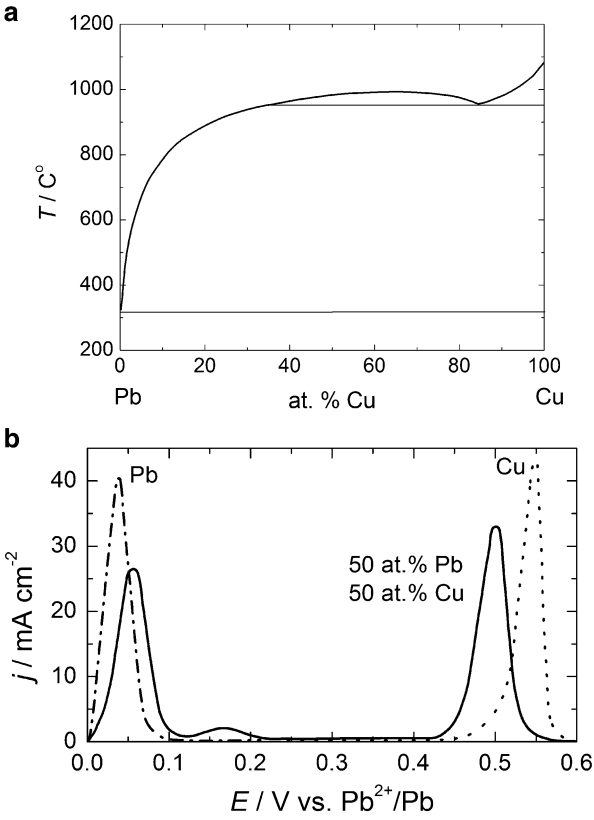

Fig. 1.12 (**a**) Phase diagram of the system Cu–Pb. (**b**) ALSV's of dissolution of pure metals (Cu—*dotted line*, Pb—*dash dot line*) and Cu–Pb alloy (*solid line*) containing approximately 50 at. % Pb and 50 at. % Cu. Conditions of dissolution: 0.01 M Pb^{2+} + 1 M HBF_4, $v = 1$ mV s^{-1}, RPM = 0 (Reprinted from [1] with the permission of Springer)

characterized by two separate dissolution peaks, each of them reflecting dissolution of the corresponding pure metal and appearing at potentials more positive than the reversible potential of that particular metal. The two peaks might overlap only if the difference between the reversible potentials of these two metals is very small and the thickness of a deposited alloy is high (over 1 μm).

System Cu–Pb [51]

The phase diagram for the system Cu–Pb [67] is shown in Fig. 1.12a, while the ALSV's of Cu, Pb, and Cu–Pb alloy dissolution, recorded in the solution containing 0.01 M Pb^{2+} + 1 M HBF_4, $v = 1$ mV s^{-1}, RPM = 0, are presented in Fig. 1.12b. Pure metals were deposited onto rotating disc electrode (RDE) made of glassy carbon (GC) at RPM = 1,000: Pb was deposited from the solution containing 0.1 M Pb^{2+} + 1 M HBF_4, $E = -0.04$ V vs. Pb^{2+}/Pb; Cu was deposited from the solution containing 0.05 M Cu^{2+} + 0.2 M H_2SO_4, $E = -0.05$ V vs. Ag/AgCl; Cu–Pb alloy was deposited from the solution containing 0.05 M Cu^{2+} + 0.01 M Pb^{2+} + 1 M HBF_4, $E = -0.52$ V vs. Ag/AgCl ($j_{dep} \approx -7.5$ mA cm^{-2}). As can be seen in

Fig. 1.12b the peaks of Cu and Pb dissolution from the alloy are well defined and separated, and their dissolution potentials are close to the dissolution potentials of pure metals [case (1) of Sect. 1.3.2.1]. Slightly, more positive peak potential for the dissolution of Pb from the alloy is due to diffusion of Pb from the bulk of alloy, while slightly more negative peak potential for the dissolution of Cu from the alloy is the consequence of the fact that, after the dissolution of all Pb from the alloy, the remaining layer of pure Cu is more porous and its dissolution takes place at more negative potentials. A small peak at about 0.15 V vs. Pb^{2+}/Pb represents the dissolution of a solid solution of Pb in Cu, which could be formed only in electrodeposited alloys [63], with up to 10 wt.% of Pb being dissolved in Cu. Such behavior indicates that deposited alloys could be characterized by the presence of some phases not indicated in the phase diagram of the system. At the same time, it is often the case that these phases cannot be detected by the X-ray technique, while they are clearly defined on the ALSV of alloy dissolution (see further text).

System Cd–Zn [64, 65]

The phase diagram for the system Cd–Zn [67] is shown in Fig. 1.13a, while the ALSV's of Cd–Zn alloys dissolution of different compositions are presented in Fig. 1.13b. The alloys were deposited at different constant current densities (to a total charge of 1 C cm^{-2}) on a RDE made of Au (RPM = 1,000) from the solution containing 0.01 M $CdSO_4$ + 0.5 M $ZnSO_4$ + 0.01 M H_2SO_4. Their dissolution by the ALSV technique was performed in the solution containing 0.5 M Na_2SO_4 (pH 4), RPM = 0 [64, 65]. The composition of the alloys was calculated from the ratio of current densities of both metals: more noble metal (Cd) was deposited at its diffusion limiting current density, j_L(Cd), while the difference between the total current density, j_t and j_L(Cd), was ascribed to the current density for Zn deposition, j(Zn). The current efficiency for alloy deposition was calculated from the ratio of the charge recorded during the alloy dissolution, Q_{diss}(alloy) (obtained by the integration of the surface area under the ALSV response), and that for alloy deposition, Q_t(alloy), as $\eta_j = Q_{diss}(\text{alloy})/Q_t(\text{alloy})$. Accordingly, the molar ratio of the more noble metal in the alloy is expressed as [64, 65]

$$x(\text{Cd}) = \frac{j_L(\text{Cd})}{\eta_j j_t(\text{alloy})} = \frac{Q_t(\text{Cd})}{\eta_j Q_t(\text{alloy})} = \frac{Q_t(\text{Cd})}{Q_{diss}(\text{alloy})}, \tag{1.38}$$

while that for the less noble one was

$$x(\text{Zn}) = \frac{\left[\eta_j j_t(\text{alloy}) - j_L(\text{Cd})\right]}{\eta_j j_t(\text{alloy})} = \frac{\left[\eta_j Q_t(\text{alloy}) - Q_t(\text{Cd})\right]}{\eta_j Q_t(\text{alloy})} = \frac{\left[Q_{diss}(\text{alloy}) - Q_t(\text{Cd})\right]}{Q_{diss}(\text{alloy})}. \tag{1.39}$$

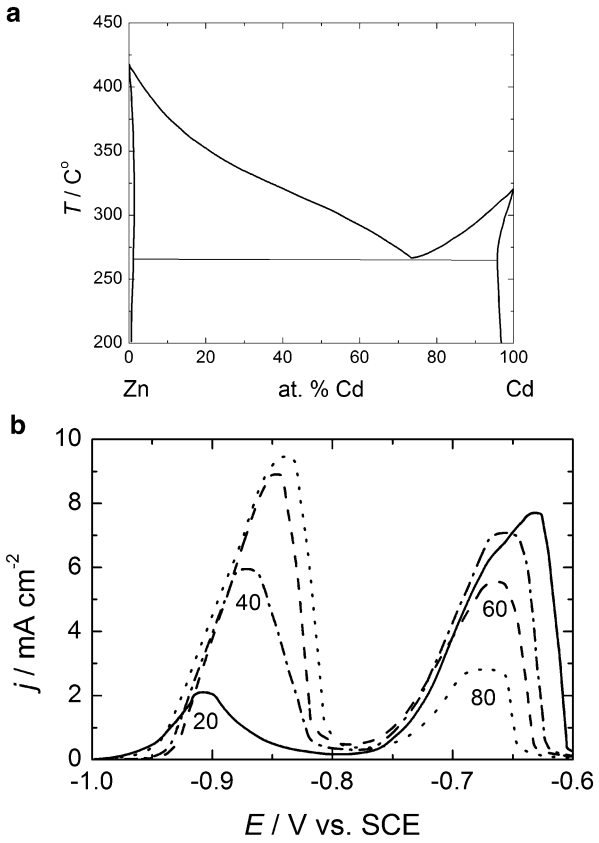

Fig. 1.13 (**a**) Phase diagram of the system Cd–Zn. (**b**) ALSV's of dissolution of Cd–Zn alloy of different compositions (at.% of Zn in the alloy marked in the figure). Conditions of dissolution: 0.5 M Na_2SO_4 (pH 4), $v = 1$ mV s^{-1}, RPM = 0 (Reprinted from [1] with the permission of Springer)

To express the molar ratio of each metal in the alloy by the ratio of their current densities for deposition, $\Delta = j_L(\mathrm{Cd})/j(\mathrm{Zn})$, it follows that

$$x(\mathrm{Cd}) = \frac{\Delta}{1+\Delta}, \tag{1.40}$$

$$x(\mathrm{Zn}) = \frac{1}{1+\Delta}. \tag{1.41}$$

The composition of alloys, i.e., the desired total current density for alloy deposition for the defined duration of the current pulse, was obtained by using Eqs. (1.38, 1.39, 1.40, and 1.41).

As can be seen in Fig. 1.13b the peaks of Zn and Cd dissolution are clearly separated [case (1) of Sect. 1.3.2.1] for all alloy compositions (at.% of Zn in the

alloys are marked in the figure), as in the case of the system Cu–Pb (Fig. 1.12b). By comparing the charge under the peaks for Cd and Zn dissolution on the ALSV's and their charges for deposition (taking into account η_j), it was found that $Q_{diss}(Zn)$ is smaller than $Q_{dep}(Zn)$, while $Q_{diss}(Cd)$ is higher than $Q_{dep}(Cd)$. This finding confirms the fact that in electrodeposited Cd–Zn alloys, supersaturated solid solution of Zn in Cd can be formed [66].

System Cd–Co [72]

According to the literature data [67], several attempts were made in order to obtain phase diagram for the system Cd–Co and none of them was successful, because it was not possible to prepare alloys with less than 94 wt.% and more than 10 wt.% Co [68]. In the case of melts with up to 10 wt.%, Co cooling curves showed only eutectic arrests at 316 °C. By the structural analysis of this melt, it was stated that an intermetallic phase is present in eutectic matrix [69]. Some authors claimed that $Cd_{23}Co_3$ intermetallic compound (having structure of γ-brass) was identified in this system [70], but it could not be proven by immersion of Co in a Cd melt at 700 °C [71]. Hence, at the moment no convincing data concerning the phase diagram for the system Cd–Co are available in the literature.

The Cd–Co alloy coatings [72] were deposited from sulfate electrolytes with different compositions: (1) 0.01 M $CdSO_4$ + 0.2 M $CoSO_4$ + 0.2 M H_3BO_3, (2) 0.02 M $CdSO_4$ + 0.2 M $CoSO_4$ + 0.2 M H_3BO_3 and (3) 0.02 M $CdSO_4$ + 0.4 M $CoSO_4$ + 0.2 M H_3BO_3. Pure Co was deposited in the solution containing 0.2 M $CoSO_4$ + 0.2 M H_3BO_3 and pure Cd from the solution (2) at the potential of pure Cd deposition (−0.75 V vs. SCE). All deposits were obtained under the conditions of convective diffusion, i.e., RPM = 1,000, while all ALSV's were recorded at the sweep rate of 1 mV s^{-1} in the 1 M NaCl solution (pH 2) at RPM = 0 (stationary electrode).

In Fig. 1.14a are compared ALSVs of pure Cd, pure Co, and Cd–Co alloy of approximate composition 50 at.% Cd − 50 at.% Co, all deposited to a constant charge of 1 C cm^{-2} (case (2) of Sect. 1.3.2.1). It appears that deposited Cd–Co alloy does not belong to the eutectic-type alloys since some new, unknown phase (Un), presented by the additional ALSV peak at about −0.32 V, has been formed. At a certain solution composition (0.02 M Cd^{2+} + 0.2 M Co^{2+} + 0.2 M H_3BO_3), certain deposition potential (−1.5 V), and certain amount of deposited alloy, the most pronounced peak is the peak of the unknown phase, Fig. 1.14b. Hence, it is possible to obtain the deposited Cd–Co alloy with the highest amount of the unknown phase in the system Cd–Co [72]. It should also be emphasized that the peak of Co dissolution is placed at significantly more positive potentials than the potential of its deposition (about −1.0 V). Accordingly, Co^{2+} ions cannot reprecipitate [case (2) of Sect. 1.3.2.1], as it was the case for Cu–Pb [51] and Cd–Zn [64, 65] systems.

Corresponding charges for the deposition of Cd and Co, obtained by the calculation of the Cd deposition charge using its diffusion limiting current density ($Q_{Cd} = j_L(Cd)\cdot t$) and Co deposition charge as $Q_{Co} = Q_{tot} - Q_{Cd}$, are presented

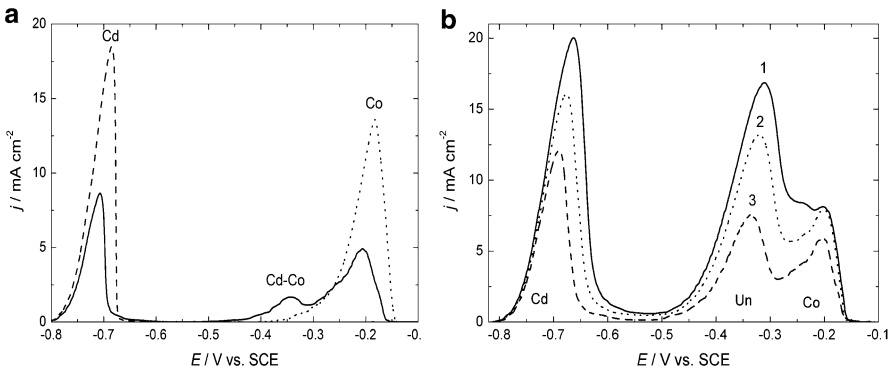

Fig. 1.14 (**a**) ALSV's recorded at $v = 1$ mV s^{-1} and RPM = 0 in the electrolyte of 1 M NaCl (pH 2) for pure Cd (*dashed line*), pure Co (*dotted line*), and Cd–Co alloy (*solid line*) deposited to a constant charge of 1 C cm^{-2} in the electrolyte containing 0.01 M $CdSO_4$ + 0.2 M $CoSO_4$ + 0.2 M H_3BO_3 at RPM = 1,000. (**b**) ALSV's recorded under the same conditions as those in (**a**) for deposits obtained at a potential of −1.5 V to the different charges of 14.8 C cm^{-2} (1), 10.7 C cm^{-2} (2), and 6.7 C cm^{-2} (3) in the electrolyte containing 0.02 M $CdSO_4$ + 0.2 M $CoSO_4$ + 0.2 M H_3BO_3 at RPM = 1,000 (Reprinted from [72] with the permission of Elsevier)

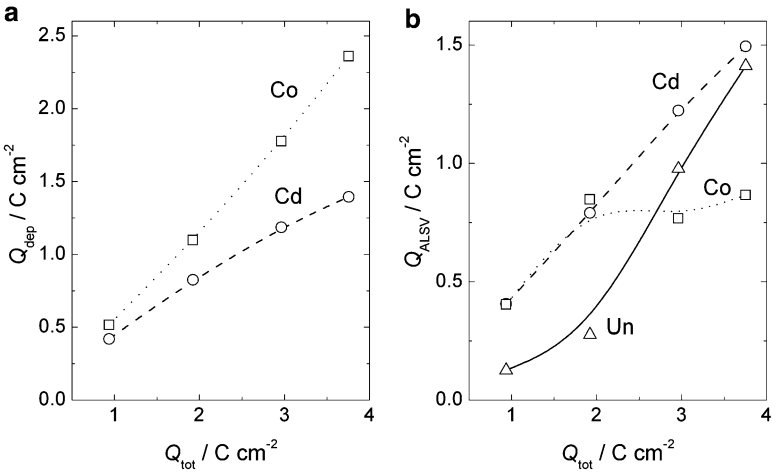

Fig. 1.15 (**a**) Deposition charges for Cd and Co as a function of the total charge for the alloys deposition. (**b**) Dissolution charges for Cd, Co, and unknown phase (Un), obtained by the integration of the charge under corresponding ALSV peaks, as a function of total charge for the alloys deposition (Reprinted from [72] with the permission of Elsevier)

in Fig. 1.15a. As can be seen with the increase of the total charge for alloy deposition, Q_{tot}, charges for both metals increase almost linearly. By the integration of the charge under corresponding peaks on the ALSV's, the charges for the dissolution of Cd, Co, and unknown phase (Un) are obtained. These charges, as a function of the Q_{tot}, are presented in Fig. 1.15b. It appears that the charge (amount)

for the unknown phase sharply increases with increasing Q_{tot} for the applied potential of alloy deposition (−1.3 V), while the charge for Co increases for $Q_{tot} \leq 2$ C cm^{-2} reaching its limiting value of about 0.8 C cm^{-2} at higher values of Q_{tot}. Such behavior indicates that the amount of the unknown phase increases on the account of the amount of both metals up to $Q_{tot} \approx 2$ C cm^{-2}, while at higher values of Q_{tot} its increase is mainly on the account of deposited Co, but certain limiting amount of Cd must be deposited for the unknown phase to be formed and seen on the ALSV. Taking into account these results, it is obvious that the unknown phase detected in the deposited alloy cannot be ascribed to the $Cd_{23}Co_3$ intermetallic compound [70], since it contains higher amount of Co than Cd and its peak is close to the peak of pure Co dissolution [72].

1.3.3.2 Solid Solution Type Alloys

In the case of solid solution type alloys, the prediction of the ALSV shape could be problematic, i.e., the dissolution can proceed through two separate peaks or through one peak. According to the literature [73] metal atoms in the ideal solid solutions should be randomly arranged. In reality, such alloys can also contain some short- and long-range ordered structures. Some alloys whose metals are totally miscible in the solid state, such as Au–Cu solid solution, possess "superlattice" structures ($AuCu_3$, AuCu, and Au_3Cu), and each of these types of "superlattices" could have different dissolution characteristics. On the other hand, if the Gibbs energy of mixing is not very high and if the potential sweep is sufficiently slow [1, 51], the less noble metal should dissolve completely at more negative potentials than the potential of dissolution of the more noble metal. In such a case at least two ALSV peaks should be expected, corresponding to the dissolution of both pure metals. The preceding peaks should represent the dissolution of the less noble metal only, assuming that, even if the two metals dissolved simultaneously in the preceding peaks (as is likely to happen with a solid solution), the more noble metal should immediately reprecipitate since its ions are formed at potentials more negative than the reversible potential of the more noble metal. Such theory, predicting two ALSV peaks, has been proposed in the literature [1, 51].

System Co–Ni, Ideal Solid Solution [24]

The phase diagram for the system Co–Ni [67] is shown in Fig. 1.16a, while the ALSV's of Co–Ni alloys dissolution of different compositions are presented in Fig. 1.16b. Considering deposition/dissolution characteristics of both metals (both are irreversible), this system cannot be assigned to either of the cases (1) or (2) of Sect. 1.3.2.1.

Pure Co and pure Ni were deposited onto gold disc electrode at RPM = 1,000 from the solution containing 0.2 M $CoSO_4$ + 0.2 M $Na_3C_6H_5O_7$ and 1 M $NiSO_4$ + 0.2 M $Na_3C_6H_5O_7$, respectively. For deposition of their alloys of different

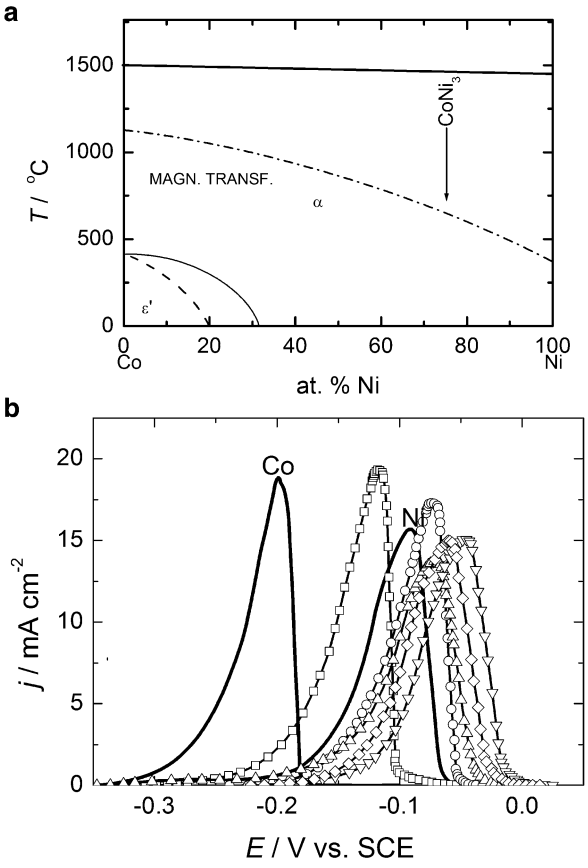

Fig. 1.16 (**a**) Phase diagram of the system Co–Ni. (**b**) ALSV's of dissolution of Co–Ni alloy of different compositions: *solid lines*—pure Co and pure Ni; *open square*—78.3 at.% Co; *open circle*—47.5 at.% Co; *open triangle*—25.2 at.% Co; *open inverted triangle*—12.9 at.% Co; *open diamond*—8.0 at.% Co. Conditions for dissolution: 1 M NaCl (pH 2), $v = 1$ mV s^{-1} (Reprinted from [24] with the permission of Elsevier)

compositions, only the concentration of Co^{2+} has been changed, being 0.005 M, 0.01 M, 0.025 M, 0.05 M, and 0.2 M, respectively (see Fig. 1.9). Alloy layers of different compositions of the thickness of approximately 0.34 μm were obtained by galvanostatic deposition at different constant current densities, but at the same amount of charge of 1 C cm^{-2}. All samples were dissolved in the solution 1 M NaCl (pH 2) by application of the ALSV technique on the stationary Au electrode (RPM = 0). The composition of alloy samples deposited at a constant current density to the amount of 1 mg and galvanostatically dissolved in 10 ml of 1 M HCl has been determined by the AAS technique [24].

Considering ALSV results presented in Fig. 1.16b, it could be concluded that the peak potentials of dissolution of pure metals are very close to each other

(the difference being about 0.1 V) and that all Co–Ni alloy samples dissolve through one ALSV peak only, indicating simultaneous dissolution of both metals from their alloy. Such behavior during the alloy dissolution is the consequence of the fact that the potentials of dissolution are much more positive than the potentials of Ni deposition (reduction of Ni^{2+} ions) so that it is not possible for Ni^{2+} ions to reprecipitate. It is interesting to note that the peaks of dissolution of Co–Ni alloys with less than 50 at.% Co are placed at potentials more positive than that of the more noble metal (Ni). Most of the data concerning the phase diagram of the system Co–Ni [74] state that these two metals form solid solutions at all compositions, while in one work the possibility of the formation of ordered $CoNi_3$ structure [75] has been predicted. For a new phase in the system, one would expect additional ALSV peak (as it is in the case in the system Ag–Pd, see text below), but in the case of Co–Ni alloys dissolution this is not the case.

Let us consider the standard potential of the phase $Co_xNi_{(1-x)}$. According to the existing literature [1], standard potential of such phase should be

$$E^{\Theta}\left(Co_xNi_{(1-x)}\right) = \frac{E^{\Theta}\left(Co^{2+}/Co\right) + E^{\Theta}\left(Ni^{2+}/Ni\right)}{2} - \frac{\mu^{\Theta}\left(Co_xNi_{(1-x)}\right)}{2F}. \quad (1.42)$$

In the case of the ideal solid solutions, the Gibbs energy is entirely defined by the entropy of mixing (the enthalpy, $\Delta H^{\Theta}{}_{i} = 0$), while the entropy of mixing depends on the composition of solid solution and the temperature

$$\mu_i^{\Theta}\left(Co_xNi_{(1-x)}\right) = -RT[x \ln x + (1-x) \ln (1-x)]. \quad (1.43)$$

In real systems this behavior is rather exceptional and usually mixing is endothermic or exothermic, i.e., ΔH^{Θ} is included and explained by the quasi-chemical model assuming that the heat of mixing (ΔH^{Θ}) is only due to the bond energies between adjacent atoms [73]. In such a case the Gibbs energy change upon mixing of a so-called regular solid solution is given by

$$\mu_i^{\Theta}\left(Co_xNi_{(1-x)}\right) = \Delta H^{\Theta}\left(Co_xNi_{(1-x)}\right) - RT[x \ln x + (1-x) \ln (1-x)], \quad (1.44)$$

where the heat of mixing $\Delta H^{\Theta}(Co_xNi_{(1-x)})$ is determined by the interatomic bonds and is given by the equation:

$$\Delta H^{\Theta}\left(Co_xNi_{(1-x)}\right) = N_a z \varepsilon x(1-x) \quad (1.45)$$

with N_a being Avogadro's constant, z is the number of bonds per atom, and ε is the bond energy.

This model is also rather limited, and in the real systems the actual arrangement of atoms will be a compromise that gives the lowest internal energy consistent with sufficient entropy, or randomness, to achieve the minimum Gibbs energy. Such a tendency can lead to a formation of ordered structures known as "superlattices,"

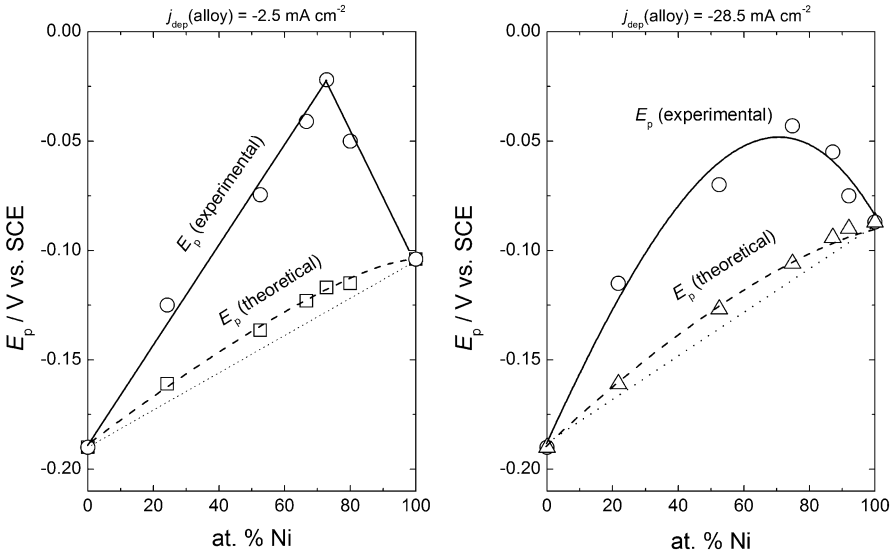

Fig. 1.17 Dependences of the ALSV peak potentials as a function of alloy composition for Co–Ni alloys deposited at different current densities (marked in the figure) (Reprinted from [24] with the permission of Elsevier)

which are clearly detected [73] in the system Au–Cu as Au_3Cu, AuCu, and $AuCu_3$. All the above considerations assume thermally prepared alloys obtained under equilibrium conditions. Since electrodeposited alloys are practically never obtained under equilibrium conditions [1], one can expect that the effects of the heat and entropy of mixing will be even more pronounced in the case of deposited alloys.

Using Eq. (1.42) the highest value of the entropy of 1.717 kJ mol^{-1} is obtained for $x = 0.5$ (for temperature of 25 °C), while the corresponding change of the standard potential of the $Co_xNi_{(1-x)}$ phase is only 9 mV. Hence, in such a case the standard potential of this phase should change linearly from that of Co, $E^{\Theta}(Co^{2+}/Co)$, to that of Ni, $E^{\Theta}(Ni^{2+}/Ni)$, while the contribution of μ^{Θ}_i is very small and causes very small deviation in the change of standard potential from linearity (see Fig. 1.17). Taking into account that it is not possible to determine reversible potentials of Co, Ni, and Co–Ni alloys from the dissolution characteristics represented by their ALSV's in Fig. 1.16b, and bearing in mind high irreversibility of the deposition/dissolution processes for both metals, an attempt was made to use ALSV peak potentials instead of the reversible potentials for dissolution of all components of the system [24]. In Fig. 1.17 are presented dependences of the ALSV peak potentials (E_p) as a function of the alloy composition (at.% Ni) for the alloys and pure metals deposited at different current densities. As can be seen theoretical and experimental dependences are different, with the most positive experimentally determined peak potentials recorded for the composition of approximately 75 at.% Ni ($CoNi_3$). The peak potential change is much better defined for the samples deposited at lower current density, $j_{dep}(\text{alloy}) = -2.5$ mA cm^{-2}.

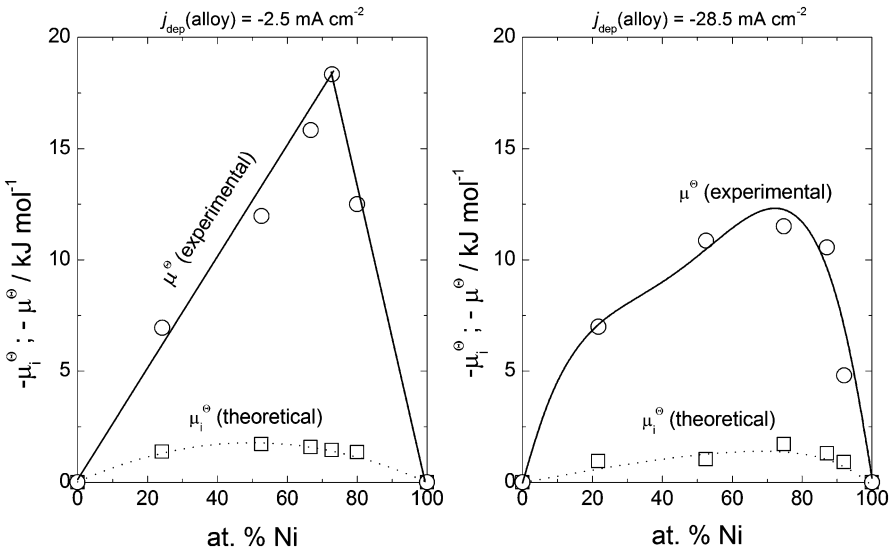

Fig. 1.18 Dependences of the μ^{Θ} and $\mu^{\Theta}{}_{i}$ as a function of alloy composition for Co–Ni alloys deposited at different current densities (j_{dep}(alloy)—marked in the figure) (Reprinted from [24] with the permission of Elsevier)

By expressing μ^{Θ} using E_p instead of E^{Θ} values in Eq. (1.5), it is possible to plot experimental and theoretical values for μ^{Θ} as a function of alloy composition, as shown in Fig. 1.18.

Hence, it could be concluded that even in the absence of additional ALSV peak for dissolution of "ordered structure" ($CoNi_3$), it is possible to predict the existence of such structure in the solid solution by proper analysis of the ALSV response.

System Ag–Pd [62]

The Ag–Pd alloys were deposited to a constant charge from the solution containing 0.005 M $PdCl_2$ + 0.04 M AgCl + 12 M LiCl + 0.1 M HCl (t = 50 °C) onto rotating Au disc electrode (RPM = 1,000) at constant current densities defined by the desired alloy composition [see Eqs. (1.38, 1.39, 1.40, and 1.41)]. Pure metals were deposited under the same conditions from two different solutions: Pd from the solution 0.001 M $PdCl_2$ + 12 M LiCl + 0.1 M HCl at the constant current density of −0.5 mA cm^{-2}; Ag from the solution 0.04 M AgCl + 12 M LiCl + 0.1 M HCl at the constant current density of −10.0 mA cm^{-2}. All deposited samples were dissolved by the ALSV technique in the solution 0.001 M AgCl + 12 M LiCl + 0.1 M HCl (RPM = 0).

The ALSV's of pure metals dissolution (Ag—dotted line, Pd—dashed line) and an alloy containing approximately 50 at.% Ag and 50 at.% Pd (solid line) are presented in Fig. 1.19a [case (1) of Sect. 1.3.2.1].

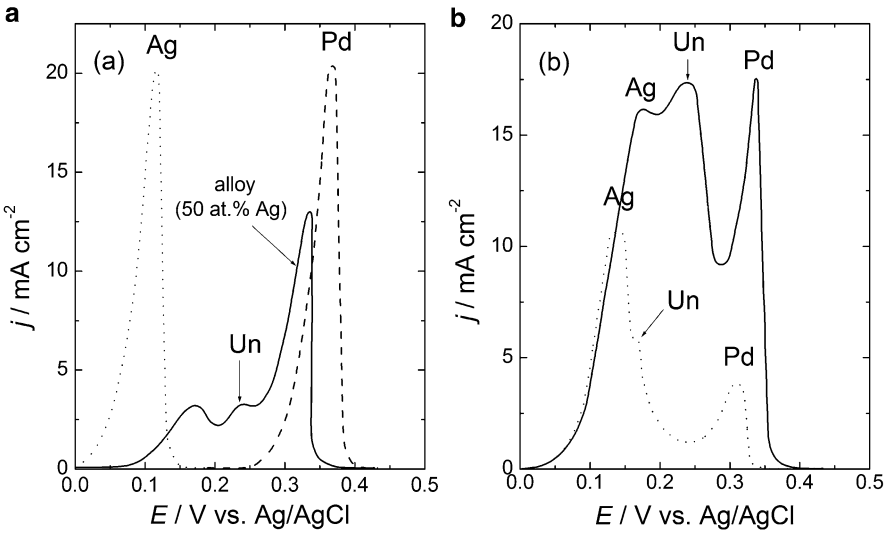

Fig. 1.19 (**a**) ALSV's recorded at $v = 1$ mV s^{-1} and RPM = 0 in the solution 0.001 M AgCl + 12 M LiCl + 0.1 M HCl for pure Ag (*dotted line*), pure Pd (*dashed line*), and Ag–Pd alloy (approximately, 50 at.% Ag and 50 at.% Pd—*solid line*) deposited to a constant charge of 1 C cm^{-2}. (**b**) ALSV's recorded under the same conditions as those in (**a**) for alloy containing 80 at.% Ag and 20 at.% Pd deposited to the different charges of 1.0 C cm^{-2} (*dotted line*) and 4.0 C cm^{-2} (*solid line*) (Reprinted from [62] with the permission of Elsevier)

As can be seen Ag and Pd dissolution peaks are well separated. The ALSV of an alloy containing approximately 50 at.% Ag and 50 at.% Pd is characterized by the presence of additional peak at about 0.24 V vs. Ag/AgCl (Un), while peak of pure Ag dissolution from the alloy is placed at more positive potentials (due to diffusion through the alloy matrix) and peak of Pd dissolution is positioned at more negative potentials (due to its porous structure—consequence of Pd reprecipitation). The peak of unknown phase (Un) is seen to depend on the amount of deposited alloy, as well as on the alloy composition, Fig. 1.19b. In the alloy with 80 at.% Ag deposited to the lower charge (1 C cm^{-2}, thinner deposit—dotted line) this peak is small and not well defined, while in the same alloy with higher thickness (4 C cm^{-2}—solid line) this peak is much bigger, indicating higher amount of this phase in the alloy. This finding [62] indicates that deposited Ag–Pd alloy is not a simple homogeneous solid solution [76, 77], as predicted by the phase diagram [67]. Confirmation of this finding is in accordance with the measurement of the microhardness of deposited Ag–Pd alloys, which was found to increase with increasing Ag content in the alloy [78]. Such behavior could only be explained by the presence of some intermetallic compound that possesses a higher value of microhardness than that of pure Pd. Since the microhardness of Pd is three times higher than that of Ag, the microhardness of their solid solutions should be somewhere in between. Hence, the unknown phase is most likely an intermetallic compound, formed only in the deposited Ag–Pd alloys.

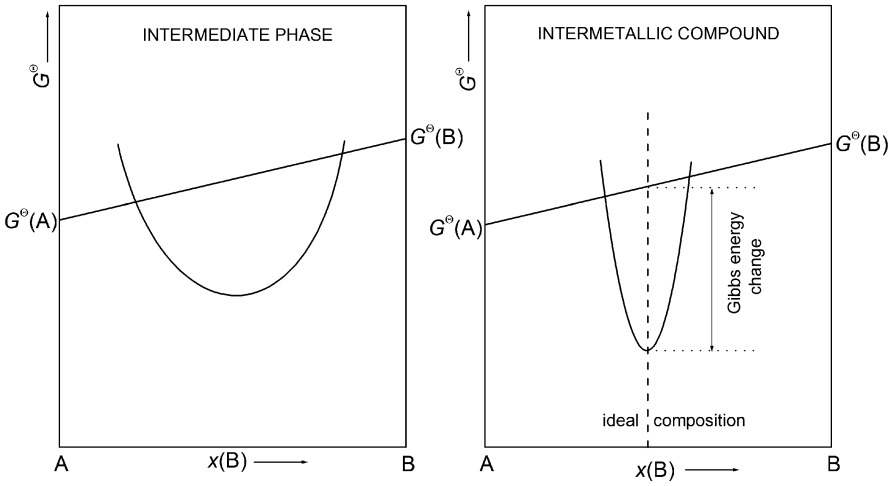

Fig. 1.20 Schematic representation of the change of Gibbs energy of intermediate phase and intermetallic compound as a function of alloy composition (Reprinted from [1] with the permission of Springer)

1.3.3.3 Alloys Characterized with Intermediate Phases and/or Intermetallic Compounds

It is known that the configuration of atoms that has minimum Gibbs energy after the mixing of two metals often does not have the same crystal structure as either of the pure metals. Such structure may be either an intermediate phase or intermetallic compound. The difference between them is not in their structures but in the change of their Gibbs energies with composition [73]. The changes of their Gibbs energies with the composition are schematically represented in Fig. 1.20. Since the change of the Gibbs energy of an intermetallic compound is very sharp, it seems reasonable to assume that its reversible potential should be a singular point. Accordingly, the dissolution peak of an intermetallic compound on the ALSV should be better defined than that of an intermediate phase [51], but this is not necessarily true since either of them should diffuse through the alloy matrix, and their diffusion could influence the shape of the ALSV peak. Hence, one can expect that the ALSV peaks of intermediate phases or intermetallic compounds which appear at the beginning of the ALSV (at the most negative potentials) could be influenced by the diffusion through the matrix of alloy (being wider), while those which are placed at the most positive potentials should be sharper.

In studying the phase composition of alloys containing intermediate phases and/or intermetallic compounds by the ALSV technique several systems were investigated. The best examples of the power of the ALSV technique are found in the work described below for the systems: Cd–Cu [51, 57, 58, 61], Cd–Ni [23], Ag–In [79], and Ag–Cd [80].

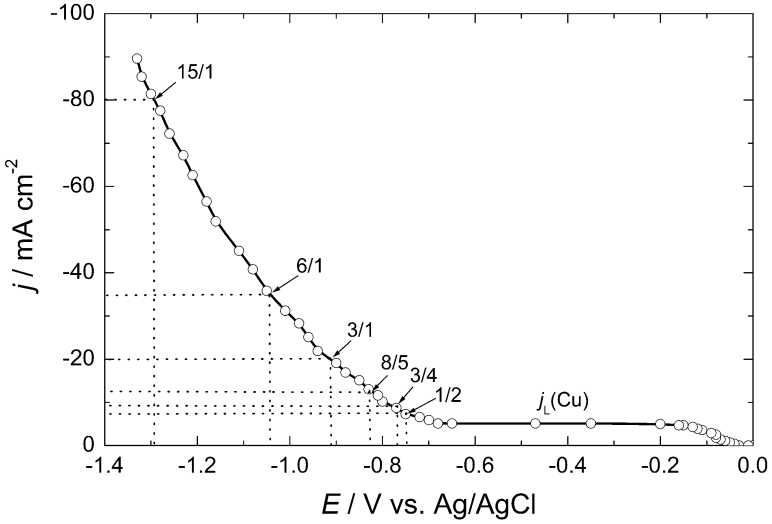

Fig. 1.21 Polarization diagrams for Cd–Cu alloy deposition at defined (marked in the figure) ratios of current densities, $j(\mathrm{Cd})/j_{\mathrm{L}}(\mathrm{Cu})$. RPM = 1,000, solution: 0.01 M $CuSO_4$ + 0.5 M $CdSO_4$ + 0.2 M Na_2SO_4 + 0.01 M H_2SO_4 (Reprinted from [1] with the permission of Springer)

System Cd–Cu [58]

According to the phase diagram of the system Cd–Cu, this alloy is characterized by the presence of four intermetallic compounds [67] (Fig. 1.22a): Cd_3Cu, Cd_8Cu_5, Cd_3Cu_4, and $CdCu_2$. In order to obtain alloys of certain compositions, corresponding to four intermetallic compounds, four samples were deposited with the current density ratios 3/1, 8/5, 3/4, and 1/2. Among these, alloys with high amount of Cd were also deposited at the current density ratios 6/1 and 15/1, as shown in Fig. 1.21. Deposition of such alloys was possible due to the fact that deposition of Cu onto RDE in the investigated solution is diffusion-controlled, taking place at the diffusion limiting current density $j_{\mathrm{L}}(\mathrm{Cu})$ (see Figs. 1.2 and 1.21).

All alloys were deposited at the gold or silver RDEs at RPM = 1,000 from the solution containing 0.01 M $CuSO_4$ + 0.5 M $CdSO_4$ + 0.2 M Na_2SO_4 + 0.01 M H_2SO_4. As can be seen in Fig. 1.21 down to about −0.7 V vs. Ag/AgCl only Cu is deposited, while at more cathodic potentials Cd deposition took place. Hence, Cu is deposited under diffusion control, while Cd is deposited under activation control and in all cases flat deposits were obtained.

Deposited alloys were dissolved by the ALSV technique (RPM = 0, $v = 1$ mV s^{-1}) in the solution 0.01 M $CdSO_4$ + 0.2 M Na_2SO_4 + 0.01 M H_2SO_4. Cadmium wire immersed in the solution of Cd^{2+} ions was used as the reference electrode (Cd^{2+}/Cd) and dissolution of alloy started from the reversible potential of this electrode [case (1) of Sect. 1.3.2.1].

In Fig. 1.22 are shown phase diagram of the Cd–Cu system [67] (a) and the ALSV of dissolution of alloy containing 75 at.% Cd and 25 at.% Cu (solid line),

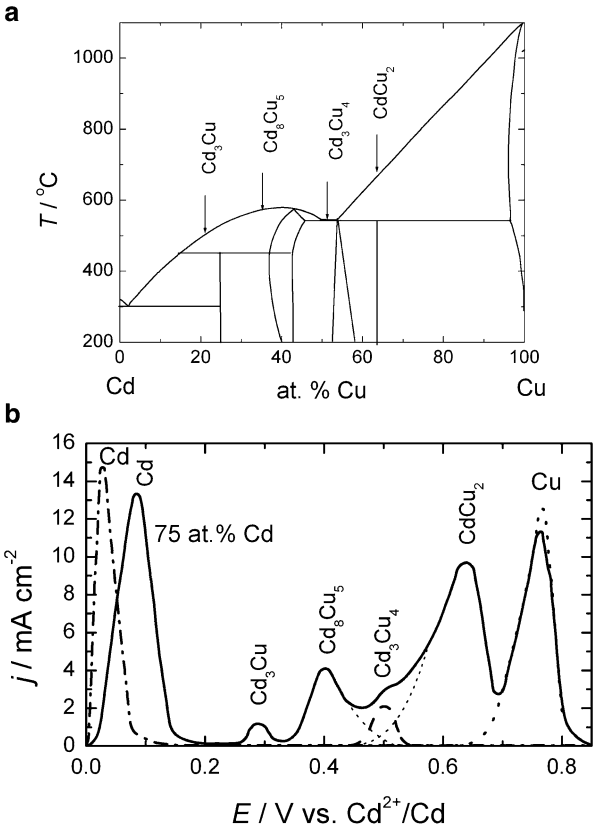

Fig. 1.22 (**a**) Phase diagram of the system Cd–Cu and (**b**) ALSV for dissolution of alloy containing 75 at.% Cd and 25 at.% Cu (*solid line*), pure Cd (*dash-dot line*), and pure Cu (*dotted line*). Solution: 0.01 M $CdSO_4$ + 0.2 M Na_2SO_4 + 0.01 M H_2SO_4; RPM = 0; $v = 1$ mV s^{-1} (Reprinted from [1] with the permission of Springer)

pure Cd (dash-dot line), and pure Cu (dotted line) (b). The peaks of dissolution of certain intermetallic compounds, as well as pure metals, are marked in the figure. As can be seen all intermetallic compounds could be detected in the deposit obtained at the current density ratio $j_{dep}(Cd)/j_{dep}(Cu) = 3/1$ (solid line). The peaks of dissolution of all intermetallic compounds are well defined, except the peak of Cd_3Cu_4 which is covered by the peak of $CdCu_2$ to a large extent. By simple deconvolution (dotted lines) of the ALSV at this position, the peak of Cd_3Cu_4 could be clearly detected (dashed line).

The shapes of ALSV's depend on the alloy composition, i.e., on the current density ratio for their deposition. In Fig. 1.23 are shown ALSV's of dissolution of Cd–Cu alloys deposited at different values of $j_{dep}(Cd)/j_{dep}(Cu)$ to a constant charge of 5 C cm^{-2}. With the increase of Cd content in the alloy the number of peaks increases. For the alloy deposited at the current density ratio 1/2 only two peaks

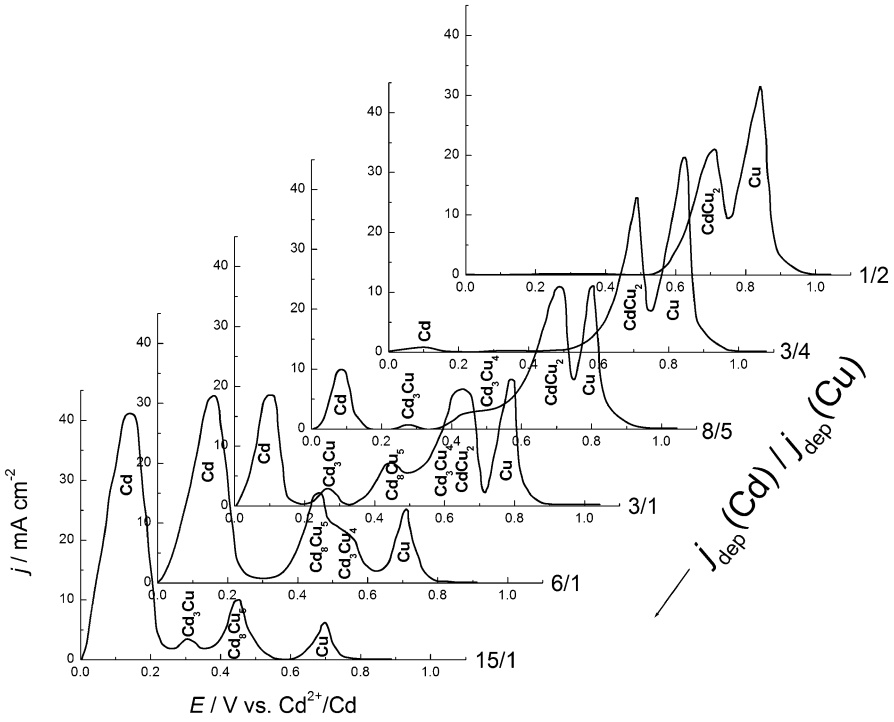

Fig. 1.23 The ALSV's for dissolution of Cd–Cu alloys deposited at different current density ratios (marked in the figure, 1/2, 3/4, 8/5, 3/1, 6/1, and 15/1). Solution: 0.01 M $CdSO_4$ + 0.2 M Na_2SO_4 + 0.01 M H_2SO_4; RPM = 0; $\nu = 1$ mV s^{-1} (Reprinted from [1] with the permission of Springer)

appear on the ALSV corresponding to $CdCu_2$ and Cu, whereas for alloys deposited at higher values of current density ratio the number of peaks increases with the peaks corresponding to other intermetallic compounds (marked in the figure).

Considering presented ALSV's it appears that Cd_3Cu_4 and $CdCu_2$ cannot be detected separately [57, 58] in any of deposited alloys and that only for the ALSV of alloy deposited at $j_{dep}(Cd)/j_{dep}(Cu) = 3/1$ the Cd_3Cu_4 could be detected after ALSV deconvolution.

It is obvious from the presented results that in spite of the adjustment of the current density ratio for the formation of particular intermetallic compound, in most cases more than one compound has been detected, indicating that single-phase equilibrium alloys could rarely be obtained, which is the fact well known in electrochemical practice [7, 8].

In order to confirm results obtained by the ALSV technique, an attempt was made to detect intermetallic compounds in alloy layers of higher thickness (>20 μm) deposited at different current density ratios, using X-ray technique. Unfortunately, the X-ray results revealed practically amorphous deposits, indicating that the grain sizes of intermetallic compounds were less than that required for

Table 1.3 Comparison of the results of the Guinier method of phase structure analysis for Cd–Cu alloys deposited at different current density ratios and submitted to subsequent thermal treatment and the results of the ALSV analysis of as-deposited samples

$j_{dep}(Cd)/j_{dep}(Cu)$	Guinier analysis results	ALSV analysis results
3/4	$CdCu_2$ Cd_3Cu_4 Cu	Cu $CdCu_2$
8/5	$CdCu_2$ Cd_3Cu_4 Cd_8Cu_5	Cu $CdCu_2$ Cd_3Cu_4 Cd_3Cu Cd
3/1	Cd_8Cu_5 Cd_3Cu Cd	Cu $CdCu_2$ Cd_3Cu_4 Cd_3Cu Cd
6/1	Cd_8Cu_5	Cu Cd_3Cu_4 Cd_8Cu_5 Cd
15/1	Cd_8Cu_5 Cd_3Cu Cd	Cu Cd_8Cu_5 Cd_3Cu Cd

Reprinted from [1] with the permission of Springer

discernible X-ray peaks. Hence, to increase the grain size of intermetallic compounds thicker samples (50 μm) were deposited onto glassy carbon disc, peeled off from the substrate surface, and submitted to thermal treatment at a temperature of 200 °C for 50 h in vacuum. The results obtained using Guinier analysis after the thermal treatment [58] are presented in Table 1.3. In spite of the fact that the X-ray analysis was performed on samples thermally treated after deposition (some solid-state reaction might take place), comparison of the ALSV results with those of the Guinier phase structure analysis shows relatively good agreement between them. The tendency for reduction in the number of intermetallic compounds for thermally treated samples could be explained in terms of the tendency towards the equilibrium [58].

From the presented results it could be inferred that deposited alloys are not in an equilibrium state. Considering ALSV's presented in Figs. 1.22b and 1.23, the question arises as to whether the ALSV peaks represent phases (intermetallic compounds) that are present in the alloy from the start or reflect the transformation of initially present phases into compounds ever richer in Cu during the process of dissolution [50]? If this would be the case (only Cd_3Cu existed at the start and is subsequently transformed successively into compounds richer in Cu), the charges under the subsequent peaks should follow a rational sequence defined by the stoichiometry. Thus, by calculation, the charges under subsequent peaks should be equal to 0.607, 0.178, and 0.357 of that under the first (most negative) peak, respectively. This is obviously not so. Indeed, the more likely event would be the

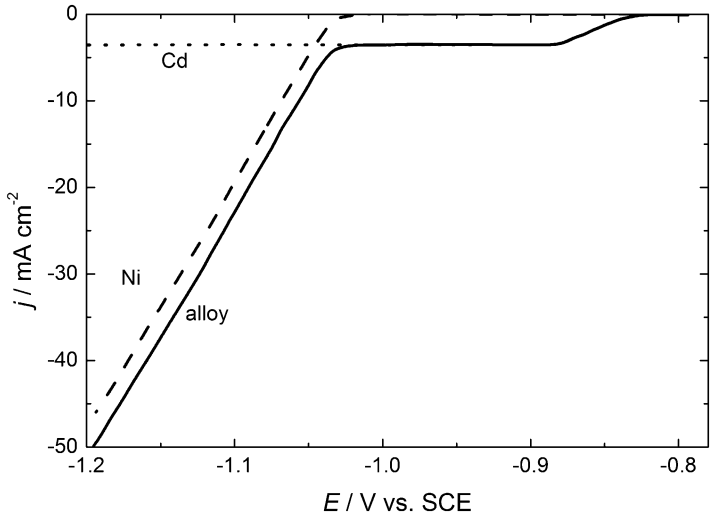

Fig. 1.24 Polarization diagrams for Cd (*dotted line*), Ni (*dashed line*), and Cd–Ni alloy (*solid line*) deposition recorded onto gold RDE at the sweep rate of 1 mV s^{-1} and RPM = 1,000 in the solution containing 0.002 M $CdSO_4$ + 0.2 M $Na_3C_6H_5O_7$ + 2.0 M $NiSO_4$ (Reprinted from [15] with the permission of Elsevier)

formation of different compounds in accordance with the standard Gibbs energy per atom sequence, but this is not the case either. Hence, it can be concluded [58] that all the compounds were formed simultaneously. This conclusion is in accordance with the results of the Guinier phase structure analysis.

System Cd–Ni [15]

System Cd–Ni is one of the most suitable binary alloy systems for the application of ALSV technique since the process of deposition/dissolution of Ni is irreversible. Although its standard potential is −0.474 V vs. SCE ($E^{\Theta}_{Cd} = -0.647$ V vs. SCE) and in this system Ni represents the more noble component, its deposition, due to high overpotential for Ni deposition [15, 24], commences at about −1.04 V vs. SCE in the solution for alloy deposition (0.002 M $CdSO_4$ + 0.2 M $Na_3C_6H_5O_7$ + 2.0 M $NiSO_4$, Fig. 1.24), while the ALSV peak for Ni dissolution in 1 M NaCl (pH 2) is positioned at about −0.10 V vs. SCE (Fig. 1.25). Accordingly, the Ni^{2+} ions formed during the dissolution of certain intermediate phase in the potential range from −0.80 V vs. SCE to −0.20 V vs. SCE (Fig. 1.25) cannot reprecipitate on the spot [case (2) of Sect. 1.3.2.1], and the ALSV peak of dissolution of pure Ni could be seen at the most positive potentials on the ALSV only if the whole amount of deposited Ni has not been dissolved during the dissolution of all phases and the deposit contains some amount of free Ni. On the other side, due to its reversible deposition/dissolution Cd starts to deposit at more positive potential than Ni of

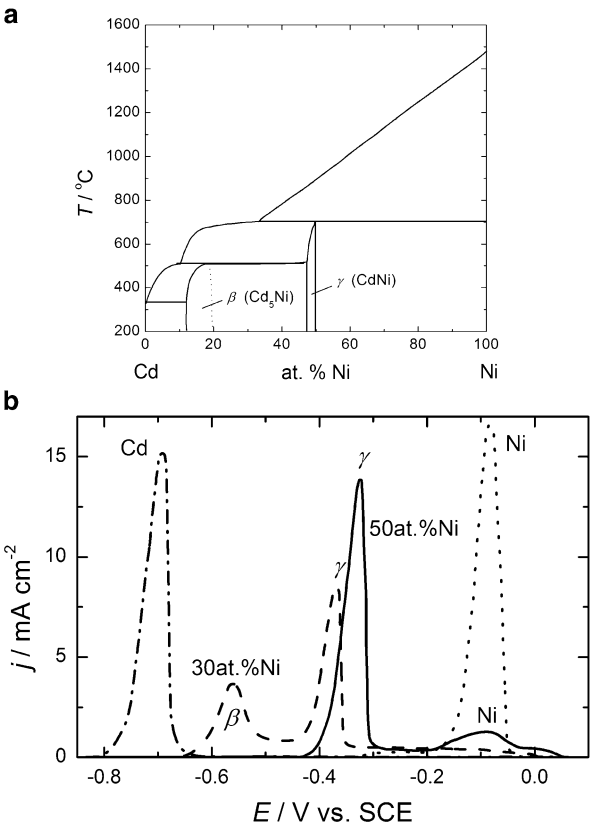

Fig. 1.25 (**a**) Phase diagram of the system Cd–Ni and (**b**) ALSV's for dissolution of pure Cd (*dash-dot line*), pure Ni (*dotted line*), alloy containing 30 at.% Ni (*dashed line*), and alloy containing 50 at.% Ni (*solid line*). Conditions of dissolution: 1 M NaCl, pH 2; RPM = 0; $v = 1$ mV s^{-1} (Reprinted from [15] with the permission of Elsevier)

about −0.82 V vs. SCE (Fig. 1.24), and its dissolution commences at about −0.80 V vs. SCE (Fig. 1.25). At the same time it is very easy to calculate alloy composition by the analysis of charge consumed during the alloy deposition, the total charge for alloy dissolution (charge under the ALSV), and the charge for deposition of Cd [see Eq. (1.38)]. The current efficiency for alloy deposition is given by the relation.

$$\eta_j = \frac{Q_{\text{diss}}(\text{alloy})}{Q_{\text{dep}}(\text{alloy})}. \tag{1.46}$$

In Fig. 1.24 are presented polarization curves for Cd, Ni, and Cd–Ni alloy deposition recorded at the sweep rate of 1 mV s^{-1} and RPM = 1,000 in the solution containing 0.002 M $CdSO_4$ + 0.2 M $Na_3C_6H_5O_7$ + 2.0 M $NiSO_4$.

The phase diagram of the system Cd–Ni [67] is presented in Fig. 1.25a. As can be seen two intermediate phases, β (Cd_5Ni) and γ(CdNi), exist in a narrow range of composition. Hence, one would expect two peaks for these phases on the ALSV of Cd–Ni alloy dissolution, placed at potentials more positive than that for pure Cd dissolution (in the case that the whole amount of Ni is not consumed in these two

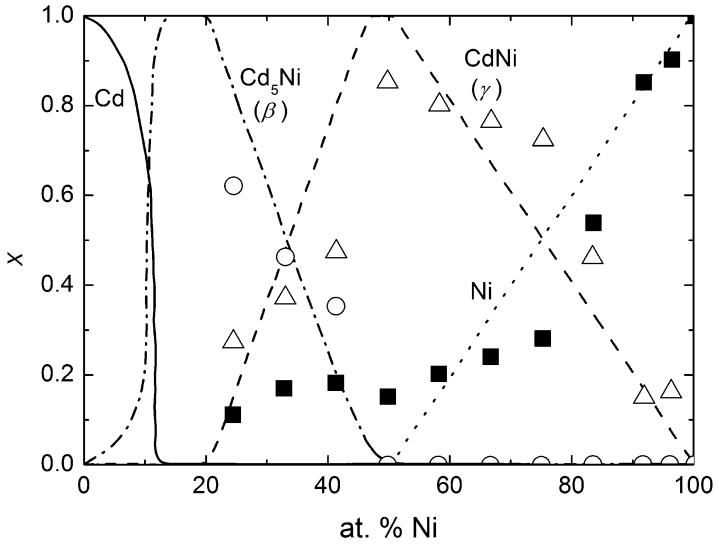

Fig. 1.26 Equilibrium molar fractions of Cd (*solid line*), β phase–Cd_5Ni (*dash-dot line*), γ phase–CdNi (*dashed line*), and Ni (*dotted line*). Molar fractions of β phase–Cd_5Ni (*open circle*), γ phase–CdNi (*open triangle*), and Ni (*filled square*) obtained by the analysis of the ALSV's (Reprinted from [15] with the permission of Elsevier)

phases, being dissolved under these peaks, additional peak for Ni dissolution might appear at the most positive potentials). Considering the ALSV's for dissolution of pure Cd (dash-dot line), pure Ni (dotted line), Cd–Ni alloy containing 30 at.% Ni (dashed line), and Cd–Ni alloy containing 50 at.% Ni (solid line), presented in Fig. 1.25b it is obvious that expected ALSV response has been obtained [15]. The Cd–Ni alloy containing 30 at.% Ni is characterized by the presence of both intermediate phases (β and γ) and no free Ni, while the alloy containing 50 at.% Ni is characterized by the presence of only one phase (γ) and small amount of free Ni.

In order to confirm agreement between the results obtained by the ALSV analysis and those obtained by the analysis of the phase diagram [67] (equilibrium ones) of the system Cd–Ni, the equilibrium molar fraction of each phase in the system (Cd, Ni, β, and γ) has been compared with that obtained by the integration of corresponding ALSV peaks. For this to be done the Cd–Ni alloys with following compositions were deposited and dissolved using ALSV technique: 24, 32, 41, 50, 58, 67, 75, 83, 92, and 97 at.% Ni. The results of this analysis are presented in Fig. 1.26. As can be seen good agreement between the equilibrium molar fractions and molar fractions obtained by the analysis of the ALSV's has been obtained for phases β and γ, while slightly higher amount of Ni (in comparison with the equilibrium one) has been obtained for alloys containing up to 50 at.% Ni. Hence, although it is well known in electrochemical practice that equilibrium alloys could rarely be obtained by electrodeposition, in some cases (as is Cd–Ni alloy) this is possible.

Taking into account that the alloys were dissolved in the electrolyte (1 M NaCl, pH 2) containing no ions of corresponding metals (Cd^{2+} and Ni^{2+}), instead of using standard potentials of metals [Eq. (1.18)] for determining the standard Gibbs energies of intermediate phases β and γ, the reversible potentials (E_r) for dissolution of Cd, Ni, β, and γ could be used. These potentials could be relatively precisely determined from the ALSV's of their dissolution as the potentials at which the dissolution current density starts to rise on the ALSV. In such a way Eq. (1.18) could be written as [15]

$$E\left(A_xB_{(1-x)}\right) = \frac{xp}{[xp+(1-x)q]}E_r(A) + \frac{(1-x)q}{[xp+(1-x)q]}E_r(B) - \frac{\mu^{\Theta}\left(A_xB_{(1-x)}\right)}{[xp+(1-x)q]F}. \tag{1.47}$$

Applying this equation on the intermediate phases β (Cd_5Ni) and γ (CdNi), following relations are obtained:

$$E_r(\beta) = 0.167E_r(Ni) + 0.833E_r(Cd) - \frac{\mu^{\Theta}(\beta)}{2F}, \tag{1.48}$$

$$E_r(\gamma) = 0.5E_r(Ni) + 0.5E_r(Cd) - \frac{\mu^{\Theta}(\gamma)}{2F}. \tag{1.49}$$

From Eqs. (1.48) and (1.49) it follows

$$\mu^{\Theta}(\beta) = 2F[0.167E_r(Ni) + 0.833E_r(Cd) - E_r(\beta)], \tag{1.50}$$

$$\mu^{\Theta}(\gamma) = 2F[0.5E_r(Ni) + 0.5E_r(Cd) - E_r(\gamma)]. \tag{1.51}$$

Using Eqs. (1.50) and (1.51) and values for E_r(Ni), E_r(Cd), $E_r(\beta)$, and $E_r(\gamma)$, the values for the standard Gibbs energies of intermediate phases were obtained as $\mu^{\Theta}(\beta) = -1.3$ kJ mol^{-1} and $\mu^{\Theta}(\gamma) = -28.9$ kJ mol^{-1}.

Hence, taking into account that the obtained values for $\mu^{\Theta}(\beta)$ and $\mu^{\Theta}(\gamma)$ are negative, this is in good accordance with the fact that already at 20 at.% of Ni there is practically no free Cd in the deposited alloys. Such a behavior indicates very strong interaction between Cd and Ni in order to form both phases, with the γ phase being present in the alloy at all alloy compositions, i.e., with the γ phase being the most stable one in the alloy.

System Ag–In [79]

The phase composition of the Ag–In alloy has been investigated by different authors [67, 81, 82], and the most cited paper is that of Campbell et al. [82]. Due to its complex structure the phase diagram is commonly presented in two parts: up

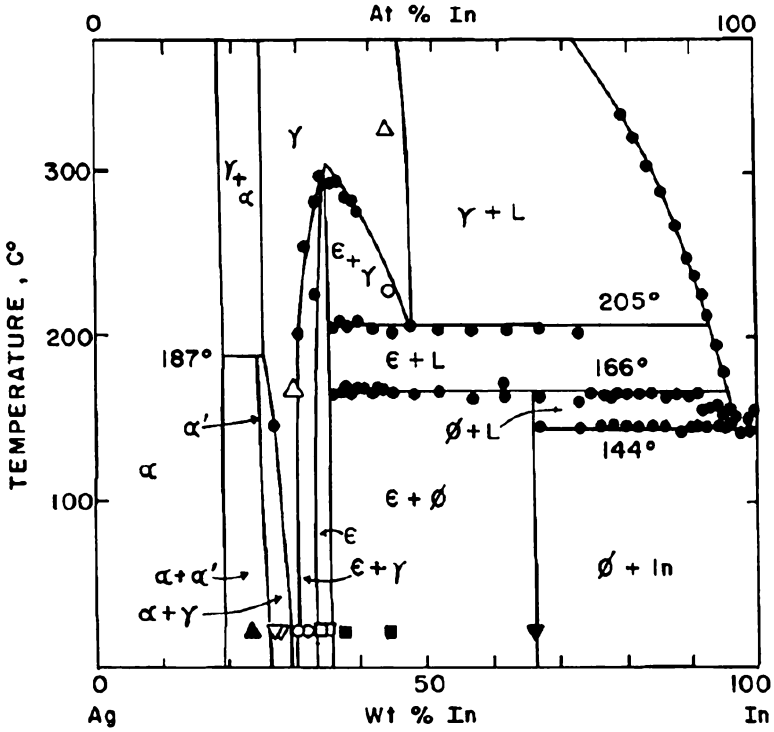

Fig. 1.27 Phase diagram of Ag–In system below 400 °C. γ (Ag_3In)—hexagonal phase; ε (Ag_9In_4)—cubic phase; ϕ ($AgIn_2$)—tetragonal phase (Reprinted from [79] with the permission of Elsevier)

to 400 °C and above. A part of the phase diagram below 400 °C is presented in Fig. 1.27. This system is characterized by the presence of three intermediate phases, ϕ ($AgIn_2$), ε (Ag_9In_4), and γ (Ag_3In), while considering deposition/dissolution characteristics of the more noble metal it belongs to the case (2) of Sect. 1.3.2.1.

The Ag–In alloy coatings were deposited onto stationary Pt electrode from cyanide electrolyte [79] with the composition: 0.2 M $InCl_3$ + 0.04 M KAg $(CN)_2$ + 0.1 M D(+) Glucose + 1 M KCN, pH 8.4. Cyclic voltammogram for alloy deposition/dissolution ($v = 1$ mV s^{-1}) is presented in Fig. 1.28, while in the inset is shown cathodic part only, with the current densities for alloy deposition marked with the arrows (four different alloy compositions). Three potential regions could be detected on the cathodic part presented in the inset: only Ag is deposited down to the inflection point A, while the alloy deposition takes place at more negative potentials (from point A to the second inflection point B) and from point B simultaneous alloy deposition and hydrogen evolution take place. Already at the current density of -2 mA cm^{-2}, Ag–In alloy coating with small amount of In is deposited, while higher amounts of In are obtained at higher cathodic current densities (-4, -6, and -8 mA cm^{-2}).

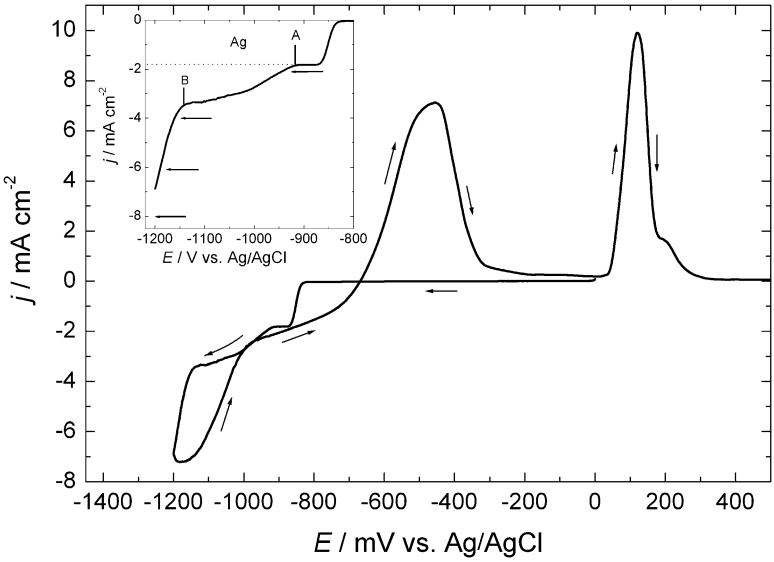

Fig. 1.28 Cyclic voltammogram for alloy deposition/dissolution ($v = 1$ mV s^{-1}) recorded onto Pt stationary electrode in the solution 0.2 M $InCl_3$ + 0.04 M $KAg(CN)_2$ + 0.1 M D(+) Glucose + 1 M KCN, pH 8.4. In the inset is shown cathodic part only, with the current densities for alloy deposition marked with the *arrows*

The ALSV curves of the dissolution of Ag–In coatings deposited from cyanide electrolyte at different current densities (−2, −4, −6, and −8 mA cm^{-2}) to a constant charge ($Q = 1.25$ C cm^{-2}) recorded in the solution of 12 M LiCl + 0.1 M HCl ($v = 1$ mV s^{-1}) are presented in Fig. 1.29. The ALSV curve of the alloy coating deposited at a current density of −2 mA cm^{-2} shows only the presence of one peak E, probably due to the α-phase of the alloy which is a solid solution of In in Ag that exists up to about 19 wt.% of In in the alloy (average amount of In in this coating is found to be about 4 wt.% [83, 84]) and/or pure Ag (see Fig. 1.27), since this peak is situated at the same potential as the peak of pure Ag dissolution. As shown earlier [85] the solid solution appears at the same potential as pure metal (in this case Ag) and cannot be detected as a separate peak. The ALSV curve of the alloy coating deposited at a current density of −4 mA cm^{-2} is characterized by the presence of three additional peaks, A, B, and D. These peaks become more pronounced in the coating deposited at a current density of −6 mA cm^{-2}, while new peak C appears in the coating deposited at a current density of −8 mA cm^{-2}. Hence, these peaks should be attributed to the presence of different phases in the alloy coatings: A—In, B—$AgIn_2$, C—Ag_9In_4, D—Ag_3In, and E—Ag. With the increase of the amount of Ag richer phases, the coating becomes very heterogeneous and some periodic spatiotemporal structures can be observed on its surface [79, 83, 84].

It is interesting to note that the effect of aging of the alloy coatings has clearly been demonstrated for this alloy. In Fig. 1.30 are shown ALSV's (a) and diffractograms (b) for freshly deposited alloy samples (dotted lines) and samples

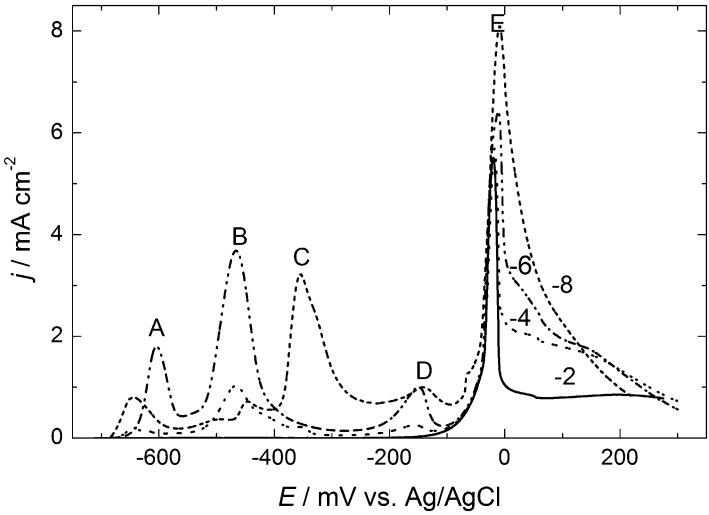

Fig. 1.29 ALSV's of Ag–In alloy coatings dissolution ($v = 1$ mV s^{-1}, solution 12 M LiCl + 0.1 M HCl) deposited at different current densities (marked in the figure in mA cm^{-2}). The ALSV peaks A, B, C, D, and E correspond to In, $AgIn_2$, Ag_9In_4, Ag_3In, and Ag, respectively (Reprinted from [79] with the permission of Elsevier)

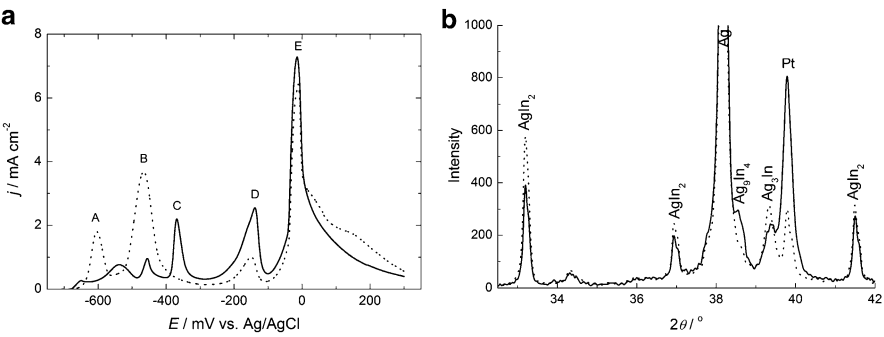

Fig. 1.30 (**a**) ALSV's of Ag–In alloy coating dissolution ($v = 1$ mV s^{-1}, solution 12 M LiCl + 0.1 M HCl) deposited at $j = -6$ mA cm^{-2} recorded immediately after deposition (*dotted line*) and after aging for 20 h at the room temperature. (**b**) Diffractograms of Ag–In alloy coating deposited at $j = -6$ mA cm^{-2} recorded immediately after deposition (*dotted line*) and after aging for 20 h at the room temperature (Reprinted from [79] with the permission of Elsevier)

kept under vacuum in a desiccator during 20 h at the room temperature (solid lines). As can be seen in these figures in a sample analyzed immediately after deposition one phase, Ag_9In_4—peak C, is missing. It is reasonable to expect that during the solid-state reaction, which takes place at the room temperature very slowly, more noble phases (Ag_9In_4 and Ag_3In) are formed on the account of the less noble ones (In and $AgIn_2$), as shown in Fig. 1.30. The same effect has also been detected for the system Cd–Cu [86].

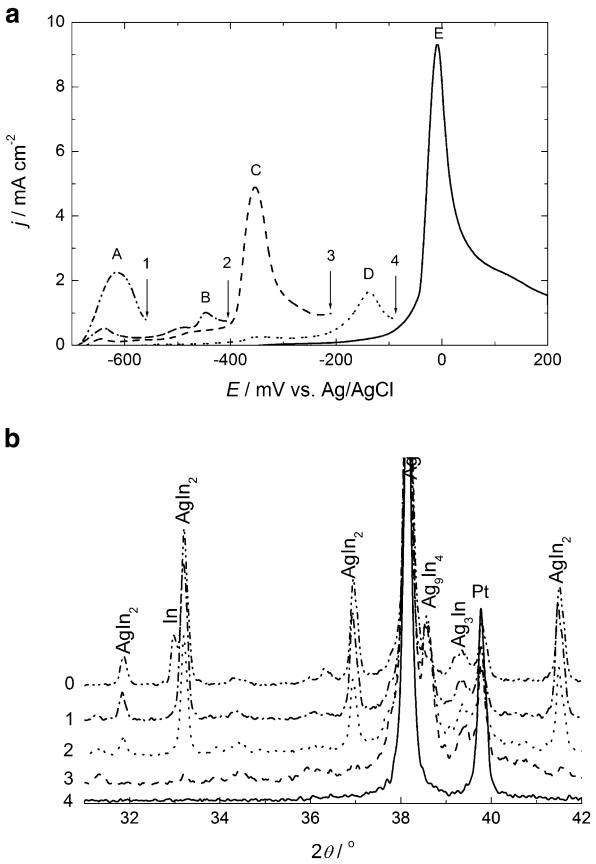

Fig. 1.31 (a) ALSV's of Ag–In alloy coating dissolution ($v = 1$ mV s^{-1}, solution 12 M LiCl + 0.1 M HCl) deposited at $j = -8$ mA cm^{-2}: *1* first dissolution sequence; *2* second dissolution sequence; *3* third dissolution sequence; *4* fourth dissolution sequence. (**b**) Diffractograms of the same Ag–In alloy coating: *0* before the first dissolution sequence; *1* after the first dissolution sequence; *2* after the second dissolution sequence; *3* after the third dissolution sequence; *4* after the fourth dissolution sequence (Reprinted from [79] with the permission of Elsevier)

In order to confirm the statement about the presence of phases mentioned above, following experiment was performed: an alloy coating containing all phases was submitted to the ALSV experiment in such a way that during the first sweep only the phase under the first peak (A) was dissolved; in the second sweep, starting from the same potential (−800 mV), the first (A) and second (B) peaks were dissolved; in the third sweep A–C peaks were dissolved; in the fourth sweep A–D peaks were dissolved; and finally during the last sweep the rest of the alloy was dissolved. The result of this experiment is shown in Fig. 1.31a. After the dissolution of the peak A (up to the potential limit 1, marked with the arrow), during the second run (up to the potential limit 2) very small peak A appears on the ALSV curve, while peak B is

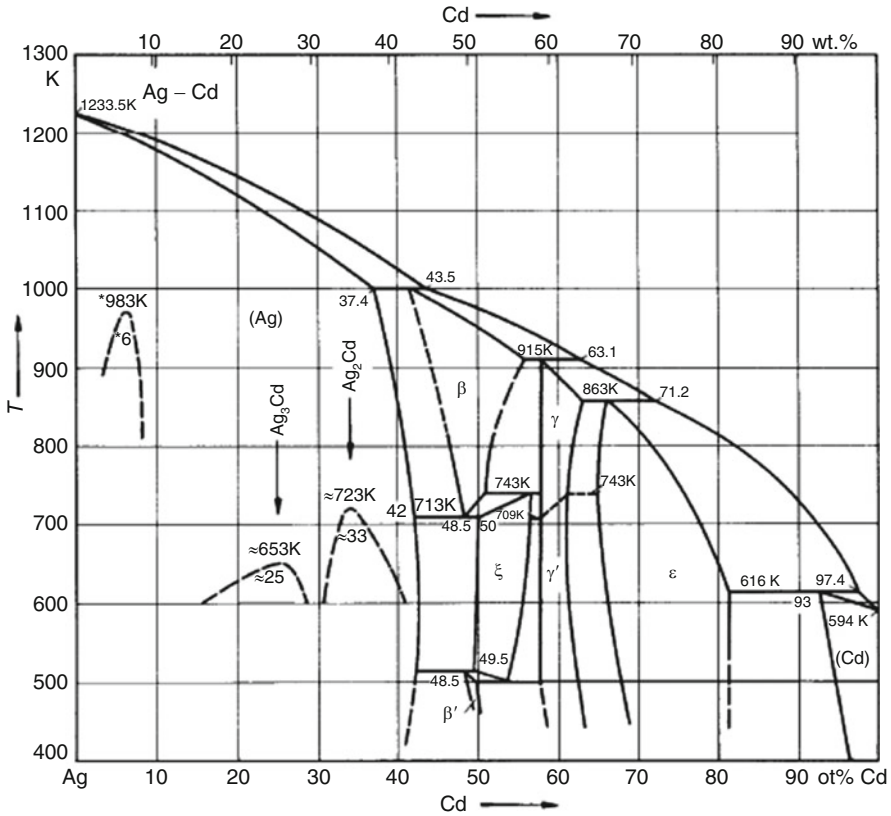

Fig. 1.32 Phase diagram of Ag–Cd system

almost the same as one recorded on the ALSV curve shown in Fig. 1.29. During the next run these two peaks are still slightly visible, while the peak C is well defined (as in Fig. 1.29). After dissolving a phase corresponding to the peak C, during the next run, peaks A and B disappear, peak C become very small, while peak D is the same as in Fig. 1.29. Finally, during the last run no peaks, except the peak E, are seen on the ALSV. After each ALSV run samples were investigated by means of X-ray diffraction, and corresponding diffractograms are shown in Fig. 1.31b. As can be seen excellent agreement between ALSV and X-ray diffraction results were obtained, confirming above statement concerning the presence of different phases.

System Ag–Cd [80]

Phase diagram of the Ag–Cd system is presented in Fig. 1.32. The phases observed in the Ag–Cd alloy system are described in the monograph of Hansen and Anderko [67] in the following way: The solubility of Cd in Ag (α-phase) reaches 42 at.%.

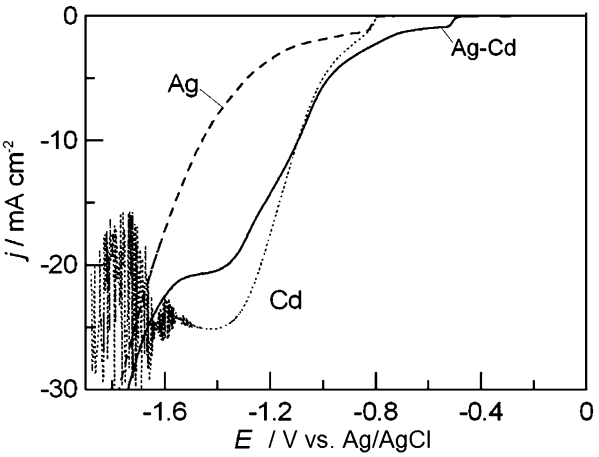

Fig. 1.33 Polarization curves recorded at a sweep rate of 1 mV s^{-1} in the electrolyte containing 0.032 M KAg$(CN)_2$ + 0.56 M KCN (Ag), 0.14 M $CdSO_4 \cdot 8/3H_2O$ + 0.56 M KCN (Cd), and 0.032 M KAg$(CN)_2$ + 0.14 M $CdSO_4 \cdot 8/3H_2O$ + 0.56 M KCN (Ag–Cd) (Reprinted from [80] with the permission of Elsevier)

In the composition range between 26 and 29 at.% Cd, the high-temperature Ag_3Cd phase could be observed. In the composition range between 42 and 60 at.% Cd, three phases (β, β' and ξ) are established in the vicinity of 50 at.% Cd at different temperatures. The β and β' phases are characterized by the *b.c.c.* lattices and the ξ phase by *h.c.p.* lattice. These phases correspond to the AgCd compound. The existence of several phases (γ, γ', ε, and η) is reported in the composition range between 60 and 100 at.% Cd. The first one (γ) is a hexagonal phase, and the second one (γ') possesses a *b.c.c.* lattice. They correspond to the Ag_5Cd_8 compound. The pure hexagonal ε phase exists in the range 68–81.4 at.% Cd and corresponds to the Cd_3Ag compound. In the composition range 81.4–96.9 at.% Cd, ε phase exists together with the η phase, which is a solid solution of Ag in Cd. Pure η phase is observed in the interval 96.9–100 at.% Cd (100 °C).

The Ag, Cd, and the Ag–Cd alloy coatings were deposited onto stationary Pt electrode from cyanide electrolytes [80]. Pure Cd from the solution containing 0.14 M $CdSO_4 \cdot 8/3H_2O$ + 0.56 M KCN, pure Ag from the solution containing 0.032 M $KAg(CN)_2$ + 0.56 M KCN, and Ag–Cd alloys from the solution containing 0.032 M $KAg(CN)_2$ + 0.14 M $CdSO_4 \cdot 8/3H_2O$ + 0.56 M KCN. Figure 1.33 shows polarization curves recorded at a sweep rate of 1 mV s^{-1} in the electrolyte containing both metals separately or together. The deposition of Ag (dashed line) is characterized by the cathodic shoulder, which is most likely indication of the diffusion limiting current density (taking into account small concentration of Ag) at a potential of about −0.82 V, with the deposition starting at about −0.79 V. The increase of the cathodic current density at potentials more negative than −1.2 V during the Ag deposition is the consequence of simultaneous hydrogen evolution. Pure Cd deposition (dotted line) starts at the same potential as that of Ag. At potentials more negative than −1.6 V, current oscillations with amplitude higher than 200 mV have been observed. In the case of Ag–Cd alloy deposition, a shoulder representing diffusion controlled deposition of Ag (solid line) appears at about −0.51 V (for about 0.3 V more positive than the shoulder of pure Ag). Hence, in the solution containing both metal ions, deposition of

Table 1.4 Concentration of different Ag complexes and their equilibrium potentials

	Concentration (%)			E_{eq}/V vs. Ag/AgCl	
Solution composition	$[Ag(CN)_2]^-$	$[Ag(CN)_3]^{2-}$	$[Ag(CN)_4]^{3-}$	$[Ag(CN)_3]^{2-}$	$[Ag(CN)_2]^-$
0.032 M $KAg(CN)_2$ + 0.56 M KCN	35.9	61.2	2.6	−0.737	
0.032 M $KAg(CN)_2$ + 0.14 M $CdSO_4$ + 0.56 M KCN	98.1	1.9	–		−0.479

Reprinted from [80] with the permission of Elsevier

Ag commences at more positive potential. In order to find out the reason for such behavior, the analysis of Ag complexes with cyanide has been performed. The results are presented in Table 1.4. As can be seen, when pure Ag is present in the KCN solution the dominant complex is $[Ag(CN)_3]^{2-}$, with the equilibrium potential of −0.737 V. In the presence of Cd ions most of the CN^- anions are consumed in Cd–CN complexes ($[Cd(CN)]^+$, $[Cd(CN)_2]$, $[Cd(CN)_3]^-$, and $[Cd(CN)_4]^{2-}$), and the dominant Ag–CN complex becomes $[Ag(CN)_2]^-$, with the equilibrium potential of −0.479 V. Hence, from the presented analysis it is obvious that the first shoulder on a solid curve in Fig. 1.33 for Ag–Cd alloy deposition corresponds to the deposition of pure Ag from $[Ag(CN)_2]^-$ complex [87].

Five alloy samples were deposited to the total charge of 1.3 C cm^{-2} at different potentials (−1.0, −1.4, −1.6, −1.8, and −2.0 V). Their ALSV's and diffractograms are presented in Fig. 1.34a, b, respectively. As in a previous case the results of the ALSV analysis and the X-ray analysis are in good agreement. Accordingly, the ALSV peaks detected in Fig. 1.34a could be ascribed to following intermediate phases: the peak A corresponds to the pure Cd phase; the peak B to the $AgCd_3$ phase; the peak C to the AgCd phase; the peak D to the Ag_3Cd phase; and the peak E to the pure Ag.

It is interesting to note that neither ALSV nor X-ray analysis is sensitive to the presence of different lattices for certain compounds at room temperature analysis: (β, β', and ξ)—AgCd compound; (γ, γ', ε, and η)—Ag_5Cd_8 compound.

There are two more systems with intermediate phases investigated by the ALSV technique application, Ni–Zn [87–90] and Co–Zn [91]. As in above presented results, ALSV and X-ray analysis showed good agreement for both systems.

1.3.4 Mechanism of Dissolution of Thin Layers of Electrodeposited Alloys

When a single-phase binary alloy is anodically dissolved in an aqueous solution, assuming that all the necessary conditions are fulfilled (cf. Sect. 1.3.2.1), the mechanism of dissolution may be [1, 40]:

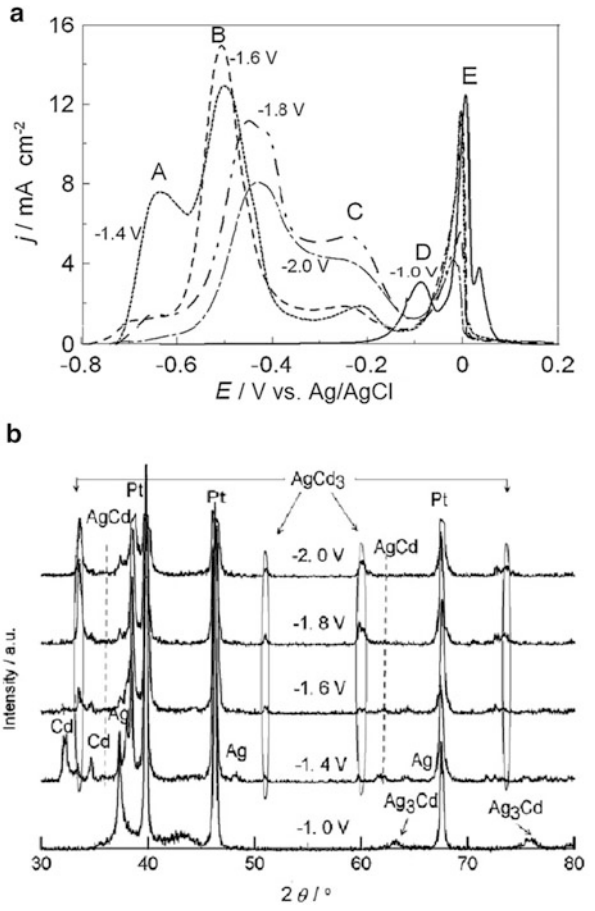

Fig. 1.34 (**a**) ALSV's of Ag–Cd alloy coatings dissolution ($v = 1$ mV s^{-1}, solution 12 M LiCl + 0.1 M HCl) deposited at different potentials (marked in the figure). (**b**) Diffractograms of corresponding alloy coatings (Reprinted from [80] with the permission of Elsevier)

1. Simultaneous dissolution of both components of the alloy, with the more noble one being reprecipitated on the spot;
2. Partial dissolution (ionization) of the less noble component, causing restructuring of the remaining matrix into a phase richer in the more noble component;
3. Complete dissolution (ionization) of the less noble component, with the atoms of the more noble one aggregating by surface diffusion (formation of patches and monolayers of the more noble component with the possibility of formation of small three-dimensional crystals, which may prevent further dissolution of the less noble component);
4. Complete dissolution (ionization) of the less noble component, leaving atoms of the more noble one in an unstable matrix. Atoms of both metals then move in the solid phase by volume diffusion, one kind dissolving, and the other kind restructuring the matrix so that it corresponds to the crystal lattice of the pure metal.

On the basis of diffusivities extrapolated from high-temperature measurements, the participation of the fourth mechanism should be negligible. However, this extrapolation assumes that the equilibrium concentration of vacancies is established and that the contribution of diffusion along small grain boundaries and dislocations is negligible. This is not the case in reality, since the diffusion coefficients at room temperature may be considerably larger than the extrapolated ones (in the case of Cu, monovacancies cannot account for this mechanism, but divacancies, with $D = 1.3 \times 10^{-12}$ cm^2 s^{-1}, may make the mechanism operative) [40].

There is a significant inconsistency in the results reported earlier from investigations of the mechanism of alloy dissolution, particularly for results obtained with bulk alloy samples [39–48]. For example, for one and the same system (Cu–Ni) it was found both that components dissolve simultaneously [44] and that Ni dissolves preferentially [43]. In the case of Cu–Au and Cu–Zn systems, two different mechanisms were observed, preferential dissolution of the less noble component and simultaneous dissolution of both components [40–43]. Actually, it was concluded that in the Cu–Zn system, enrichment of the surface with copper is a necessary condition for simultaneous dissolution of both components to start. Hence, there exists an induction period of disproportionate dissolution of the less noble component, preceding simultaneous dissolution [43].

It is likely that the mechanism depends on the composition of the alloy. Thus, at low contents of the more noble metal, the dissolution of the less noble one leaves the atoms of the former loose and ready to oxidize. Conversely, at high contents of the more noble metal, the atoms of the less noble one are likely to tend to squeeze out of the lattice without producing much change in the latter.

It is obvious that in bulk alloy samples, diffusional limitations (diffusion of metal atoms from the bulk of the alloy to the surface) influence the process of anodic dissolution. In the case of dissolution of thin layers of alloys, where the entire amount of the alloy is dissolved, such limitations (if they exist) can be overcome (cf. Sect. 1.3.2.1). However, two phenomena should be noted:

(a) Simultaneous dissolution creates locally an increased concentration of the positive constituent, corresponding to a more positive reversible potential of the pure metal phase than that attained at a particular moment in the course of the anodic sweep. Hence, that potential turns out to be cathodic with respect to the reversible potential, so that this metal constituent must deposit on the spot either in the form of another alloy phase with a more positive reversible potential or in the form of pure metal crystallites. Hence, the net recorded current reflects the dissolution of the less noble constituent only.
(b) Dissolution of one alloy phase from a mixture with other phases, or through redeposited positive constituent, must run into transport difficulties. Hence, the dissolution current comes under diffusion control, which makes the current vs. potential (time) pattern similar to that obtained in such a situation for a cathodic metal deposition process; that is, it exhibits a maximum and subsequent decay.

Considering all presented cases it appears that the alloy phase dissolves by dissolving both metal constituents. If the deposition/dissolution process of the more noble metal is reversible [case (1) of Sect. 1.3.2.1], the ions of this metal reprecipitate on the spot and the whole amount of the more noble metal becomes dissolved through the ALSV peak positioned at the most positive potential (systems Ag–Pd, Cd–Cu, Cd–Zn, Cu–Pb, etc.). If the deposition/dissolution process of the more noble metal is irreversible [case (2) of Sect. 1.3.2.1], the more noble metal dissolves together with the less noble one through the peak of each phase. In the case that the whole amount of the more noble metal is not consumed in existing phases, the rest of the more noble metal becomes dissolved through the ALSV peak positioned at the most positive potential (systems Cd–Co, Cd–Ni, Co–Ni, etc.).

Finally, it should be noted that using the ALSV technique, it is possible to identify solid-state reactions in electrodeposited alloys at room temperature, leading to the formation of more noble phases on the account of the less noble ones (as shown for the systems Ag–In [79] and Cd–Cu [85]).

1.4 Electrodeposition of Composite Metal Coatings

1.4.1 Basic Concepts

Two types of coatings obtained by electrodeposition could be ascribed to composite metal coatings: (i) laminar metal structures and (ii) metal coatings with inclusion of nonmetallic particles [1, 92].

According to the theory of composite systems [93], the existence of intermediate layer between two metals is inevitable in multilayered laminar metal structures. The thickness of the intermediate layer is usually of the order of couple of atomic layers, and the parameters of the system (concentration of individual metals, crystal structure, Young's modulus, density, coefficient of thermal expansion, etc.) change from one layer to another. Usually such intermediate layer is composed of two layers of solid solutions and one layer of intermetallic compound, as it is schematically presented in Fig. 1.35.

By using appropriate techniques for the formation of such structures (chemical of physical evaporation, electrodeposition, etc.), it is possible to achieve high value of total surface area of the intermediate layer amounting to 3,000 cm^2 cm^{-3}. Accordingly, the larger the surface of the intermediate layer, the higher the difference in the properties of the multilayered laminar metal structure (higher values of Young's modulus, hardness, tensile strength, etc.) [93]. Taking into account that the electrodeposition of such structures is the cheapest technique, its advantage over the other techniques is obvious.

It should be emphasized here that multilayered laminar metal structures could be obtained by electrodeposition of individual metal layers from separate baths, which is a time consuming process. On the other side, it is possible to obtain such deposit

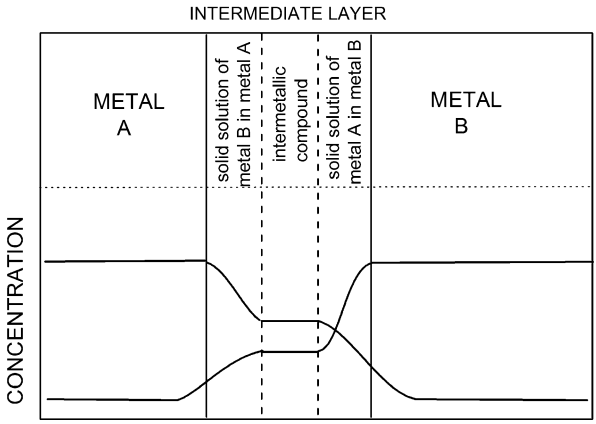

Fig. 1.35 Schematic representation of the intermediate layer in multilayered laminar metal structures

from one bath containing ions of both metals by appropriate choice of metal ions concentration and applied current density. In such a case one layer (usually first) is always pure more noble metal, while the other one (second) must be alloy of these two metals. Hence, by appropriate choice of deposition conditions, one can adjust the composition of a second layer in multilayered structures, as well as the thickness of each layer, and, accordingly, properties of such structures.

Concerning composite structures containing metals with inclusion of nonmetallic particles, despite the potential interest and many years of work in this field, only a few large-scale commercial baths have been developed, while general theoretical explanation of this phenomenon is still missing [1, 92] although some attempts were successfully applied to certain systems [1, 92].

1.4.2 Electrodeposition of Laminar Metal Structures

As already stated above, multilayered laminar metal structures could be obtained by electrodeposition of individual metal layers from separate baths or from one bath containing ions of both metals. Only the second case is of interest for this chapter, and such conditions will be discussed.

1.4.2.1 Spontaneous Formation of Layered Deposits

In the investigations of electrodeposition of alloys, laminar metal structures, parallel to the cathode surface, were observed in quite a few instances. Such phenomenon has been observed by Meyer and Phillips [94] during the deposition of Cu with other metals; Aotani [95] detected laminar metal structures in the case of Fe–Ni alloys deposition, while Mikhalev [96] found them in Cd–Zn deposits. This phenomenon has been accompanied with the fluctuations of potential ranging from

0.1 mV to 0.1 V depending on the system and applied current density. Any fluctuations of periodic nature (oscillations) must be the consequence of superposition of two counteracting processes. Accordingly, this phenomenon could be explained in a following way: At the beginning of the process under galvanostatic conditions, the rate of deposition of the more noble metal is sufficient for its nuclei to be formed and its grains to grow. However, after some time, due to depletion of the diffusion layer, the concentration of the ions of the more noble metal at the cathode surface becomes practically zero and the discharge of the ions of the less noble metal must compensate for the decrease of the partial current density of the more noble metal. This requires a certain increase in cathodic overpotential and nucleation and growth of the less noble metal mainly. After some time the concentration of the ions of the more noble metal at the cathode surface recovers to the point where its nucleation can start again, causing decrease of the cathodic overpotential and, accordingly, the nucleation and growth of the less noble metal subsides. Hence, the process starts all over again.

1.4.2.2 Formation of Laminar Deposits by Pulsating Current Regimes

Instead of letting laminar metal structures to be formed spontaneously during the alloy deposition, there was significant motivation to obtain well-defined multilayered structures of controlled compositions and thicknesses of individual layers. Deposition of such structures was first demonstrated by Brenner [4], while Cohen et al. [97] obtained an Ag–Pd alloy with periodically changing composition by alternating the current density, and such structure showed improved wear performance of electrical contacts. In order to obtain laminar metal structure with the thickness of individual layers (with the second layer being Cu–Ni alloy with small amount of Ni) of 300 nm in the system Cu–Ni, pulsating regimes were used [98, 99]. It was shown that such structures possessed higher tensile strength [98] and microhardness [99].

In the application of pulsating regimes [97–99] three types of pulses, schematically presented in Fig. 1.36, were used.

The first attempt in theoretical treatment of the variation of the composition of a deposit obtained by pulsating current from a bath containing two different metal cations, using complicated mathematical procedure, was presented in 1985 [100]. The quantitative theory of laminar metal deposition based on fundamental concepts of electrode kinetics, using much simpler mathematical approach, was presented in a series of papers of Despić and coworkers [101–103].

Single Current Pulse Regime

For the deposition of laminar metal coatings, two conditions must be fulfilled: (1) The reversible potentials for metals A and B must be sufficiently different so that at a given current density the less noble one (B) virtually does not deposit

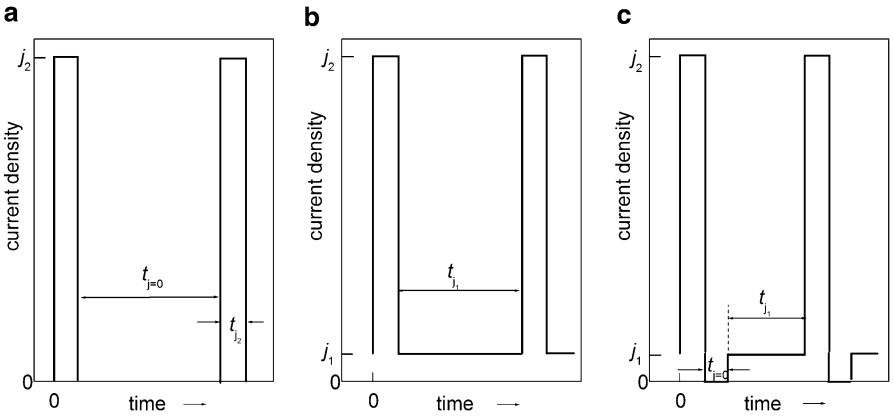

Fig. 1.36 Schematic presentation of pulsating regimes used for deposition of laminar metal structures

during the deposition of the more noble one (A) until complete concentration polarization with respect to ions of metal A takes place. (2) Within the duration of the current density pulse, Send's equation [22] for diffusional polarization is obeyed with respect to concentration change, resulting in transition from deposition of metal A to deposition of metal B after well-defined transition time.

Hence, the first layer contains pure metal A and its thickness is, according to Faraday's law, defined by

$$d(\mathrm{I}) = \left(\frac{M_\mathrm{A}}{z_\mathrm{A}\rho_\mathrm{A}F}\right) j\tau_\mathrm{A}, \tag{1.52}$$

where M_A, ρ_A, and z_A are, respectively, atomic weight, density, and charge on the ions of metal A, j is the current density in the pulse, while τ_A is the transition time with respect to the ions of metal A. Assuming that the convection and migration of ions of the electrolyte are negligible, τ_A is defined by Send's equation [22]:

$$\tau_\mathrm{A} = \frac{(z_\mathrm{A}F)^2 \pi D_\mathrm{A}}{4}\left(\frac{C_\mathrm{A}^\mathrm{o}}{j}\right)^2, \tag{1.53}$$

where $C_\mathrm{A}{}^\mathrm{o}$ and D_A are, respectively, the bulk concentration and diffusion coefficient of the ions of metal A. Introducing Eq. (1.53) into Eq. (1.52) and rearranging one obtains

$$\frac{\left(C_\mathrm{A}^\mathrm{o}\right)^2}{j} = \frac{4\rho_\mathrm{A}}{z_\mathrm{A}F\pi D_\mathrm{A}M_\mathrm{A}} d(\mathrm{I}). \tag{1.54}$$

Considering Eq. (1.54) it could be concluded that desired thickness of the layer of metal A could be achieved by proper choice of metal ions concentration and the current density of the pulse.

Taking into account that Sand's equation is valid only as long as the change of concentration occurs within a stagnant layer undisturbed by convection and introducing the Nernst's diffusion layer boundary δ and hydrodynamic layer boundary Δh, the minimum current density that must be applied for the transition and deposition of the second layer to take place is given by

$$j^{\min} = \frac{z_A F \pi D_A}{2\Delta h} C_A^o \tag{1.55}$$

and, accordingly, by introducing Eq. (1.54) into Eq. (1.55), the maximum achievable thickness of the first layer (metal A) is

$$d(\mathrm{I})^{\max} = \frac{M_A C_A^o \Delta h}{2\rho_A}. \tag{1.56}$$

Deposition of the second layer starts after τ_A is reached and is accompanied by sudden change of potential to the reversible potential of metal B deposition [1].

The shape of the potential vs. time (E vs. t) response in such a case depends on the property of the alloy and its constituents in the investigated solution. Two situations could be considered: (i) replacement reaction takes place during the off-time ($j = 0$) period; (ii) replacement reaction does not take place during the off-time ($j = 0$) period.

(i) If the difference between the reversible potentials of metals A and B is sufficient, and the constituents of the alloy do not mix in the solid state (eutectic-type alloy), and/or deposition/dissolution of metal B is reversible, replacement reaction must take place during the off time ($j = 0$). Such a case is schematically presented in Fig. 1.37. The current density change is presented in (a), while corresponding potential change is presented in (b). As can be seen, after reaching τ_A, metal A continues to deposit but at a decreasing partial current density [actually by its diffusion limiting current density—$j_d(A) = j_L(A)$], while the partial current density of the metal B increases to make a constant current density of the pulse—$j_d(B)$. If the concentration of ions of metal B is much larger than that of the metal A, the growth of the second layer could be virtually unlimited and the content of metal A in the second layer will continuously decrease with the thickness of the second layer [following the decrease of $j_d(A)$]. Corresponding potential response, schematically presented in (b), is characterized by a sudden increase of cathodic potential to the value higher than $E_r(B)$ at the position of τ_A. At the position of the end of the current pulse (T) and the beginning of the current density off period ($j = 0$), replacement reaction will take place. The deposition of metal A will continue with $j_d(A) = j_L(A) = j_d(A)_r$, while, in order to keep total current density at zero, the less noble metal B will start to dissolve with the positive partial current density $j_{diss}(B)_r$ equal to that of metal A deposition. Once this process is finished,

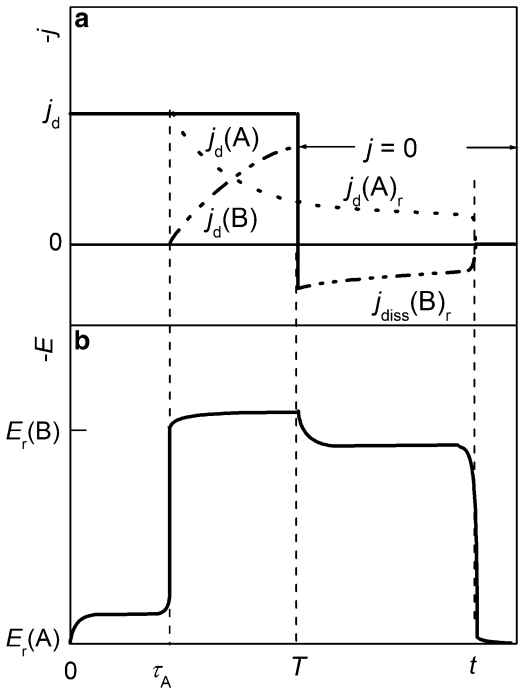

Fig. 1.37 Schematic representation of the partial current densities changes (**a**) and corresponding potential response (**b**) during the deposition of two layers of metals A and A + B by constant current density pulse (j_d) up to time T and during the replacement reaction at $j = 0$. Partial current density for deposition of metal A after reaching $\tau_A - j_d(A)$ and partial current density for deposition of metal B after reaching $\tau_A - j_d(B)$, partial current density for deposition of metal A during the replacement reaction $j_d(A)_r$, partial current density for dissolution of metal B during the replacement reaction $j_{diss}(B)_r$ (Reprinted from [1] with the permission of Springer)

either due to dissolution of the whole amount of metal B in the second layer or prevention of its dissolution for some reasons (e.g., at some places of a second layer atoms of metal B become covered with a monolayer of metal A, etc.), the current density $j_{diss}(B)_r$ will drop to zero and corresponding potential to the value of $E_r(A)$ [1].

Although the replacement reactions have extensively been studied in the literature [104], the only example for such reaction in the layered deposits was demonstrated for the system Cu–Pb [1, 101]. A two-layer structure, composed of a first layer of pure Cu and a second layer of Cu–Pb alloy, has been deposited at a constant current density $j_d = -1$ mA cm^{-2} for different times (from 60 to 300 s) on a stationary glassy carbon electrode from a solution containing 0.01 M Cu $(CH_3COO)_2$ + 0.01 M Pb$(CH_3COO)_2$ + 1 M HBF_4 [101]. After the deposition, zero current density ($j = 0$) was applied (positions marked in the figure with 1, 2, 3, 4, 5, 6, 7, 8, and 9) and corresponding potential responses are presented in Fig. 1.38. As can be seen after applying zero current density (positions 1–9), the

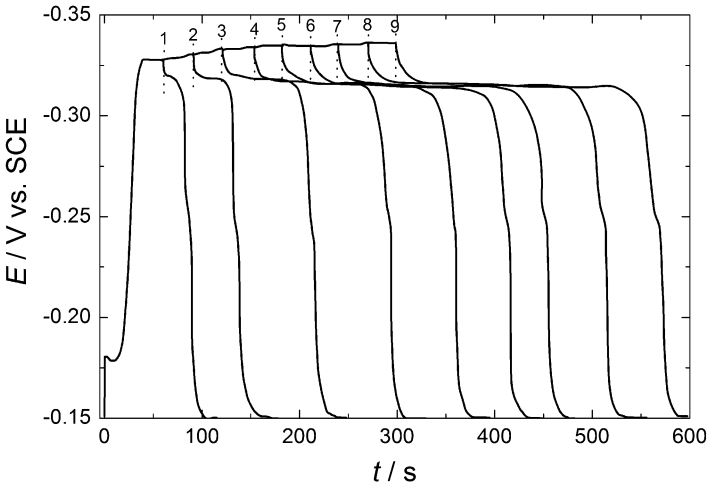

Fig. 1.38 Potential responses recorded during constant current density $j_d = -1$ mA cm^{-2} pulse trains on a stationary glassy carbon electrode from a solution containing 0.01 M $Cu(CH_3COO)_2$ + 0.01 M $Pb(CH_3COO)_2$ + 1 M HBF_4. After the deposition, zero current density ($j = 0$) was applied (positions marked in the figure with 1–9) (Reprinted from [1] with the permission of Springer)

potential remains for some time at a level slightly below the reversible potential of Pb, after which it falls to the potential of Cu. That time is virtually equal to duration of the current density pulse, indicating that the dissolution of Pb from a second layer occurs all the time. When the dissolution process is finished, potential returned to the reversible potential of Cu. By the EDS analysis it was confirmed that the whole amount of deposited Pb has been dissolved during the off-time periods. Hence, all conditions (i) for the replacement reaction to take place were fulfilled: Cu–Pb is eutectic-type alloy, and deposition/dissolution of Pb is reversible [101].

(ii) If the difference between the reversible potentials of metals A and B is sufficient, and the constituents of the alloy mix in the solid state forming solid solution and a metal B passivates in the electrolyte used, replacement reaction will not take place during the off-time ($j = 0$). Such a case is schematically presented in Fig. 1.39. The current density change is presented in (a), while corresponding potential change is presented in (b). During the current density pulse everything is the same as in a previous case. The absence of replacement reaction is characterized by sudden potential change from E_r(B) to E_r(A) at the position of the end of the current pulse (T) and the beginning of the current density off period ($j = 0$).

Typical example for such behavior is the system Cu–Ni [98, 99, 103, 105, 106]. This system belongs to the solid solution type alloys, and the dissolution of Ni is prevented by its passivation in the electrolyte for deposition. As shown earlier [15, 24] dissolution of the whole deposited amount of Ni could be achieved in chloride containing electrolyte of pH 2.

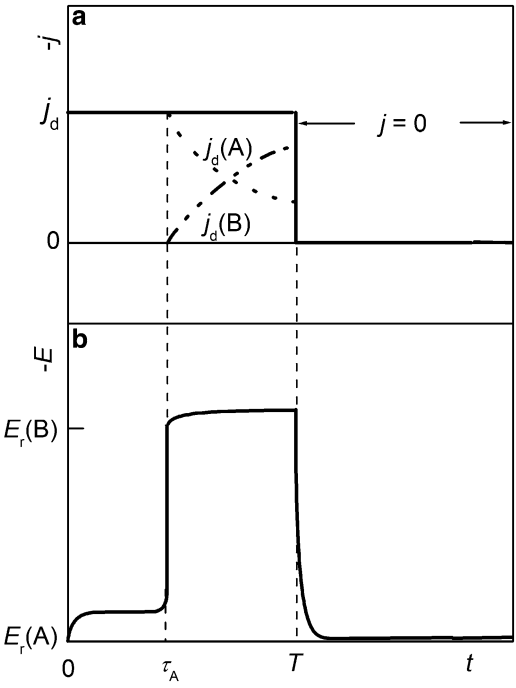

Fig. 1.39 Schematic representation of the partial current densities changes (**a**) and corresponding potential response (**b**) during the deposition of two layers of metals A and A + B by constant current density pulse (j_d) up to time T and after, in the absence of the replacement reaction at $j = 0$. Partial current density for deposition of metal A after reaching $\tau_A - j_d(A)$, partial current density for deposition of metal B after reaching $\tau_A - j_d(B)$

Dual Current Pulse Regime

Single current pulse regime imposes serious limitations on both the thickness of the layers of the more noble metal and the content of that metal in the second layer. The application of a dual current pulse scheme was found more suitable for manipulation of the thickness of each layer, as well as the content of the more noble metal in the second layer. The scheme consists of current pulses in two different intensities each. A lower current density j(I) for a certain time period T(I) is followed by a higher current density j(II) for a period T(II) before the current is interrupted (or the sequence repeated). It can be shown that with such a scheme and proper choice of parameters, any desired thickness of both layers can be achieved and the content of metal A in the second layer can be reduced to a desired level. The process can be improved, in terms of shortening the deposition time of the first layer while maintaining a desired content of metal A in the second layer and by synchronously modulating the hydrodynamic conditions. Such a process can have significant practical value for obtaining bilayers (or multilayers) [1, 102].

In the dual current pulse regime, it is desirable to have

$$C_B^o >> C_A^o \tag{1.57}$$

the best choice being that which satisfies equality

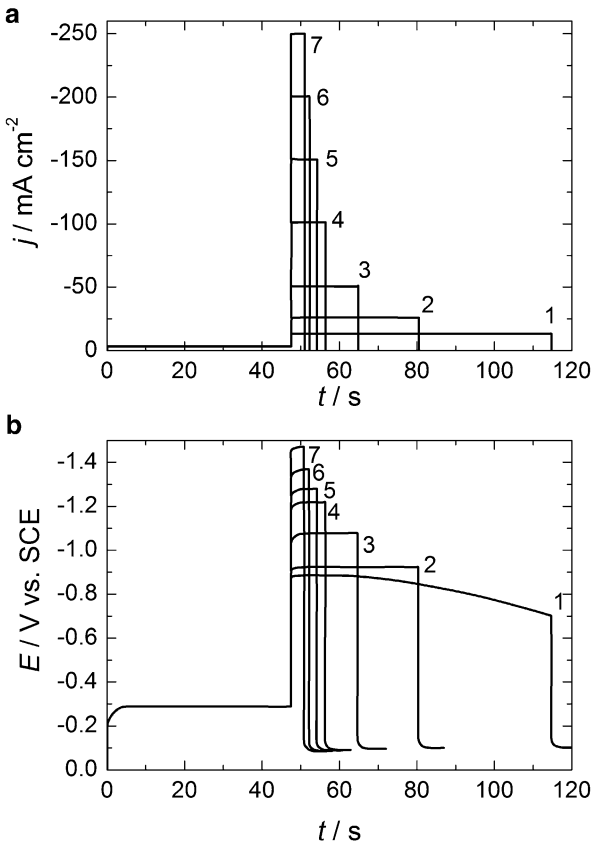

Fig. 1.40 A sequence of high current density pulses (**a**) and corresponding potential responses (**b**) (marked with numbers 1–7) during the formation of two-layer structure composed of a pure (first) Cu layer of about 2 μm and the second layer of different Cu–Ni alloy compositions of a thickness of about 12 μm. The current density ratio, c.r.—$j(\mathrm{Ni})/j(\mathrm{Cu})_{\mathrm{L}}$, for pulse no. 1–2.0, no. 2–5.3, no. 3–13.3, no. 4–27.6, no. 5–36.5, no. 6–56.1, no. 7–61.5 (Reprinted from [102] with the permission of Electrochemical Society)

$$\frac{C_{\mathrm{B}}^{\mathrm{o}}}{j(\mathrm{II})} = \frac{C_{\mathrm{A}}^{\mathrm{o}}}{j(\mathrm{I})}. \tag{1.58}$$

An attempt was made to deposit two-layer structure composed of pure (first) Cu layer of about 2 μm and the second layer of different Cu–Ni alloy compositions of a thickness of about 12 μm by applying dual current pulse regime presented in Fig. 1.40. The two layers were deposited onto Ag RDE (RPM = 1,000) from the solution 0.02 M $CuSO_4$ + 2 M $NiSO_4$ + 0.5 M $Na_3C_6H_5O_7$. The value of the current density in the first pulse, $j(\mathrm{I})$, was adjusted at 75 % of the value of the diffusion limiting current density for copper ions at the given concentration and rotation speed [102].

Table 1.5 The composition of the second layer of the deposits as a function of the current density ratio (c.r.)

		Composition of the second layer			
		EDS analysis		Calculated from c.r.	
Pulse no.	c.r.	at.% Cu	at.% Ni	at.% Cu	at.% Ni
1	2.0	35.4	64.6	33.3	66.7
2	5.3	20.8	79.2	16.0	84.0
3	13.3	7.9	92.1	7.0	93.0
4	27.6	4.9	95.1	3.5	96.5
5	36.5	4.7	95.3	2.7	97.3
6	56.1	3.9	96.1	1.7	98.3
7	61.5	4.2	95.8	1.6	98.4

Reprinted from [102] with the permission of Electrochemical Society

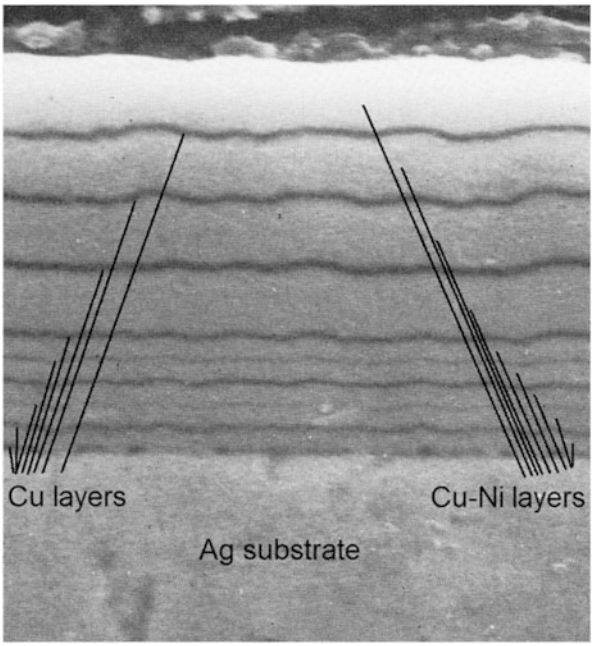

Fig. 1.41 Multilayer structure obtained by the current pulses presented in Fig. 1.42 (Reprinted from [102] with the permission of Electrochemical Society)

Relatively, smooth deposits, consisting of two well-defined layers, are obtained. Results of the EDS analysis of the composition of the second layer (Cu–Ni alloy) of the deposits obtained by the current regimes shown in Fig. 1.40 are compared in Table 1.5 with the composition of the second layer calculated from the current density ratio in the second pulse assuming 100 % current efficiency for alloy deposition, c.r.—$j(\mathrm{Ni})/j(\mathrm{Cu})_{\mathrm{L}}$. Taking into account precision of the EDS analysis, it is seen that a relatively good agreement is obtained.

A multilayer structure consisting of ten relatively thick layers shown in Fig. 1.41 was obtained by the current regime presented in Fig. 1.42.

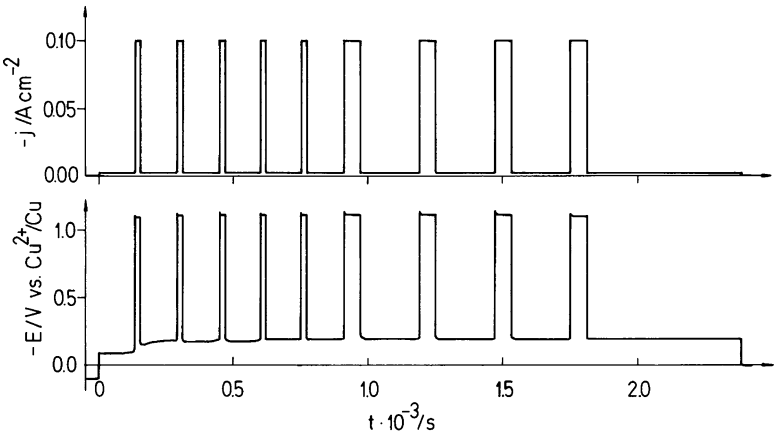

Fig. 1.42 Current density pulses and corresponding potential responses applied for the formation of multilayer structure presented in Fig. 1.41 (Reprinted from [102] with the permission of Electrochemical Society)

Presented analysis confirmed that the thickness and the composition of layered deposits could be controlled with sufficient precision [102].

1.4.2.3 Intermediate Layer Detection

Taking into account the fact that the intermediate layer in deposited laminar metal structures plays an important role in obtaining improved mechanical and magnetic properties [93], from 1980 to 2000 particular attention has been given to the pulsating regimes which would provide as thin as possible layers (of the order of nanometers) [105–109] in multilayered metal structures, and, accordingly, much higher surface area of the intermediate layer.

In theoretical consideration of multilayer deposition of Cu–Ni alloy under the conditions of convective diffusion [103], it was shown that a constant concentration of Cu in the second layer (Cu–Ni alloy) could be established at different thicknesses of the second layer, depending on the value of the current density of a second pulse and the rotation rate. As the value of the current density in the second pulse increases, the thickness at which a constant concentration of Cu could be established also increases, indicating that the thickness of the intermediate layer also increases, reaching the maximum value of about 150 nm [103]. Unfortunately, this theoretical consideration was not experimentally confirmed. Most of the experimentally confirmed theoretical treatments of the pulsed deposition of multilayer have been applied to the Cu–Ni system [110–113]. Equations for partial currents for copper and nickel deposition [19, 111] (including the evolution of hydrogen) from a single bath in the case of galvanostatic [110] and potentiostatic [111] deposition of multilayered Cu–Ni coatings under the conditions of convective diffusion were developed. The experimental

results were in good agreement with the theoretical predictions. The subject of two papers [112, 113] was the process taking place during the off-time period in pulsed deposition, showing that during the off-time period copper deposits by a displacement of nickel ("replacement reaction"). These models were found to agree well with the experimental findings. Hence, the existence of an intermediate layer in these investigations has not been confirmed experimentally.

However, it was shown in the system Cd–Ni [114] that the intermediate layer could be detected by the application of the ALSV technique. Alloy samples used for the ALSV analysis were galvanostatically deposited at the amount of charge of 1 C cm^{-2} in the solution containing 2 M $NiSO_4$ + 0.2 M $Na_3C_6H_5O_7$ + 0.002 M $CdSO_4$. Pure Ni and Cd layers were also deposited galvanostatically at $j_d = -10$ mA cm^{-2} ($Q_d = -1$ C cm^{-2}) from the solutions containing 2 M Ni $(NH_2SO_3)_2$ + 0.5 M H_3BO_3 and 0.5 M $CdSO_4$ + 0.01 M H_2SO_4, respectively. The samples composed of a layer of alloy and a layer of pure Cd on top of the alloy layer, used for the analysis of the intermediate layer existence, were galvanostatically deposited from two different baths: 2 M $NiSO_4$ + 0.2 M $Na_3C_6H_5O_7$ + 0.002 M $CdSO_4$ and 2 M $Ni(NH_2SO_3)_2$ + 0.5 M H_3BO_3 + 0.002 M $CdSO_4$. All samples were dissolved in a solution of 1 M NaCl (pH 2).

Intermediate Layer Between Ni and Cd Deposited from a Separate Baths

For this purpose layers of pure Cd and pure Ni were deposited from the appropriate separate baths onto gold disc electrode. To provide normal dissolution of these metals, Ni was first deposited as a more noble metal and a layer of Cd was deposited on top of it. From such a deposit Cd dissolves at about −0.8 to −0.7 V, while Ni starts to dissolve at about −0.33 V with the peak appearing at about −0.1 V.

Hence, to detect an intermediate layer between these two metals, ALSV's of pure Ni and pure Cd dissolution were first recorded. Then, after the deposition of a layer of Cd on top of a layer of Ni, an ALSV of dissolution of a deposit consisting of two metal layers was recorded. Since these two metals make two intermediate phases [15], in the case of interaction between the two layers, one would expect one or two small ALSV peaks, pertaining to the dissolution of either of these phases, between the peaks of dissolution of pure metals. There was no indication, however, of the existence of any additional ALSV peak even after prolonged thermal treatment (deposit was kept in an atmosphere of purified nitrogen at a temperature of 50 °C for 24 h) of such deposit. Knowing that the ALSV technique is very sensitive and that it is possible to detect clearly a monolayer of metals by this technique, it seems that in the case of Ni and Cd layers, deposited from separate baths, no intermediate layer between them is formed.

Intermediate Layer Between Cd–Ni Alloy and Pure Cd Deposited from a Single Bath

In the case of Cu–Ni alloy, detection of an intermediate layer by the ALSV technique is impossible, since these two metals make a series of solid solutions

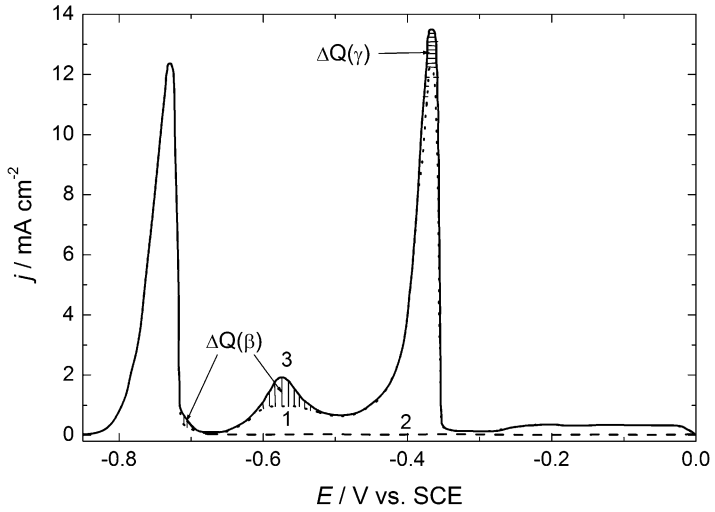

Fig. 1.43 The example of the ALSV's of Cd–Ni alloy dissolution (*dotted line*, 1), pure Cd dissolution (*dashed line*, 2) and dissolution of a two layer deposit (*solid line*, 3) composed of a layer of Cd–Ni alloy and a layer of pure Cd deposited on top of a layer of the alloy (Reprinted from [114] with the permission of Elsevier)

and the potentials of dissolution of pure metals in solution 1 M NaCl, pH 2, are very close. However, the system Cd–Ni should be very suitable for this purpose, since the ALSV's of Cd–Ni alloys dissolution are seen to be characterrized by the existence of two ALSV peaks corresponding to the dissolution of phases β and γ of the formula $NiCd_5$ and NiCd, respectively [15, 114]. Hence, if there exists the intermediate layer, it should be composed of these phases [1]. By comparing ALSV of dissolution of a single layer of the alloy with the ALSV of dissolution of the two-layers deposit, it is possible to detect an intermediate layer between these two layers. An example is shown in Fig. 1.43. Curve 1 represents the ALSV of the alloy dissolution without the Cd layer on top, curve 2 the ALSV of pure Cd dissolution, while curve 3 represents the ALSV of the two-layers deposit dissolution. As can be seen curves 1 and 3 are different, with the peaks of β- and γ-phase dissolution being somewhat higher on the curve 3, while the peak of pure Cd dissolution does not change. As the content of Ni in the alloy layer increases, the difference between these two ALSV curves becomes smaller.

Hence, the difference between curves 3 and 1 (shaded areas on Fig. 1.43) should represent the intermediate layer. By integration of the surface of shaded areas, it is possible to obtain the charges (amounts) corresponding to the increase of β and γ phases in the two-layer deposit [marked in the figure as $\Delta Q(\beta)$ and $\Delta Q(\gamma)$], which should be a consequence of the formation of an intermediate layer between a layer of alloy and a layer of pure Cd. Thus, the intermediate layer is mainly composed of β and γ phases, which is in good agreement with the theory of an intermediate layer in laminar metal structures [93].

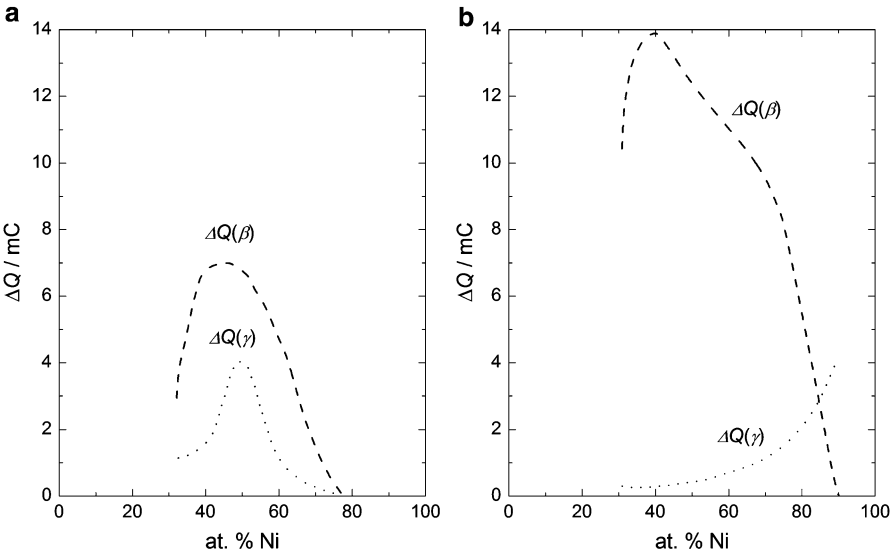

Fig. 1.44 The charges corresponding to the contribution of the β and the γ phases in the intermediate layer obtained by the analysis of the ALSV's of two-layer deposits dissolution. Alloys were deposited from the solutions containing: (**a**) 2 M $NiSO_4$ + 0.2 M $Na_3C_6H_5O_7$ + 0.002 M $CdSO_4$; (**b**) 2 M $Ni(NH_2SO_3)_2$ + 0.5 M H_3BO_3 + 0.002 M $CdSO_4$ (Reprinted from [114] with the permission of Elsevier)

These investigations were performed with the two-layers deposits obtained from two different baths (as stated above). The recorded charges $\Delta Q(\beta)$ and $\Delta Q(\gamma)$, obtained for both investigated baths for alloy deposition, are shown in Fig. 1.44 as functions of alloy layer composition. As can be seen in the figure, the intermediate layer composition is slightly different in the two cases. The amount of the β phase in the intermediate layer is seen to reach its maximum value at about the same alloy composition (30–40 at.% Ni) in both cases, while the contribution of the γ phase in the intermediate layer is different in two-layer deposits obtained from different baths. Such a behavior clearly indicates that the composition of an intermediate layer is sensitive to the composition of the electroplating bath, since the conditions of deposition were identical in both cases.

Assuming that both phases are homogeneously distributed in the intermediate layer, the intermediate layer thickness can be calculated from the charges recorded on the ALSV's. From the formula of the β phase (Cd_5Ni), one can determine the charge corresponding to Ni as 0.167 and to Cd as 0.833 of total charge $\Delta Q(\beta)$ and in a similar way for the γ phase [Ni 0.5 and Cd 0.5 of $\Delta Q(\gamma)$]. Using these charges and corresponding values of the density and molecular weights of the two metals, the thicknesses of β and γ phases in the intermediate layer can be calculated. Hence, the total thickness of the intermediate layer should represent the sum of the thickness of individual phases. Figure 1.45 shows the dependence of the thickness of β and γ phases and the total thickness of an intermediate layer (d_{il}) as a function of alloy

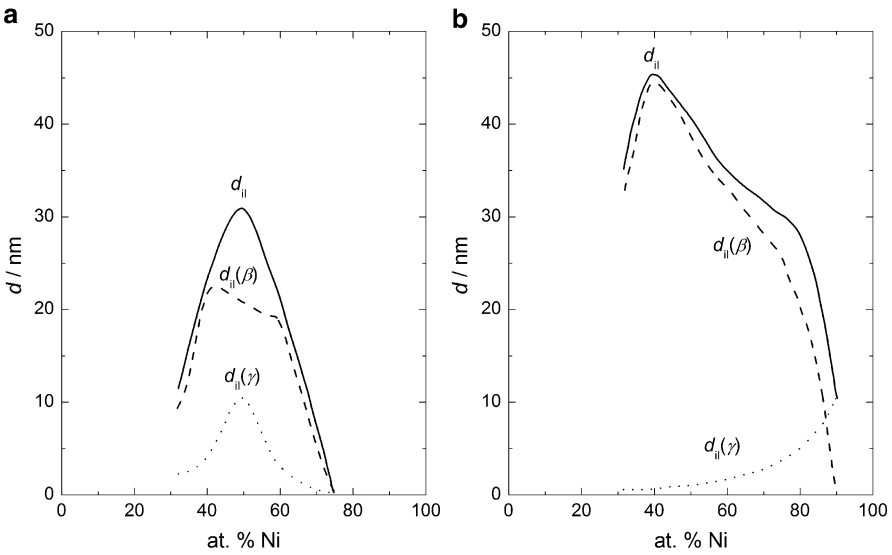

Fig. 1.45 The thickness of the individual phases, $d_{il}(\beta)$ and $d_{il}(\gamma)$, and the intermediate layer, d_{il}, obtained by the analysis of the results presented in Fig. 1.44 (Reprinted from [114] with the permission of Elsevier)

composition, obtained by the analysis of the results presented in Fig. 1.44. As can be seen the thickness of the intermediate layer depends on the solution for alloy deposition, and its maximum value is about 45 nm. Hence, in certain systems it is possible to estimate the thickness and the surface of intermediate layer by the application of ALSV technique.

1.4.2.4 Mechanical and Magnetic Properties of Multilayered Structures

Mechanical properties of multilayered structures were only investigated for deposits containing Cu/Cu–Ni layers. Following mechanical properties were mainly investigated: Young's modulus [98], hardness [115], and tensile strength [107, 115–117]. It is shown that all investigated properties depend on the thickness of the individual layers and that in all cases multilayered structures showed better properties than that of pure metals and/or their alloys.

The results of hardness investigation [115] are presented in Fig. 1.46. As can be seen maximum hardness for the deposit containing Cu/Ni−100 layers was achieved at the thickness of individual layers of 12 nm. These results are not in agreement with those detected for evaporated layers Cu/Ni−111 [116], where the maximum hardness was obtained for individual layer thickness of 1.6 nm, indicating that, most probably, the hardness depends on the thickness and the total surface area of

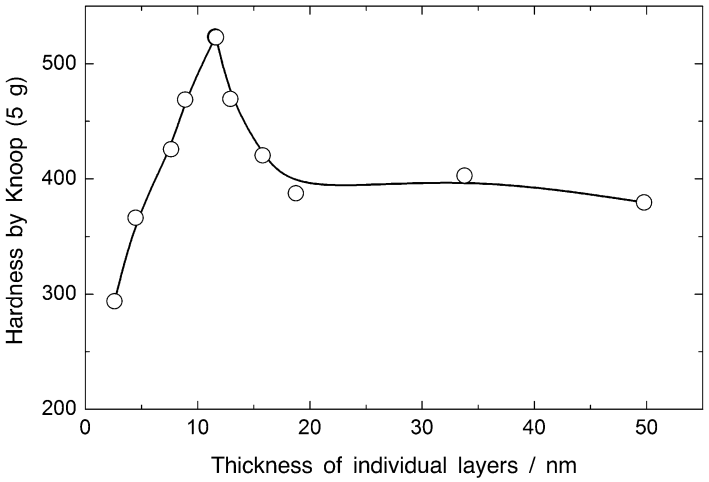

Fig. 1.46 The hardness of the deposit containing Cu/Ni – 100 layers as a function of the thickness of individual layers (Reprinted from [115] with the permission of Elsevier)

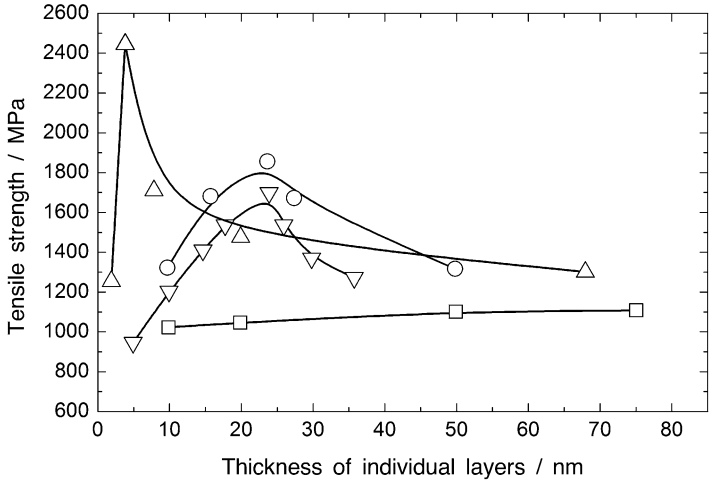

Fig. 1.47 The tensile strength of the multilayered deposits as a function of the thickness of individual layers: *open circle*—[107]; *open square*—[117]; *open triangle*—[118]; *open inverted triangle*—[108] (Reprinted from [109] with the permission of Elsevier)

the intermediate layer which is different for different techniques of multilayered structure formation.

In several investigations the influence of the individual layer thickness on the tensile strength was reported [106, 114, 116, 117]. The results of these investigations are presented in Fig. 1.47. Significant difference in the obtained results is

Table 1.6 Tensile test for electroformed 90 % Ni − 10 % Cu multilayers vs. Cu layer thickness

Cu layers (nm)	UTS (MPa)	YS (MPa)	Modulus (GPa)	Strain (%)
1.0	1,021	795	160	2.4
2.0	1,056	840	152	2.4
2.0	1,029	881	141	1.4
5.0	1,107	893	147	2.0
7.5	1,116	844	154	2.1
7.5	1,116	848	151	2.7
10.0	1,069	807	145	2.8
12.5	978	789	154	1.5
15.0	863	724	130	1.2
		Averages	148 (±18)	2.1 (±0.9)

Reprinted from [108] with the permission of Electrochemical Society

mainly the consequence of different parameters of the deposition process (bath composition, pulse regimes, temperature, etc.). A common explanation for the decrease of tensile strength with the increase of individual layer thickness (after the maximum value) is the increase of the coherence of the intermediate layer. It is concluded that with the decrease of the number of dislocations in the intermediate layer, the probability of their transfer from it to previous or subsequent layer increases, resulting in the decrease of tensile strength.

The dependence of the tensile properties of multilayered Cu–(Ni–Cu) deposits, with the nominal overall composition 90 at.% Ni−10 at.% Cu, was investigated in the work of Tench and White [108] as a function of the Cu layer thickness (varying from 1 to 15 nm). Multilayers of the nominal thickness of 50 μm were deposited from a commercial sulfamate bath with the addition of 5 mM $CuSO_4$. Pure Cu layers were plated at −0.14 V vs. SCE with cathode rotation at RPM = 750, while Ni layers (with 0.8 at.% Cu) were plated at $j = -105$ mA cm^{-2} from the stagnant bath. The results of the tensile properties (ultimate tensile strength, UTS, yield strength, YS, modulus, and strain) measurements are presented in Table 1.6. Considering X-ray data it was concluded that a decrease in the enhanced strength for such deposits, producing peak at a Cu layer thickness of about 7 nm, is associated with a decrease in the deposit (100) texture (normally established for Ni layers) and an increase in the (110) orientation preferred for Cu deposits.

Concerning the magnetic properties, giant magnetoresistance, which is a significant decrease of electric resistance in the presence of magnetic field, characteristic effect for multilayered structures, has been discovered in 1988 for the systems Fe/Cr/Fe and Fe/Cr by Grünberg and Fert (these scientists received Nobel Prize for physics in 2007). This phenomenon has also been recognized for electrodeposited multilayered structures [119–123]. The strongest effect is detected for multilayered Co–Cu/Cu [121] and Co–Ni–Cu/Cu [122, 123] structures, while less pronounced effect is detected for the multilayered Ni–Cu/Cu [121] structures. It is important to note that the presence of the intermediate layer of the thickness of 2–3 nm has been detected for the first time by high resolution transmission electron microscopy (HRTEM) for the multilayered Ni–Cu/Cu structures [119], as shown in Fig. 1.48.

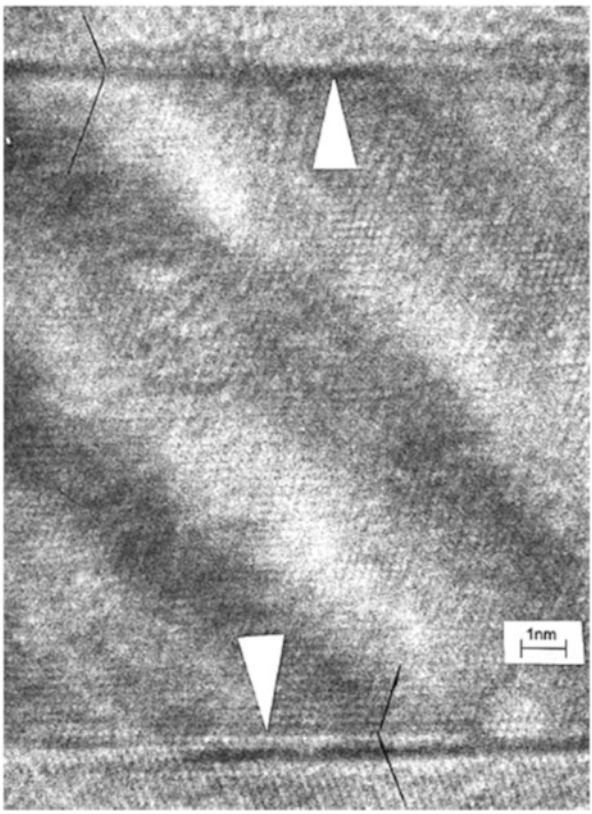

Fig. 1.48 HRTEM picture taken on the Ni–Cu (3.8 nm)/Cu(1.4 nm) sample which shows the atomic structure of a twin boundary (indicated by the *arrow*) and the magnetic/nonmagnetic layers (Reprinted from [119] with the permission of Elsevier)

1.4.3 Metal Coatings with Inclusion of Nonmetallic Particles

The basics of deposition of composite coatings containing metal and nonmetallic particles are given in the literature in chapter of Despić and Jović [1] and in a review paper of the electrochemical engineering group of Southampton University [92]. Despić and Jović [1] summarized results obtained in this field up to about 1993 in 28 available references, while review paper of Low et al. [92] presented mostly recent literature survey of the deposition of metallic coatings containing nano-sized particles citing 82 references. In this survey [92] are summarized various types of nano-structured materials obtained by electrodeposition, examples of theoretical models used to describe such a process, investigations of the inclusion of Al_2O_3, SiC, SiO_2, ZrO_2, diamond, Si_3N_4, TiO_2, etc. into metal matrix of Ni, Cu, Au, Zn, and Fe, types of current density pulses used for these investigations, effects of nano-sized particles on deposit characteristics, influence of bath agitation and cathode movement, and examples of studies using rotating cylinder electrode and other operating parameters (pH, bath temperature, type of additives and concentration of metal ions, and additives). Also, gradient distribution of particles and

properties of nano-composite deposits (corrosion rates, microhardness, wear resistance, magnetic properties) as a function of the deposition parameters are discussed. In almost all of the cited references in these two publications, the authors are either explaining the mechanism of codeposition or the influence of deposition parameters on the mechanical, tribological, corrosion, and magnetic properties of obtained composite structures. Recently, Cattarin and Musiani [124] published review of the studies carried out during the last decade on the electro-synthesis of oxide-matrix composite materials for electrocatalysis of the HER [125–134] and the oxygen evolution reaction [135–145] (OER), citing 71 references. In this review [124] particular attention has been given to the oxide-matrix composite materials for electrocatalysis of the OER. The matrix materials were PbO_2, Ni, Tl_2O_3, and PbO_2/CoO_x, while as dispersed phases Co_3O_4, RuO_2 or Ru + Sn oxides, and Co_2NiO_4 were used. In comparison with the pure matrices, composite anodes exhibited much lower overpotentials and lower Tafel slopes, comparable to those of electrocatalytic materials produced by other methods.

Taking into account that the review concerning oxide-matrix composite materials for electrocatalysis of the OER has already been published [124], in the next part of this chapter deposition of composite coatings containing metals and non-metallic (oxide) particles as catalysts for the HER will be presented and discussed.

1.4.4 Ni Based Coatings with Inclusion of Nonmetallic Particles as Cathodes for the HER

Two types of Ni-based composite coatings were investigated: (i) composite coatings of large surface area containing Co_3O_4 and RuO_2 particles [146], composite coatings containing RuO_2 and IrO_2 particles [147, 148] and TiO_2 particles [134]; (ii) composite coatings containing MoO_2 particles [150–153].

1.4.4.1 Composite Coatings Containing Co_3O_4, RuO_2, IrO_2, and TiO_2 Particles

All composite coatings were deposited from suspensions stirred with a magnetic bar (at ca. RPM = 1,000) onto disc electrodes rotating at RPM = 2,500, under galvanostatic control. The Ni + RuO_2 composites were deposited from suspensions of RuO_2 in either of the following electrolytes: 0.2 M $NiCl_2$ + 2 M NH_4Cl aqueous solution, pH 4.5, at 25 °C; Watt's bath containing 1.126 M $NiSO_4 \cdot 6H_2O$ + 0.185 M + $NiCl_2 \cdot 6H_2O$ + 0.485 M H_3BO_3, pH 4, at 55 °C at low current densities (−0.02 to −0.1 A cm^{-2}). The deposits obtained from the former bath at high current densities (−0.5 to −3.0 A cm^{-2}) are called Por–Ni + RuO_2 and those obtained from the latter one are called Watt–Ni + RuO_2. Similarly, Por–Ni and Por–Ni + Co_3O_4 are plated from the former solution (at high current densities) [146]. The Tafel plots for the HER

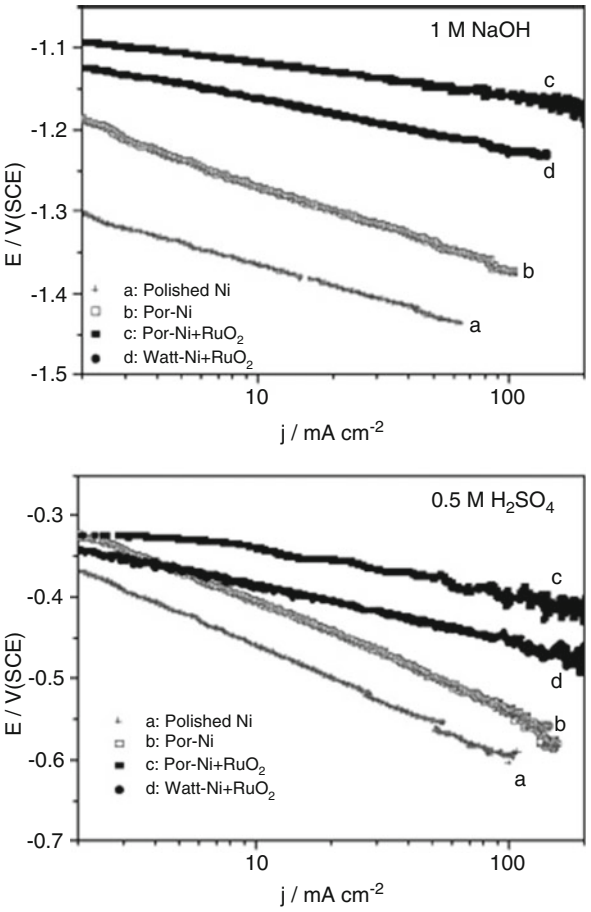

Fig. 1.49 Tafel plots of the current density potential curves for the HER measured on polished Ni (a), Por–Ni (b), Por–Ni + RuO_2 composite, $\alpha = 0.18$ (c) and Watt–Ni + RuO_2 composite, $\alpha = 0.28$ (d) in 1 M NaOH and 0.5 M H_2SO_4 (Reprinted from [146] with the permission of Elsevier)

on some of the investigated cathodes, recorded with *IR* drop correction, are presented in Fig. 1.49. As can be seen the most active electrode, in either alkaline or acidic solution, is Por–Ni + RuO_2, mainly due to high surface area in comparison with Por–Ni and Watt–Ni + RuO_2, while all composites show catalytic effect for the HER. This is confirmed by the SEM analysis of surfaces of composite coatings obtained in this work, presented in Fig. 1.50. It was also shown that composite coatings based on IrO_2 particles [148] did not possess catalytic effect for the HER.

Composite Ni–P + TiO_2 coatings were also deposited onto stationary Cu plate from a bath for deposition of Ni–P containing 99 g dm^{-3} TiO_2 powder, which was stirred with RPM = 300. It was shown that the increase in electrochemical activity of the Ni–P + TiO_2 electrode towards the HER is due to both the presence of titanium oxides and the increase in the real surface area, as compared with the Ni–P electrode [134].

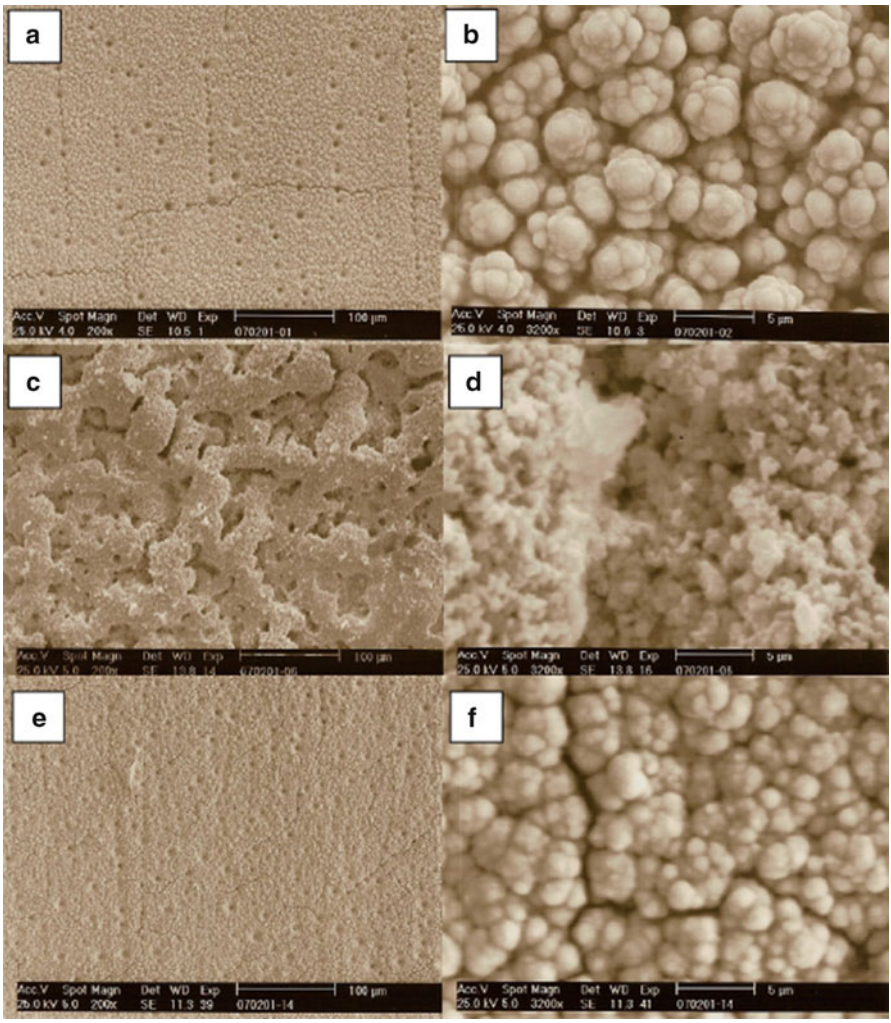

Fig. 1.50 SEM pictures of deposits obtained from 0.2 M $NiCl_2$ + 2 M NH_4Cl aqueous solution, pH 4.5, with a deposition current density -3.0 A cm^{-2}. (**a**) and (**b**) Por–Ni; (**c**) and (**d**) Por–Ni + RuO_2, from a 50 g dm^{-3} RuO_2 suspension; (**e**) and (**f**) Por–Ni + Co_3O_4, from a 50 g dm^{-3} Co_3O_4 suspension (Reprinted from [148] with the permission of Elsevier)

1.4.4.2 Composite Ni–MoO_2 Coatings as Cathodes for the HER in Industrial Electrolysis

Composite coatings containing MoO_2 [150–153] particles (average size 200 nm) were deposited at $j = -300$ mA cm^{-2} from the solution 0.2 M $NiCl_2$ + 2 M NH_4Cl (pH 3.8) containing MoO_2 powder particles, in the apparatus (pilot plant of small dimensions) schematically presented in Fig. 1.51. The volume of the electrolyte in

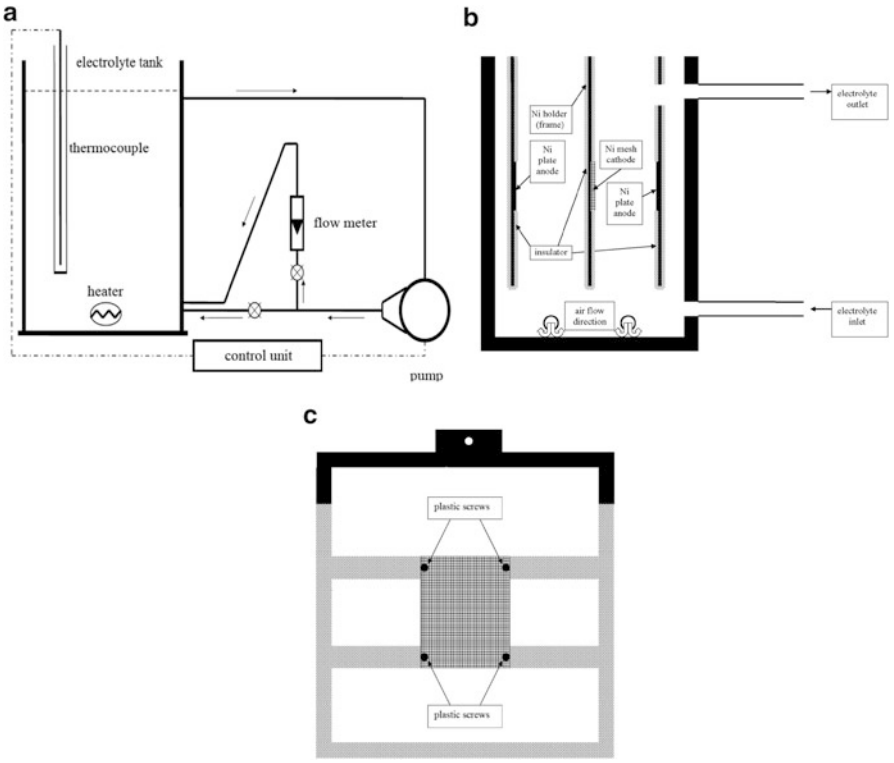

Fig. 1.51 Schematic presentation of the apparatus for deposition of Ni–MoO_2 composite coatings (Reprinted from [149] with the permission of Int. J. Hydrogen Energy)

the cell for deposition was approximately 20 dm^{-3}. The electrolyte was circulated with the pump with a maximum flow rate of 0.83 $dm^3\ s^{-1}$ (a). The flow rate in the cell was measured with a flow meter (a), being 0.33 $dm^3\ s^{-1}$. Additional mixing of the electrolyte was provided by the airflow of 0.17 $dm^3\ s^{-1}$ through two pipes with small openings facing the bottom of the cell in order to remove eventually precipitated MoO_2 particles from the bottom of the cell and to force particles to float and circulate with the electrolyte (b). The temperature of the electrolyte was kept constant by the thermocouple, heater, and the control unit (a). The Ni 40 mesh cathode, connected to a Ni holder (frame), was placed between two Ni anode plates, as is schematically presented in (c). A homemade power supply, with the ripple smaller than 1 %, was used for applying necessary current/voltage [149, 150].

Four samples were deposited under different conditions. Samples 1 and 2 were deposited from the bath with freshly added MoO_2 (after 1 h of electrolyte circulation), while deposition of samples 3 and 4 started 24 h after MoO_2 addition. It appeared that aging of the electrolyte of at least 24 h is necessary for better incorporation of MoO_2 particles in the deposit [150].

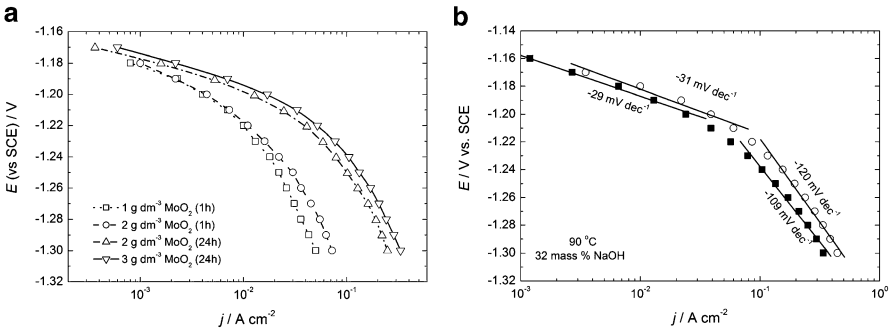

Fig. 1.52 (**a**) Polarization diagrams for the HER measured on samples 1–4. (**b**) Polarization diagrams for the HER measured on sample 4 (*open circle*) compared with that recorded for the commercial De Nora's Ni–RuO_2 cathode (*filled square*) (Reprinted from [150] with the permission of Int. J. Hydrogen Energy)

Polarization characteristics of the HER for samples 1–4, recorded in 32 mass % NaOH at 90 °C and corrected for *IR* drop, are presented in Fig. 1.52a. Significant decrease of overvoltage for the HER is recorded for samples 3 and 4. By comparing polarization diagrams for the commercial De Nora's electrode (■), and the best sample 4 (○), one can see that polarization diagrams are almost identical, Fig. 1.52b, indicating that Ni–MoO_2 composite coatings, deposited under conditions described above in the apparatus presented in Fig. 1.51, could be promising replacement for the commercial cathodes based on the Ni–RuO_2 composite coatings (DN) [150]. Taking into account that in the industrial electrolysis the current density for the HER is usually -0.3 A cm^{-2}, considering polarization curves presented in Fig. 1.52b, it could be concluded that the overvoltage for the HER onto Ni–MoO_2 composite coating is for about 20 mV lower than that on the commercial cathode.

The morphology of the coating deposited in the presence of the highest amount of MoO_2 powder particles (3 g dm^{-3}, sample 4) is presented in Fig. 1.53a. As can be seen, two regions can be detected on the deposit surface. The region rich in Ni with no cracks (low percentage of molybdenum and oxygen), usually positioned at the middle of a Ni mesh wire between the crossing of two wires, and the region rich in Mo with the presence of cracks (high percentage of molybdenum and oxygen and low percentage of nickel) are placed around the position of the crossing of two wires. It is quite difficult to uniformly incorporate MoO_2 particles in the Ni deposit on the Ni 40 mesh, since all places of the surface are not equally accessible to the MoO_2 particles and Ni ions. The position of crossing of two wires is the place where, because of the change of hydrodynamic conditions at this particular position, higher amount of MoO_2 particles is embedded in the Ni deposit, probably as a result of lower real current density for Ni deposition. The uniform composition of the Ni–MoO_2 composite coating could probably be achieved by improving hydrodynamic conditions. The cross section of the Ni-rich part of the coating is presented in Fig. 1.53b. The EDS analysis showed that white areas (b) are rich in Mo, but the

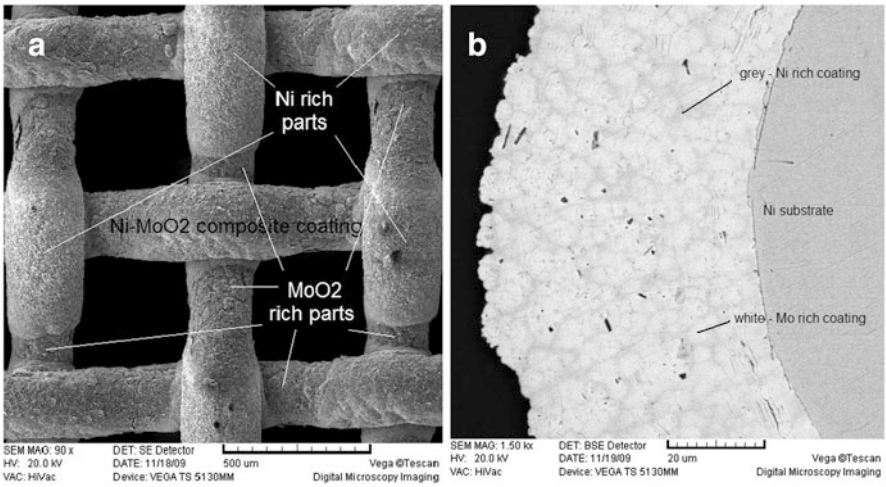

Fig. 1.53 (**a**) Surface of the sample 4, SEM. (**b**) Cross section of the Ni-rich part of the coating, backscatter SEM (Reprinted from [151] with the permission of Elsevier)

content of Ni is still high (around 79 at.%) and the content of oxygen is low. Hence, white areas correspond to agglomerates of MoO_2 surrounded with Ni and incorporated into Ni matrix (gray areas) [150].

This statement is confirmed by the XRD analysis of as-deposited sample 4 and XRD analysis after additional thermal treatment. The coating was thermally treated in air atmosphere for 5 h at two different temperatures, 300 and 600 °C. As shown in Fig. 1.54, in the XRD pattern of the as-deposited sample only Ni peaks could be detected, indicating amorphous (or nano-crystalline) MoO_2. After recrystallization at 300 and 600 °C, peaks of MoO_2 are clearly seen in the XRD pattern of sample 4 [150].

Hence, considering polarization curves presented in Fig. 1.52b it appears that the overvoltage for the HER onto Ni–MoO_2 composite coating is for about 20 mV lower than that on the commercial cathode. However, this is not the only criteria that should be satisfied for the application of such cathodes in industrial electrolysis. The "service life" test should also give satisfactory results.

Service Life Test

In the process of chlor-alkali electrolysis for chlorine production in the membrane cells [154–156], an ion-exchange membrane separates the anode and the cathode compartments and gaseous hydrogen is produced in the cathode compartment from 30 to 32 mass % caustic soda solution at a typical operating temperature of 90 °C. The efficiency of the cathodes is an important issue in this process, since the overvoltage for the HER in the cathode compartment contributes significantly to

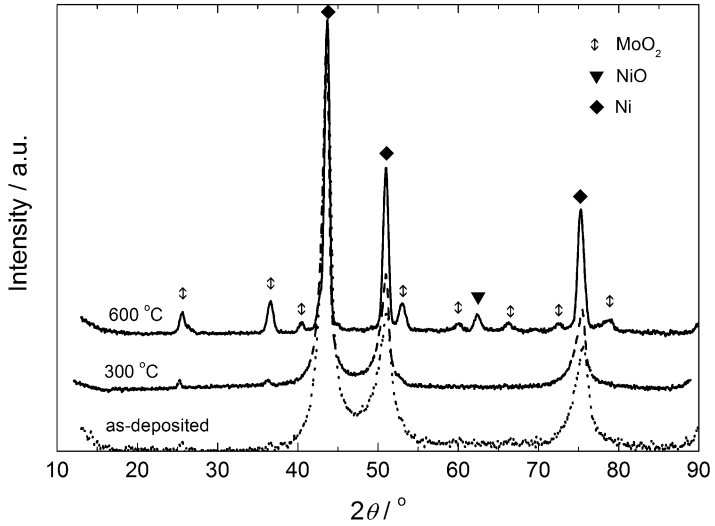

Fig. 1.54 XRD pattern of as-deposited sample 4, the same sample after annealing at 300 °C for 5 h in air (300 °C) and after additional annealing at 600 °C for 5 h in air (600 °C) (Reprinted from [150] with the permission of Int. J. Hydrogen Energy)

the overall power consumption. The efficiency of the cathodes is a result of combination of certain activity and stability at current densities (0.3–0.6 A cm^{-2}) normally used in industrial applications. The main reason for the loss of activity and stability of the cathodes during long-term operation is the so-called polarity inversion of the electrodes, which takes place during the replacement of old electrodes of an electrolyzer with new ones in the zero-gap cells. During this operation anodes and cathodes are short-circuited, causing a reverse current flow which may damage the cathodes and negatively affect their activity for the HER [156]. The manufacturers can predict how often in a certain period of time such operation should be performed and, in accordance with that, design an appropriate accelerated "service life" test for cathodes [148, 151, 153].

Such test was performed in the following way: the electrode was kept at $j = -0.3$ A cm^{-2} for 0.5 h and the corresponding potential response was recorded. After that, the electrode was cycled (five cycles) in the potential range from -1.25 V (HER) to 0.5 V (OER) with a sweep rate of 50 mV s^{-1}. In the next step the electrode was kept again at $j = -0.3$ A cm^{-2} for 500 s and the corresponding potential response was recorded. This procedure was repeated five times, until the number of cycles reached 25. The potential response measured at $j = -0.3$ A cm^{-2} for 500 s (the value recorded at the last point, 500 s) was corrected for IR_Ω drop using the value of ohmic resistance (R_Ω) obtained from EIS measurements. The results of this test for the composite Ni–MoO_2 coating (sample 4) and the commercial De Nora's electrode (DN) are presented in Fig. 1.55. As can be seen the performance of the Ni–MoO_2 coating (sample 4) after "service life" test confirmed

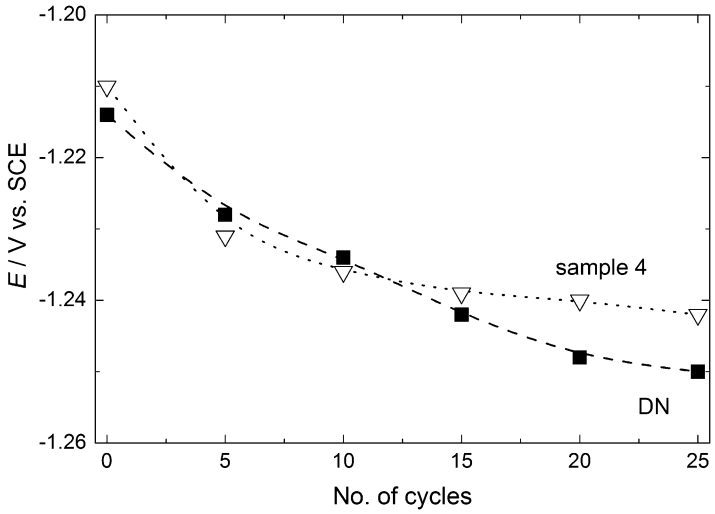

Fig. 1.55 The results of "service life" test for the commercial De Nora's electrode (DN) and composite Ni–MoO_2 coating (sample 4), potential for the HER corrected for IR_Ω drop at the current density $j = -0.3$ A cm^{-2}

that this electrode could be promising replacement for the commercial one, showing slightly lower overvoltage for the HER after 15 cycles.

The appearances of the coating after its cathodic polarization at -0.3 A cm^{-2} for 40 h and after the "service life" test are presented in Fig. 1.56a, b, respectively. As can be seen the appearance of the coating did not change after 40 h of the HER (Figs. 1.53a and 1.56a), while Mo-rich parts were mainly destroyed and peeled from the Ni mesh surface after the "surface life" test (Fig. 1.56b). Taking into account the presence of the large number of cracks in the Mo-rich parts of the Ni–MoO_2 coating, the loss of the coating (and consequently the loss of activity) is most likely due to erosion caused by the evolved gas. It is well known that the effective catalytic activity does not correlate always with the total surface of the catalyst, especially with the inner surface. In the case of Raney–nickel cathodes [158], utilization of the inner surface for the HER does not exceed on the average 10 % at the high current densities. This low degree of catalyst utilization is due to slow diffusive mass transport of electrogenerated dissolved hydrogen out of the pores and cracks of the catalyst. Hydrogen bubbles cannot precipitate in nanometer pores unless the concentration of the hydrogen in the electrolyte exceeds high concentration. It is clear that the higher exchange current density of the evolved gas reaction, the lower the penetration depth and catalyst utilization. Taking into account the fact that this electrode exhibits high catalytic activity for the HER, due to diffusive mass transport limitation of dissolved hydrogen, it could be expected that this reaction practically does not take place in the pores and cracks present in the coating. Consequently, the mechanical damage was not caused by the evolved hydrogen bubbles, which is confirmed in Fig. 1.56a. However, during cycling procedure

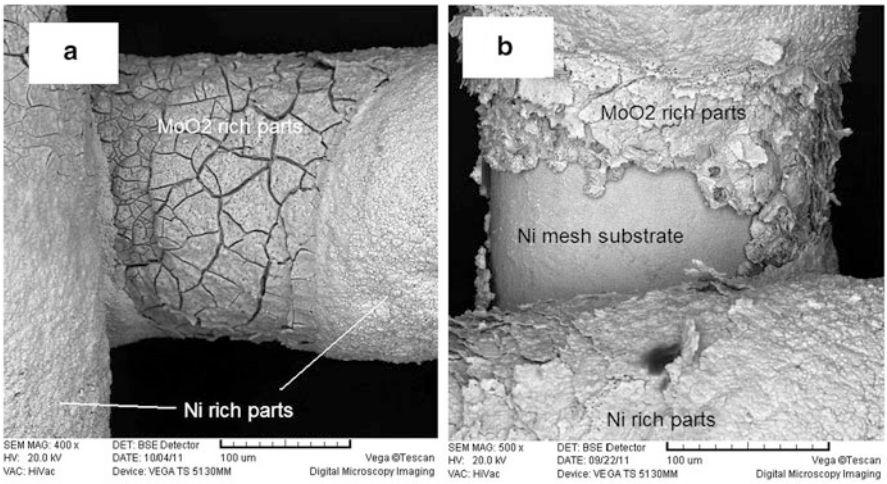

Fig. 1.56 (**a**) Surface of the sample 4 after 40 h of the HER at $j = -0.3$ A cm^{-2}, SEM. (**b**) Surface of the sample 4 after "service life" test (Reprinted from [151] with the permission of Elsevier)

(inverse polarization), the OER takes place on examined electrodes reaching very high current densities of 0.3–0.4 A cm^{-2} during anodic polarization. Unlike the HER, the OER is a highly irreversible reaction and due to its very low exchange current density it takes place at overall catalyst surface without any diffusion limitation in the pores and cracks. So, the rapid evolution of oxygen on Mo-rich parts of the Ni–MoO_2 coating generated significant pressures within the porous coating causing their mechanical damage (erosion). The EDS analysis of the surface of the Ni–MoO_2 coating showed that the percentage of Ni and Mo was practically the same before and after the "service life" test, indicating that during the replacement of old electrodes with the new ones (inverse polarization) no dissolution and further oxidation of MoO_2 could take place.

1.5 Conclusions

In this chapter basics of electrodeposition of alloys from aqueous solutions are presented, taking into account conditions that must be fulfilled for deposition of alloys, their reversible potentials in the solutions of corresponding ions, the influence of the Gibbs energy of phase formation, and stability of such alloy phases in the solutions of corresponding ions.

Different types of alloy deposition (equilibrium, irregular, regular, anomalous, and induced codeposition) are defined, being ascribed to certain systems, such as Ni–Sn, Ag–Pd, Ag–Cd, Co–Ni, and Fe–Mo, respectively.

Characterization of electrodeposited alloys by ALSV is explained in great detail for the eutectic-type alloys (systems Cu–Pb, Cd–Co, and Cd–Zn), solid solution type alloys (systems Ag–Pd and Co–Ni) and alloys containing intermediate phases and/or intermetallic compounds (systems Cd–Cu, Cd–Ni, Ag–In, and Ag–Cd). Based on the presented results of ALSV technique application to different alloy systems, a mechanism of alloy dissolution is proposed.

In the part concerning electrodeposition of composite metal coatings, two types of deposits are described: laminar metal structures and metal coatings with inclusion of nonmetallic particles. Basic equations and conditions for deposition of laminar metal structures are given, together with the explanation of the improvement of their mechanical and magnetic properties (based on the existence of the intermediate layer of high surface area) in comparison with their alloys or pure metals. In the case of metal coatings with inclusion of nonmetallic particles, particular attention is addressed to their catalytic properties for hydrogen and oxygen evolution reactions.

Acknowledgments This work was financially supported by the Ministry of Education, Science and Technological Development of the Republic of Serbia through the Project No. 172054/2011.

The authors also wish to express their gratitude to the Department of Research and Development of De Nora Industries S.p.A. for providing equipment for electrodeposition of Ni–MoO_2 coatings.

References

1. Despić AR, Jović VD (1995) Electrochemical Deposition and Dissolution of Alloys and Metal Composites – Fundamental Aspects. In: White RE, Bockris JO'M, Conway BE (eds) Modern Aspects of Electrochemistry. vol. 27, Plenum Press, New York, pp. 143–232
2. De Ruolz M (1842) C R Acad Sci 15:1140
3. Srivastava RD, Mukerjee RC (1976) J Appl Electrochem 6:321
4. Brenner A (1963) Electrodeposition of Alloys: Principle and practice. Academic Press, New York
5. Bondar VV, V. Grimina V, Pavlov VN (1980) Itogi nauki i tehniki, Elektrokhimiya. vol. 16, Izd. Viniti, Moscow
6. Spitzer F (1905) Z Electrochem 11:345
7. Schlötter M (1914) Die Elektrolytische darstellung von Legierungen aus wässserigen Lösungen (Sammlung Vieweg, Tagesfragen aus den Gebieten Naturwiss. U. der Technik, No. 19). In: Kremann R (ed), Vieweg, Braunschweig
8. Gorbunova KM, Polukarov YuM (1976) In: Tobias CW (ed) Advances in Electrochemistry and Electrochemical Engineering. vol. 5, John Willey and Sons Inc., New York
9. Fedoteev NP, Bibikor NN, Vyacheslavov PM, Grilihes CYa (1962) Elektroliticheskie Splavy, MASHGIZ, Moscow
10. Faust CL (1963) In: Lowenheim FA (ed) Modern Electroplating, Ch. 18, John Wiley and Sons Inc., New York
11. Reinders W (1902) Z Physik Chem 42:225
12. Pushin N (1907) Z Anorg Chem 56:1
13. Lačnjevac U, Jović BM, Jović VD (2012) J Electrochem Soc 159: D310

14. Handbook of Chemistry and Physics (1976–1977) 57th edition, Weast RC (ed), CRC Press Inc., Cleveland, pp. D141–146
15. Jović VD, Tošić N (1998) J Electroanal Chem 441:69
16. Daen JA (1999) Lange's Handbook of Chemistry 15th Edition, McGraw-Hill Inc., New York
17. Duffield JR, Williams DR, Kron I (1991) Polyhedron 10:377
18. Turyan IYa, Kravtsov VI, Kondratev VV (1986) Elektrokhimiya 22:1388; 1618
19. Orekhova VV, Andryuschenko FK, Sakhnenko ND (1980) Elektrokhimiya 16:1304
20. Han C, Liu Q, Ivey DG (2008) Electrochim Acta 53:8332
21. Jović VD, Lačnjevac U, Jović BM, Karanović Lj, Krstajić NV (2012) Int J Hydrogen Energy 37:17882
22. Delahay P (1954) New Instrumental Methods in Electrochemistry, Interscience, New York
23. Jović VD, Stojanović MV, Jović BM, Gajić-Krstajić Lj (1992) J Serb Chem Soc 57:951
24. Jović VD, Tošić N, Stojanović M (1997) J Electroanal Chem 420:43
25. Dahms H, Croll J (1965) J Electrochem Soc 112:771
26. Higashi K, Fukushima H, Urakawa T, Adaniya T, Matsuko K (1981) J Electrochem Soc 128:2081
27. Horkans T (1979) J Electrochem Soc 126:1861
28. Horkans T (1981) J Electrochem Soc 128:45
29. Podlaha EJ, Landolt D (1996) J Electrochem Soc 143:885
30. Podlaha EJ, Landolt D (1996) J Electrochem Soc 143:893
31. Podlaha EJ, Landolt D (1997) J Electrochem Soc 144:1672
32. Marlot A, Kern P, Landolt D (2002) Electrochim Acta 48:29
33. Zeng Y, Li Z, Ma M, Zhou S (2000) Electrochem Comm 2:36
34. Sanches LS, Domingues SH, Carubelli A, Mascaro LH, J Braz Chem Soc 14: 556
35. Jović VD, Jović BM, Lačnjevac U, Branković G, Bernik S, Rečnik A (2010) Electrochim Acta 55:4188
36. Grgur BN, Krstajić NV, Elezović N, Jović VD (2005) J Serb Chrem Soc 70:879
37. Evans UR (1928) J Inst Metals 40:99
38. Glazunov A (1953) Metallic Protective Coatings 21:1262
39. Steigerwald RF, Greene ND (1962) J Electrochem Soc 109:1026
40. Pickering HW, Wagner C (1967) J Electrochem Soc 114:698
41. Pickering HW (1968) J Electrochem Soc 115:690
42. Pickering HW, Byrne PJ (1971) J Electrochem Soc 118:209
43. Holliday JE, Pickering HW (1973) J Electrochem Soc 120:470
44. Bockris JO'M, Rubin BT, Despić A, Lovreček B (1972) Electrochim Acta 17:973
45. Mance A, Mihajlović A (1980) J Appl Electrochem 10:967
46. Lee HP, Nobe K (1984) J Electrochem Soc 131:1236
47. Petro I, Mallat T, Syabo A, Hange F (1984) J Electroanal Chem 160:289
48. Shapovalov ET, Baranova LI, Yektser O (1988) Elektrokhimicheskie metody v metallovodenii i fazovom analize, Izd. Metallurgya, Moscow
49. Stevanović J, Skibina L, Stefanović M, Despić A, Jović VD (1992) J Appl Electrochem 22:172
50. Swathirajan S (1986) J Electrochem Soc 133:671
51. Jović VD, Zejnilović RM, Despić AR, Stevanović JS (1988) J Appl Electrochem 18:511
52. Swathirajan S (1987) J Electroanal Chem 221:211
53. Andricacos PC, Tabib J, Romankiw LT (1988) J Electrochem Soc 135:1172
54. Andricacos PC, Avana C, Tabib J, Duković J, Romankiw LT (1989) J Electrochem Soc 136:1336
55. Wong KH, Andricacos PC (1990) J Electrochem Soc 137:1087
56. Horkans J, I-Chia Hsu Chang, Andricacos PC, Podlaha EJ (1991) J Electrochem Soc 138:411
57. Jović VD, Despić AR, Stevanović JS, Spaić S (1989) Electrochim Acta 34:1093
58. Jović VD, Spaić S, Despić AR, Stevanović JS, Pristavec M (1991) Mater Sci Technol 7:1021
59. Skibina L, Stevanović J, Despić AR (1991) J Electroanal Chem 310:391

60. Stevanović R, Kovrigina I, Despić AR (1991) J SerbChem Soc 56:217
61. Despić AR, Electrochemistry in Transition from the 20th to the 21st Century. In: Murphy OJ, Srinivasan S, Conway BE (1992) Plenum Press, New York, p.453.
62. Jović VD, Jović BM, Despić AR (1993) J Electroanal Chem 357:357
63. Raub E, Engel A (1950) Z Metallk 41:485
64. Jović VD, Jevtić V (1996) J Serb Chem Soc 61:479
65. Jović VD, Jevtić V (1998) Electrochim Acta 43:63
66. Fedotev NP, Vyacheslavov PM (1970) Plating 3:700
67. Hansen M, Andrenko K (1958) Constitution of binary alloys. Mc Graw-Hill Book Company, Inc., New York, Toronto, London
68. Köster W, Hern E (1952) Z Metallk 43:333
69. Lewkonja K (1980) Z Anorg Chem 59:322
70. Westgren A, Ekman W (1930) Arkiv kemi, Mineral Geol B10:1
71. Lihl F, Buhl E (1955) Z. Metallkunde 46:787
72. Jović BM, Dobrovolska Ts, Lačnjevac U, Krastev I, Jović VD (2009) Electrochim Acta 54:7565
73. Porter D, Easterling KA (1980) Phase Transformations in Metals and Alloys, Van Nostrand Reinhold, Wokingham
74. Spitzer F (1905) Z Electrochem Angew Physik Chem 23:345
75. Rotinyan AL, Molotkova EN (1959) Zh Prikl Khim 11:2502
76. Thierer Ch, (1951) Gmelin Handbuch der anorganischen Chemie, System 65A(5), Weinheim/Bergstrasse, Verlag Chemie, p.653
77. Savitski EM, Pravoverov NL (1961) Zh Neorg Khim 76:499
78. Sturzenegger B, Puippe JC (1984) Platinum Met Rev 28:117
79. Dobrovolska Ts, Jović VD, Jović BM, Krastev I (2007) J Electroanal Chem 611:232
80. Dobrovolska Ts, Krastev I, Jović BM, Jović VD, Beck G, Lačnjevac U, Zielonka A (2011) Electrochim Acta 56:4344
81. Weibke F, Eggers H (1935) Z Anorg Chem 222:145
82. Campbell AN, Wagemann R, Ferguson RB (1970) Can J Chem 48:1703
83. Dobrovolska Ts, Krastev I, Zielonka A (2005) J Appl Electrochem 35:1245
84. Dobrovolska Ts, Veleva L, Krastev I, Zielonka A (2005) J Electrochem Soc 152 :C137
85. Stevanović JS, Jović VD, Despić AR (1993) 349:365
86. Dobrovolska Ts, Krastev I, Zielonka A (2010) ECS Trans 25:1
87. Petrauskas A, Grincevičiene L, Češuniene A, Juškenas R (2005) Electrochim Acta 50:1189
88. Elkhatabi F, Benballa M, Sarret M, Müler C (1999) Electrochim Acta 44:1645
89. Stevanović J, Gojković S, Despić A, Obradović M, Nakić V (1998) Electrochim Acta 43:705
90. Stevanović J, Despić A, Poleti D (1995) J Serb Chem Soc 60:285
91. Bajat JB, Stanković S, Jokić BM, Stevanović SI (2010) Surf Coat Techn 204:2745
92. Low CTJ, Wills RGA, Walsh FC (2006) Surf Coat Techn 201:371
93. Metcalfe AG (1974) Interfaces in Metal Composites. Academic Press, New York, p. 65
94. Meyer WR, Phillips A (1938) Trans Electrochem Soc 73:377
95. Aotani K (1953) J Electrochem Soc Jpn 21:180
96. Mikhalev PF (1939) C R Acad Sci URSS 24:899
97. Cohen U, Koch FB, Sard R (1983) J Electrochem Soc 130:1987
98. Tench D, White J (1984) Metall Trans 15A:2039
99. Ogden C (1986) Plating Surf Finish 73:130
100. Verbruge MW, Tobias CW (1985) J Electrochem Soc 132:1298
101. Despić AR, Jović VD (1987) J Electrochem Soc 134:3004
102. Despić AR, Jović VD, Spaić S (1989) J Electrochem Soc 136:1651
103. Despić AR, Trišović T (1993) J Appl Electrochem 23:662
104. Power CP, Ritchie IM (1975). In: Conway BE, Bockris JO'M (eds) Modern Aspects of Electrochemistry vol. 11, Plenum Press, New York
105. Yahalom J, Zadok O (1987) J Mater Sci 22:499

106. Lashmore DS, Dariel MP (1988) J Electrochem Soc 135:1218
107. Tench DM, White JD (1990) J Electrochem Soc 137:3061
108. Tench M, White J (1991) J Electrochem Soc 138:375
109. Ebrahimi F, Liscano AJ (2001) Mat Sci Eng A301:23
110. Yang C–C, Cheh HY (1995) J Electrochem Soc 142:3034
111. Yang C–C, Cheh HY (1995) J Electrochem Soc 142:3040
112. Roy S, Landolt D (1995) J Electrochem Soc 142:3021
113. Bradley PE, Landolt D (1997) Electrochim Acta 42:993
114. Despić AR, Jović VD, Tošić N (1998) Surf Coat Techn 105:206
115. Oberle RR, Cammarata RC (1995) Scr Metall Et Mater 32:583
116. Cammarata RC, Schleisinger TE, Kim C, Qadri SB, Edelstein AS (1990) Appl Phys Lett 56:1862
117. Meneyes S, Anderson DP (1990) J Electrochem Soc 137:440
118. Simunovich D, Schleisinger M, Snyder DD (1994) J Electrochem Soc 141:L10
119. Cziraki A, Pierron–Bohnes V, Ulhaq–Bouillet C, Toth–Kadar E, Bakonyi I (1998) Thin Solid Films 318:239
120. Bakonyi I, Toth–Kadar E, Becsei T, Toth J, Tarnoczi T, Cziraki A, Geröcs I, Nabiyouni G, Schwarzacher W (1996) J Magn Magn Mater 156:347
121. Bird KD, Schleisinger M (1995) J Electrochem Soc 142:L65
122. Hart R, Alper M, Attenborough K, Schwarzacher W (1994). In: Romankiw LT, Herman DAJr (eds) Proc. 3rd Int. Symp. on Magnetic Mater. Processes and Devices, Electrodeposition Division of the Electrochem. Soc., vol. 94-96, Pennington, p. 215.
123. Hua SZ, Lashmore DS, Salamanca–Riba L, Schwarzacher W, Swartzendruber LJ, McMichael RD, Bennett LH, Hart R (1994) J Appl Phys 76:6519
124. Cattarin S, Musiani M (2007) Electrochim Acta 52:2796
125. Anani A, Mao , Srinivasan S, Appleby AJ (1991) J Appl Electrochem 21:683
126. Iwakura C, Furukawa N, Tanaka M (1992) Electrochim Acta 37:757
127. Miao HJ, Piron DL (1993) Electrochim Acta 38:1079
128. Iwakura C, Tanaka M, Nakamatsu S, Noue H, Matsuoka M, Furukawa N (1995) Electrochim Acta 40:977
129. Gierlotka G, Rowinski E, Budniok A, Lagiewka E (1997) J Appl Electrochem 27:1349
130. Assuncao NA, De Giz MJ, Tremiliosi–Filho G, Gonzalez ER (1997) J Electrochem Soc 144:2794
131. Tavares AC, Trasatti S (1998). In: S.A. Sealey SA (ed.) Modern Chlor-Alkali Technology, vol. 7, SCI, London, p. 65
132. Baruffaldi C, Cattarin S, Musiani M (2003) Electrochim Acta 48:3921
133. Panek J, Serek A, Budniok A, Rowinski E, Lagiewka E (2003) Int J Hydrogen Energy 28:169
134. Losiewicz B, Budniok A, Rowinski E, Lagiewka E, Lasia A (2003) J Appl Electrochem 34:507
135. Olesky M, Budniok A, Niedbala J, Matyja P (1994) Electrochim Acta 39:2439
136. Musiani M (1996) Chem Commun 2403
137. Musiani M, Furlanetto F, Guerriero P (1997) J Electroanal Chem 437:131
138. Musiani M, Guerriero P (1998) J Electrochem Soc 145:549
139. Musiani M, Furlanetto F, Guerriero P (1998) J Electrochem Soc 145:555
140. Musiani M, Guerriero P (1998) Electrochim Acta 44:1499
141. Bertoncello R, Furlanetto F, Guerriero P, Musiani M (1999) Electrochim Acta 44:4061
142. Musiani M, Furlanetto F, Bertoncello R (1999) J Electroanal Chem 465:160
143. Bertoncello R, Cattarin S, Frateur I, Musiani M (2000) J Electroanal Chem.492:145
144. S. Cattarin, P. Guerriero, M. Musiani, Electrochim. Acta 46 (2001)4229.
145. Huet F, Musiani M, Nogueira RP (2003) Electrochim Acta 48:3981
146. Vazquez–Gomez L, Cattarin S, Guerriero P, Musiani M (2007) Electrochim Acta 52:8055
147. Vazquez–Gomez L, Cattarin S, Guerriero P, Musiani M (2009) J Electroanal Chem 634:42

148. Antozzi AL, Bargioni C, Iacopeti L, Musiani M, Vazquez–Gomez L (2008) Electrochim Acta 53:7410
149. Jović VD, Lačnjevac U, Jović BM, Gajić-Krstajić Lj, Krstajić NV, (2013) J Serb Chem Soc 78:689
150. Krstajić NV, Lačnjevac U, Jović BM, Mora S, Jović VD (2011) Int J Hydrogen Energy 36:6450
151. Jović VD, Lačnjevac U, Jović BM, Krstajić NV (2012) Electrochim Acta 63:124
152. Lačnjevac UČ, Jović BM, Jović VD, Krstajić NV (1012) J Electroanal Chem 677: 31
153. Jović BM, Lačnjevac U, Jović VD, Gajić-Krstajić Lj, Krstajić NV (2012) J Serb Chem Soc 77:211
154. Nagamura M, Ukihashi H, Shiragami O (1983). In: Jackson C (ed) Modern Chlor-Alkali Technology, vol. 2, Ellis Horwood, Chichester, p. 61
155. Grove DE (1986) In: Wall K (ed) Modern Chlor-Alkali Technology, vol. 3, Ellis Horwood, Chichester, p. 250
156. Trasatti S (1992). Electrocatalysis of hydrogen evolution: Progress in cathode activation. In: Gerischer H, Tobias CW (eds), Advances in Electrochemical Science and Engineering, Weinheim, Wiley-VCH Verlag GmbH, p. 1
157. Iwakura C, Tanaka M, Nakamatsu S, Noue H, Matsuoka M, Furukawa N (1995) Electrochim Acta 40:977
158. Rausch S, Wendt H (1995) J Appl Electrochem 22:1025